C O N T E N T S

SCHOOL OF ENGINEERING

Technical Papers

Proc. Schl. Eng. Tokai Univ., Ser. E
45 (2020) 1-6
DOI: 10.18995/24343641.45.1

A Proposal for Water Transportation by a Hydrogen Energy System
－A Feasibility Study for Kazakhstan －

by

Saule ZHOLDAYAKOVA[*1], Haruhisa UCHIDA[*2], Makoto Ryo HARADA[*3], Masashi SATO[*4], Ryota GEMMA[*5] and Yoshihito MATSUMURA[*6]

(Received on Mar. 31, 2020 and accepted on Aug. 20, 2020)

Abstract

This study examines the use of hydrogen as an energy carrier for spreading renewable energy and mitigating environmental problems, and proposes a system for carrying clean water together with hydrogen. Practical simulations were carried out assuming the present conditions of Kazakhstan. The capital and most other large cities are located both far from clean water sources, and areas with plenty of sunshine. The proposed model consists of hydrogen generation by solar-powered electrolysis, transportation of hydrogen by railways and electric power generation using fuel cells in cities. The fuel cells also generate clean liquid water.

This paper proposes a hydrogen transportation system by railway, where Ti-based hydrogen storage alloys fabricated with readily available metals in Kazakhstan are used. The railway is the most practical means of transportation compared to other methods in terms of utilities, economy, environment and time.

Keywords: Kazakhstan, Hydrogen energy system, Hydrogen storage alloys, Ti-based alloys, LCA

1. Introduction

Along with the spread of activities on SDGs, the realization of a sustainable society is expanding worldwide. It is necessary to realize the improvement of people's QOL as soon as possible in order to break away from the social system based on the massive consumption of fossil energy resources.

Kazakhstan is a country located in the central part of the Eurasian continent and is rich in coal, oil, and other mineral resources. Most cities have developed along the historical Silk Road. The existing social infrastructure was established under the Soviet Union in the 20th century and is still used today despite its aged condition.

In terms of the water supply system, each large city obtains water from the nearest river using aged facilities. However, the amount of incoming river water is reduced due to its utilization for neighboring countries' agriculture. Moreover, it arrives at the borders of Kazakhstan already polluted.

Not only industrial emissions and agricultural pesticides are causes of polluted tap water, but also nuclear pollution from nuclear tests during the Cold War in north-eastern to middle-southern parts of the country.

Under these conditions, the drinking water supply issue is a significant problem, including how to supply drinking water from limited water resources to large urban areas. This proposal is unique and rarely considered in Japan, an island with plenty of clean water.

This study proposes hydrogen energy as an alternate, new, sustainable, affordable, and reliable energy, as well as a drinking water supply source by utilizing hydrogen energy using fuel cells. As a first feasibility study, we propose a simple hydrogen energy system model as a solution for the water supply issues in Kazakhstan by utilizing the existing infrastructure as much as possible while considering cost and realizing period.

*1 Graduate School student, Course of Science and Technology
*2 Professor, Department of Human Development, Environment and Resources Course
*3 Lecturer, Department of Human Development, Environment and Resources Course
*4 Professor, Department of Applied Chemistry
*5 Junior Associate Professor, Department of Material Science
*6 Professor, Department of Nuclear Engineering

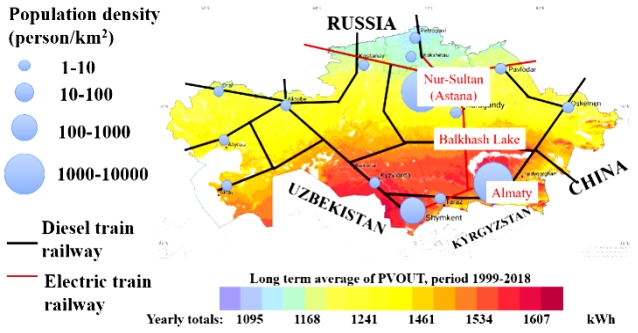

Fig.1 Solar radiation, population density, railway map of Kazakhstan made based on references [1-3].

2. Background

In Fig.1 the distribution of population and solar radiation, densities are shown. Suitable drinking water may be obtained from Balkhash Lake, one of the limited clean water resources located in the southeast area of the country. Large cities of Kazakhstan are Almaty and Nur-Sultan (Astana), both with a population of about 1 million. In Fig.1 railways connecting areas and cities are also shown.

2.1 *Energy consumption and resources*

Kazakhstan aims to reduce dependence on fossil fuels for its energy utilization and develop a sustainable society by utilizing renewable energy.

Kazakhstan's energy production covers more than twice its energy demand, and the energy self-sufficiency rate is around 200 % [4]. Coal represents almost 50 % of Kazakhstan's primary energy supply, and it is utilized for domestic energy consumption, which is more than 70 % of the total power generation [4]. However, the current existing infrastructure is disintegrating, and new construction is unfeasible because of a complicated political situation.

The potential of solar power is high in this country. For example, Kazakhstan's southern and central regions have high insolation that could be suitable for solar power with daylight hours of 2200-3000 h/year and sunlight 1.3-1.7×10^3 kWh/m^2 annually (Fig.1) [1]. Solar power could reach the range of 2.5-3.5×10^{12} kWh per year, which is 25 times larger than the present total production of electricity, and would use only half of the country's total surface area.

2.2 *Water consumption and supply*

In exchange for plentiful sunshine, water resources in Kazakhstan are not abundant, because of climate characteristics such as deficient annual precipitation and desertification. The country's rainfall amount is not large, with the average annual precipitation estimated around 250 mm.

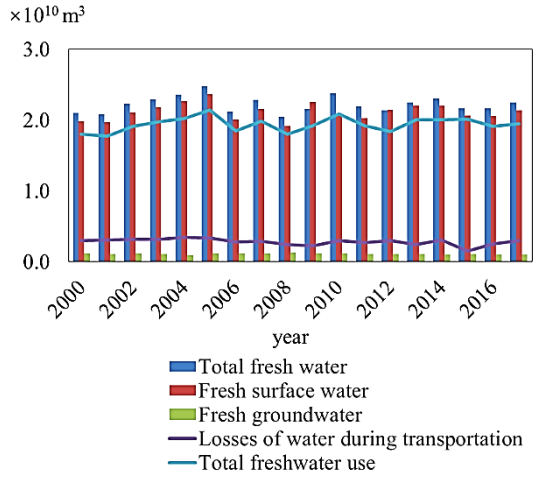

Fig. 2 Total freshwater abstracted, total freshwater use and losses of water during transportation [4].

In Kazakhstan, water resources are mainly concentrated in eight major rivers and three big lakes (the Caspian Sea, Aral Sea, and Balkhash Lake). Balkhash Lake is the primary source of freshwater.

Water availability across these major basins is distributed unevenly, and approximately 45 % of the water in the country inflows from neighboring countries such as Russia, China, Kyrgyzstan, and Uzbekistan. Inflows are expected to decrease due to increased water withdrawals for hydroelectricity generation and irrigation in Central Asia and China [5].

Annual freshwater withdrawals total around 2.3×10^4 m^3/year. Almost all freshwater is harvested from surface water because of a lack of groundwater. Consequently, surface water needs to be transported, and, unfortunately, 12 % of it is lost during transport due to old structures (Fig.2) [4].

The water supply service is relatively weak in terms of quantity and quality. A shortage of high-quality drinking water is still acute in some regions, where households in remote areas have the water delivered in water tanks and stored in individual reservoirs.

Moreover, tap water is not safe to drink in Kazakhstan, and around 30 % of consumers completely abandon it, preferring to buy bottled water. Hence, 9×10^5 m^3 per year of bottled water is transported in large cities [6].

The agriculture sector is the primary driver of water consumption in Kazakhstan (70 % of total consumption).The electricity industry and manufacturing are second large water consuming sectors at 20 % followed by households at 10 % [4].

3. Hydrogen Energy System

In order to create a hydrogen energy system, we need a practical consideration of hydrogen production, storage, and utilization that does not have a significant impact on the

environment [7].

For the realization and prosperity of hydrogen energy society, it is essential to recognize that its production method plays a very significant role in the level of environmental impacts. Hydrogen produced from water using renewable energy sources offers the prospect of long-term growth in full alignment with the need to protect the environment. It will be one of the most promising energy options for a sustainable future [8]. Cycling of hydrogen without CO_2 emissions can be achieved through the production of hydrogen by electrolysis and hydrogen consumption through the use of fuel cells.

Nowadays, the technologies for the production and use of hydrogen have been found, and efficiency problems have been identified. Also, to use hydrogen in practice, it is necessary to consider a reliable and stable method of storing and transporting it.

In this article, we focus on transporting and storing hydrogen, which is also a method for transporting water.

4. Hydrogen Transportation

Hydrogen can be transported by different means. Currently, the transport of compressed gaseous or liquid hydrogen by lorry to selected locations is the main option. A pipeline network is also an option for the general and largescale use of hydrogen as an energy source. However, pipelines require high initial investment levels and long-term construction. Design requirements for hydrogen pipelines are still evolving. Most hydrogen pipelines are designed to transport hydrogen only short distances, from the production facility to the end-user. Moreover, the hydrogen pipeline quickly develops leaks, requiring strict safety equipment and carries only about 80 % energy at the same pressure as natural gas [9].

Hydrogen pipelines have problems with embrittlement, safety, and leaks. Hydrogen has an active electron, and therefore behaves somewhat like a halogen. For this reason, hydrogen pipes have to resist corrosion in the ground. The problem is intensified because hydrogen can easily migrate into the crystal structure of most metals [10].

Hydrogen storage alloys have attracted considerable attention because they are safe and efficient media for transporting hydrogen energy. Since hydrogen storage alloys are known to be heavy, they can be transported by rail, consequently increasing the amount of hydrogen that can be transported in the existing infrastructure.

An essential transport mode in Kazakhstan is railway transport, which connects the entire country (Fig. 1)[3]. Trains account for 70 % of all cargo and passenger traffic, covering their world ranking rates and estimated cost [13].

Table 1 Kazakhstan (KZ) reserves of metal resources with

Metal	World Ranking	Confirmed Reserves ($\times 10^7$ kg)	Cost (US$/kg)	Global reserves (%)	Located part of KZ
Ti	10	2.40	4.8	0.1	East
Cr	2	38.2	5.1	30	West
Mn	4	63.5	2.0	25	Cent-ral
Fe	7	26.5	1.1	10	North

60 % of the country's territory. The load capacity of one freight car is 6-7×10^4 kg [11]. Additionally, transportation by railway is attractive for its lower emission of CO_2, which is 2.53×10^{-10} kg-CO_2/kg・m (25.3g / ton・km) [12].

Furthermore, the transportation of hydrogen by units is easy to carry to the required place, the required amount of electricity and water. If a fuel cell is attached to a locomotive, the train can supply energy by itself and distribute water along the rail lines.

5. Hydrogen Storage

As mentioned above, Kazakhstan has substantial natural and mineral resources. Specifically, Kazakhstan has 30 % of the global reserves of chrome ores, which is second globally, 25 % of manganese ores, 10 % of iron ores and is ranked tenth in the world in terms of titanium reserves [13].

In this contribution, we consider utilizing those metals for hydrogen storage alloys as hydrogen carriers. In general, the titanium-based alloys are among the most promising materials for hydrogen storage [14]. Currently, practically useful hydrogen storage alloys are made from rare earth metals, rare resources and are very expensive. In Kazakhstan Ti, Cr, Fe, and Mn are abundant, and their prices are lower than rare earth metals (Tabel 1).

According to the literature, TiCrMn and TiFeMn alloys absorb reversibly about 1-1.5 wt% of hydrogen on average (Table 2) [15-19]. Alloys TiCrMn, TiFeMn are suitable as capable carriers for the transport of hydrogen energy in Kazakhstan.

We suggest preparing hydrogen storage alloy by mechanical alloying (MA) technique, a more suitable manufacturing method for alloys' mass production. MA can synthesize various non-equilibrium alloys, so it has been widely applied to modify properties of a hydrogen storage alloy [20]. Compared with the arc melting (AM) method, the MA method enables synthesizing at low power for a long time. Moreover, since at the same vapor pressure 133 Pa, the temperature of Mn (1522 K) is lower than the other metals Cr (1968 K), Fe (2063 K), Ti (2464 K), it can be prepared by

Table 2 Hydrogen storage characteristics (Dissociation Temperature and pressure and H capacity), of Ti-based alloys prepared by arc melting (AM) and mechanical alloying (MA).

Alloys	T (K)	P (MPa)	H (wt%)	Preparation	Ref.
$Ti_{1.1}CrMn$	296	3.3	1.8	AM	15)
$TiCrMn_{0.8}$	304	1	1.98	AM	16)
$Ti_{1.1}CrMn$	273	1.2	1.61	AM	17)
$TiFe_{0.8}Mn_{0.2}$	298	1.5	1.65	AM	18)
$TiFe_{0.9}Mn_{0.1}$	295	0.8	1.5	AM	19)
$TiFe_{0.85}Mn_{0.15}$	298	1.5	1.2	MA	20)

MA at room temperature [21].

We have already investigated the preparation of alloys by MA in our previous work [22]. Our succeeding work is related to improving the hydrogenation characteristics of these alloys.

6. Hydrogen Energy System in Kazakhstan

The overall hydrogen system consists of solar energy, an electrolyzer for hydrogen production, alloys for hydrogen storage, trains for transportation, and fuel cells for utilization.

First, we consider the amount of hydrogen per capita as the necessary energy and the amount of water as the amount of hydrogen needed to be utilized.

The energy consumption per capita is 5.0×10^3 kWh/year (1 kWh = 1 J/s×3600 s = 3.6×10^6 J) and clean drinking water consumption per capita of 1 m^3/year in Kazakhstan [4]. We summarize the appropriately quantified analysis of the Hydrogen Energy System in Kazakhstan based on these amounts.

Corresponding hydrogen amount is calculated as follows of formula (1). We use Lower Heating Values (LHV) of hydrogen, which is 6.7×10^{-2} kWh/mol. (The lower heating value is the amount of heat released during the complete combustion of fuel without condensation of water vapor [23]. If it condensed, available energy is denoted as Higher Heating Values(HHV))

$$E_{\text{per capita}}\ (5\times10^3\ \text{kWh}) / LHV_{\text{hydrogen}}\ (6.7\times10^{-2}\ \text{kWh/mol}) = 7.4\times10^4\ \text{mol}\ H_2 \quad (1)$$

7.4×10^4 mol H_2 produces 7.4×10^4 mol water, which is 1.3 m^3/year and provides the necessary amount of hydrogen to required electricity 5×10^3 kWh/capita.

Secondly, we determine the required energy to produce this amount of hydrogen. We calculated the necessary energy from electrolyzer, solar power, and surface area based on efficiency, 70 %, and 16 %, respectively. Calculated results are shown in Table 3. We obtain 1.3 m^3/year/capita water by a fuel cell, which ensures the necessary water 1 m^3/year per capita.

Table 3 Calculation to produce the required energy and water by hydrogen/capita.

Necessary water to produce hydrogen	1.3 m^3/year
Solar power and surface area (16 % energy efficiency)	5.2×10^4 kWh/year 34.8 m^2
Energy from electrolyzer (70 % energy efficiency)	8.3×10^3 kWh/year
Necessary energy to produce hydrogen	5.8×10^3 kWh/year
Produced hydrogen	7.4×10^4 mol /year
Energy consumption per capita	5000 kWh/year
Produced water	1.3 m^3/year

We consider the fuel cell (50 % efficiency for electricity) and simulated hydrogen energy system for the capital city Nur-Sultan, where the population is growing, and consumption of energy and water is increasing (Fig. 3) [2].

In this paper, the hydrogen energy system was modeled for a city with a population of one million based on a calculation per capita. They will consume hydrogen, which is generated by the electrolysis method from Balkhash Lake by utilizing solar power and transported by hydrogen storage alloys via railway. The solar panel area will be located near Balkhash Lake because of high solar radiation in the South and Central part of Kazakhstan.

This lake was chosen because of the location and quality of water. Moreover, Balkhash Lake is the primary water resource in domestic supply. The volume of water in Balkhash Lake is 1.1×10^{11} m^3. The distance between Balkhash and Nur-Sultan is around 6×10^5 m [24].

We assume the weight of transported hydrogen storage alloy per wagon is 5.4×10^4 kg with 1.5 wt% of hydrogen. The hydrogen capacity per wagon is 4.1×10^5 mol.

If a regular train is composed of 50 wagons, 2.04×10^7 mol H_2 will be transported. If a train transports it 10 times per day, they transport 2.04×10^8 mol of H_2/day and 7.4×10^{10} mol /year. Approximately 3×10^7 kg/year of the alloy will be used. Finally, one million people are provided with water and 0.4 million people with electricity by utilizing fuel cells. These values are summarized in Fig. 3.

7. LCA of Hydrogen Energy System for Kazakhstan

Life Cycle Assessment is a systematic tool to analyze the environmental impact of a product through all stages of its life cycle, from the extraction of resources to the

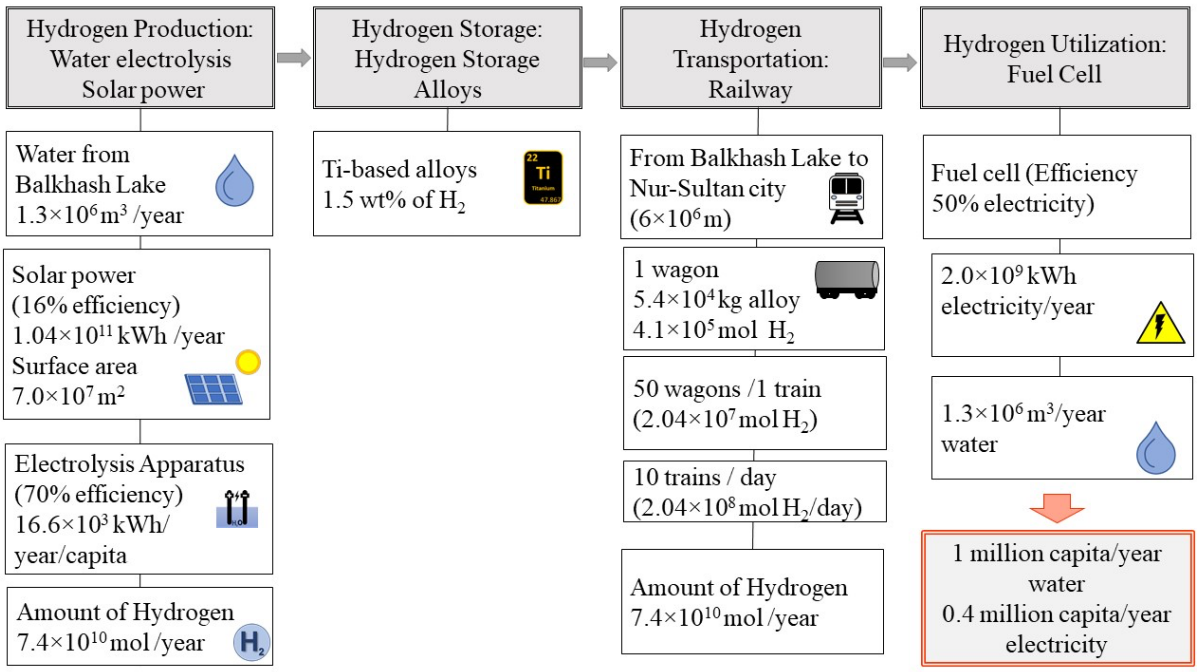

Fig.3 Hydrogen Energy System（HES）for the capital city of Kazakhstan
(calculation based for 1 million capita with 5000 kWh/year/capita electricity and corresponding water consumption).

production of materials, parts and the products itself, and its management after it is discarded, either by reuse, recycling or final disposal. LCA compiles and evaluates the inputs and outputs and the potential environmental impacts of a product system throughout its life cycle.

IDEA (Inventory Database for Environmental Analysis), a Japanese database that mainly uses national and some international statistics as its data source and aims to model the environmental impacts [25]. Unfortunately, the data for Kazakhstan is not available. To compare and see the general environmental impact, IDEA v2 was chosen.

We took into account the available CO_2 emissions from each process in this system. Based on IDEA soft dates and other references, we calculated considering the values listed in Table 4 the CO_2 emissions for the Hydrogen Energy System in Kazakhstan, which was more than 20 times less than present CO_2 emissions for electricity coal.

Table 4 CO_2 emissions of corresponding process delivered form calculation using IDEA data [25].

Process	CO_2 (kg)	Consumption/ year (for 10^6 capita)	CO_2 (kg) for HES
Consumption of solar power 1kWh	5×10^{-2}	1.04×10^{11} kWh /year	5.2×10^{8}
Production of Ti 1kg	9.2×10^{-5}	10^7 kg	9.2×10^{2}
Production of Cr 1kg	5.9×10^{-3}	10^7 kg	5.9×10^{4}
Production of Mn 1kg	5.9×10^{-3}	10^7 kg	5.9×10^{4}
Production of Fe 1kg	1.1×10^{-1}	10^7 kg	1.1×10^{6}
Ball milling 1000h /10^5kg [26]	7.2×10^{2}	3×10^7 kg	2.2×10^{4}
Freight train 10^3m/10^3 kg [27]	2.5×10^{-2}	6×10^5 m/ 3×10^7 kg	1.5×10^{8}
Fuel-cell	0	2.0×10^9 kWh	0
Total for HES in KZ			**6.7×10^8**
Present electricity	3.5×10^{-1} /kWh	5×10^9 kWh	1.4×10^{10}

8. Conclusion

This contribution considered the energy and water situation in Kazakhstan, which is currently significantly dependent on fossil fuels, despite the high potential of renewable energy sources, especially the potential of solar energy. Due in part to the abundance of sunshine, there are not many water resources in Kazakhstan.

Thus, half of the water resources inflow from neighboring countries. Depending on the transboundary rivers, the lack of groundwater, and losses during the transportation of surface water make this problem more serious.

This paper supposes the role of the hydrogen energy system in Kazakhstan for water supply, renewable energy distribution, and reduction of greenhouse gas emissions. Transportation of water can be driven by the production of hydrogen through electrolysis and the consumption of hydrogen through the use of fuel cells, as proposed in the frame of the hydrogen energy system. We revealed that the required 5000 kWh/year electricity and 1 m^3/year water are obtained by feasible hydrogen transportation.

The system is also capable of satisfying drinking water requirements, and society can become practically self-sufficient. The LCA result confirms that hydrogen is considered to be an ideal energy carrier in the future and can play a considerable role in the energy system of Kazakhstan.

In the future, the transportation possibilities of the fuel cell by train and utilization of fuel cells will be possible not only for large cities, but also for rural areas, and gives a significant opportunity for water supply. Transportation of hydrogen by storage alloys via railways allows the export of energy and water to neighboring countries. The water supply system considered here can be extended to other countries with water scarcity problems.

Acknowledgment

The authors express sincere gratitude to Tokai University, Kokudo Scholarship Foundation, The College Women's Association of Japan, Isehara Rotary Club Japan, and the Bolashak Presidential Scholarship Program of Kazakhstan.

References

1) Weather data and software for solar power investments, Solar resource maps of Kazakhstan, http://www.solargis.info
2) Geo-Ref.Net, Population density of Kazakhstan, http://geo.ref.net
3) Kazakhstan Temir Zholy, Railway map of Kazakhstan, http://www.railway.kz
4) Statistic Agency of Kazakhstan, http://www.stat.gov.kz
5) M. Karatayev, Z. Kapsalyamova, L. Spankulova, A. Skakova, Priorities and challenges for a sustainable management of water resources in Kazakhstan, Sustainability of Water Quality and Ecology Vol.9, pp.115-135 (2017).
6) Kapital Kazakhstan, Water Business in Kazakhstan www.kapital.kz
7) N. Saba, T. Manzoor, A. Pandith, Hydrogen storage: Materials, methods, and perspectives, Renewable Sustainable Energy Rev, Vol.50, pp. 457-469 (2015).
8) M. Smitkova, F. Janicek, J. Riccardi, Life cycle analysis of processes for hydrogen production; Int. J Hydrogen Energy, Vol.36, pp.7844-7851, (2011).
9) H-H. Uchida, K. Yoshida, M.Suga, Comparison in Environmental impact of energy transportation by hydrogen and electricity, Proceedings of the 3rd Int. Conf. on Balance, pp.587-590, (1998).
10) European Industrial Gases Association, Hydrogen transportation Pipelines, http://www.eiga.org
11) Railway Pro, https://www.railwaypro.com
12) Kaztemirtrans company, http://www.kazcargo.kz
13) Mining world of Kazakhstan, http://www.miningworld.kz
14) Akiba E. Hydrogen Absorbing Alloys, Curr. Opin. Solid State Mater. Sci, Vol.4, pp.267–272 (1999).
15) Kojima Y, Kawai Y, Towata S, Matsunaga T, Shinozawa T, Kimbara M, Development of metal hydride with high dissociation pressure, J. Alloys Compd, Vol.419, pp.256-261 (2006).
16) Z. Cao, L. Ouyang, H. Wang, J.Liu, D.Sun, Q. Zhang, M. Zhu, Advanced high-pressure metal hydride fabricated via Ti-Cr-Mn alloys for a hybrid tank, Int. J Hydrogen Energy, Vol. 40, pp.2717-2728 (2015).
17) F. Agresti, L. Russo, A. Maddaleno, G. Principi, G. Mazzolai, B. Coluzzi, Reaction of hydrogen with the Laves phase (C 14) $TiCr_{1.79-x}Mn_x$ compounds, Mater. Sci. Eng. A, Vol.521-522, pp.143-146, (2009).
18) R. Wakabayashi, S.Sasaki, N. Okinaka, T. Akiyama, Self-ignition combustion synthesis of $TiFe_{1-x}Mn_x$ hydrogen storage alloy, Int. J. Hydrogen Energy, Vol.34, pp. 9122–9127 (2009).
19) A. Zeaiter, P. Nardin, M. Pour Yazdi, A. Billard. Outstanding shortening of the activation process stage for a TiFe-based hydrogen storage alloy, Mater. Res. Bull. Vol.112, pp.132–141 (2019).
20) J. Bellosta von Colbe, J. Puszkiel, G. Capurso,A. Franz, H. Benz, H.Zoz, T. Klassen, M. Dornheim, Scale-up of milling in a 100 L device for processing of TiFeMn alloy for hydrogen storage applications: Procedure and characterization, Int. J. Hydrogen Energy, Vol.44(55), pp.29282–29290 (2019).
21) Power Stream, Vapor Pressure of Metals http://www.powerstream.com
22) S. Zholdayakova, R. Gemma, H-H. Uchida, M. Sato, Y. Matsumura, Mechanical Composition Control for Ti-Based Hydrogen Storage Alloys, e-J. Surf. Sci. Nanotech. Vol. 16, pp. 298-301 (2018).
23) Hydrogen Tools, Lower Heating Values www.h2tools.org
24) International Lake Environmental Committee, Balkhash Lake, http://www.ilec.or.jp
25) Japan Environmental Management Association for Industry, Inventory Database for Environmental Analysis, http://www.jemai.or.jp
26) Mineral Processing Laboratory Equipment, Industrial ball mill, https://www.911metallurgist.com
27) The Chemical Logistic Association, Measuring and Managing CO_2 http://www.ecta.com

Proc. Schl. Eng. Tokai Univ., Ser. E
45 (2020) 7-16
DOI: 10.18995/24343641.45.7

Simple Visualization of the Distribution of Ozone Concentration Generated by Atmospheric-pressure Plasma Jet Irradiation Using Test Strips

by

Hiroshi KUWAHATA*1 and Takaaki YAMAGUCHI*2

(Received on Mar. 27, 2020 and accepted on Jul. 24, 2020)

Abstract

The distribution of ozone (O_3) concentration generated by atmospheric-pressure argon (Ar) plasma jet irradiation was visualized using test strips. The O_3 test strips become brown in the presence of O_3, enabling the O_3 concentration to be easily determined on the basis of thedarkness of the color. An Ar plasma jet generated with a frequency of 10 kHz, an applied voltage of 10 kV, and an Ar gas flow rate of 10 L/min was ejected into the air in the form of an inverse cone with a length of approximately 15 mm and a maximum diameter of 6 mm. After plasma jet ejection for 1 s, the color of the O_3 test strips turned brown (>210 μg/m^3) except in the region of the plasma jet (inverted triangle). This result indicates that O_3 was generated in the region where the plasma came into contact with the air.

The results of this study suggested that the distribution of the O_3 concentration generated by atmospheric-pressure Ar plasma jet irradiation is dependent on the plasma ejection/irradiation duration, irradiation distance, and applied voltage.

Keywords: Atmospheric-pressure plasma, Ozone, Visualization, Test strips

1. Introduction

Research is being carried out on the application of atmospheric-pressure plasma in the surface treatment of solid materials [1-6], water purification [7-10], and the inactivation of bacteria and fungi [11-15]. Recently, active research on the plasma has been carried out on a wide variety of biomedical applications [16-19] including wound healing [20-23], cancer cell treatment [24-26], and the introduction of genes and drug molecules into cells [27-31]. It is known that ozone (O_3) is generated owing to the introduction of plasma in the air. O_3 is generated because high-energy electrons in the plasma collide with oxygen (O_2) molecules in the air and the oxygen (O) atoms produced by the dissociation of the O_2 molecule bind to another O_2 molecule [32, 33]. O_3 is one of the reactive oxygen species (ROS) and has a high oxidation-reduction potential of 2.07 V [34, 35], thereby easily oxidizing objects. This oxidizing power is useful in various fields of research.

The concentration of O_3 generated when an atmospheric-pressure plasma jet is ejected into the air is measured by ultraviolet (UV) absorption [36-40], an O_3 monitor [41], and molecular beam mass spectrometry (MBMS) [42]. The distribution of the O_3 concentration was studied by Winter *et al*. by means of UV absorption using a deuterium (D_2) lamp, a monochromator, an imaging spectrometer, and an intensified charge-coupled device (iCCD) camera [38]. It was also studied by Zhang *et al*. by means of UV absorption using a mercury (Hg) lamp, a monochromator, and a photomultiplier [39].

As explained above, there have been reports on the distribution of the O_3 concentration when an atmospheric-pressure plasma jet is ejected into the air. However, the suggested measurement methods require much equipment and time. In addition, the distribution of the concentration of O_3 existing on the surface of an object when it is irradiated with an atmospheric-pressure plasma jet has not been measured.

In our previous study, we measured the distribution of the concentration of hydrogen peroxide (H_2O_2) generated by atmospheric-pressure argon (Ar) plasma jet irradiation using H_2O_2

*1 Associate Professor, Department of Electrical and Electronic Engineering
*2 Undergraduate Student, Department of Electrical and Electronic Engineering

test strips [43]. H_2O_2 is also an ROS with an oxidation-reduction potential of 1.77 V [34]. The color of the H_2O_2 test strips turns blue in the presence of H_2O_2, and the concentration of H_2O_2 can be simply determined on the basis of the darkness of the color. In that study, it was found that the distribution of the H_2O_2 concentration is dependent on irradiation duration, irradiation distance, and applied voltage. Test strips for the simple measurement of the O_3 concentration are commercially available. The color of the test strips turns brown in the presence of O_3, and the O_3 concentration can be determined on the basis of the darkness of the color. The principle of the color reaction is due to the oxidation of the colorless iodide on O_3 test strips to brown iodine induced by O_3. There have been no reports on visualizing the distribution of O_3 concentration obtained using O_3 test strips to the best of our knowledge.

In this study, using O_3 test strips, we tried to visualizethe dependences of the O_3 concentration on plasma ejection/irradiation duration, irradiation distance, and applied voltage when an atmospheric-pressure Ar plasma jet is ejected into the air or when an object is irradiated with an atmospheric-pressure Ar plasma jet.

2. Experimental Methods

Figure 1 shows a schematic of the experimental setup used in this study. In the unit used to generate a plasma jet, a copper tube (inner diameter, 4 mm; outer diameter, 6 mm) as the discharge electrode was inserted into a dielectric quartz tube (length, 50 mm; inner diameter, 6 mm; outer diameter, 8 mm), around which a copper foil (thickness, 0.05 mm; width, 10 mm) was wrapped as the ground electrode [44]. A high AC voltage was applied to the electrodes to induce a dielectric barrier discharge inside the quartz tube between the electrodes and to convert the Ar gas into plasma, which was then ejected into the air in the form of a jet. A high-voltage power supply (LHV-10AC, Logy Electric Co., Ltd.) was used to generate the Ar plasma jet (frequency, 10 kHz; applied voltage, 3–10 kV; Ar gas flow rate, 10 L/min). The gas flow rate was adjusted using a gas flow meter (RK-1250, Kofloc Kyoto, Kojima Instruments Inc.). The voltage and current were measured using a high-voltage probe (P6015A, Tektronix, Inc.) and a current probe (A621, Tektronix, Inc.), respectively, which were both connected to a digital oscilloscope (TDS1001B, Tektronix, Inc.).

The plasma jet irradiated in the container made of transparent acrylic resin. The dimensions of the container are 120 (W) × 100 (D) × 180 (H) mm^3. The front side of the container is open. The height of the sample stage is variable in the range of 60–110 mm.

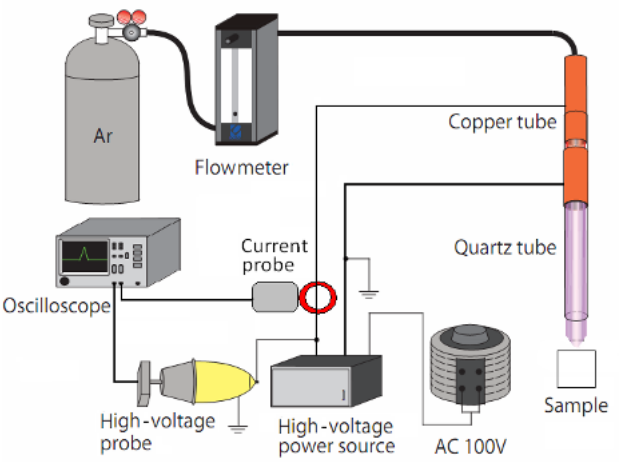

Fig. 1 Schematic of experimental setup.

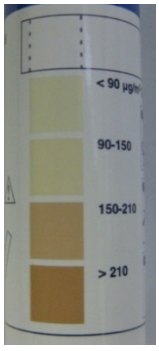

Fig. 2 Color chart of O_3 test strip.

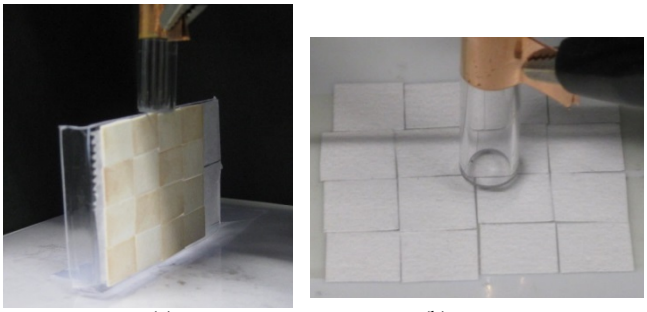

(a) (b)

Fig. 3 Photographs of O_3 test strips during measurement of distribution of O_3 concentration
(a) Ejection into air and (b) Irradiation onto object.

O_3 test strips (Macherey-Nagel) were used to determine the O_3 concentration. Figure 2 shows the color chart of the O_3 test strips. The color of the O_3 test strips turns brown in the presence of O_3, and the O_3 concentration can be determined in four levels (<90, 90–150, 150–210, and >210 μg/m^3) on the basis of the darkness of the color.

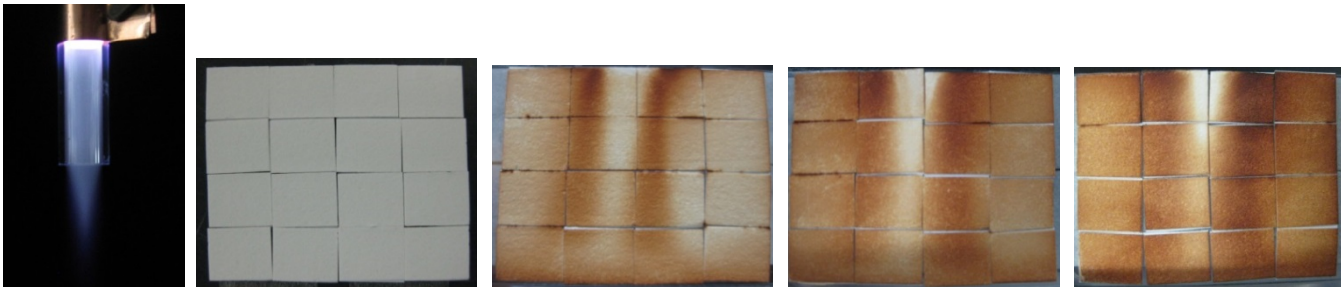

(a) (b) (c) (d) (e)

Fig. 4 Photographs of atmospheric-pressure Ar plasma jet ejected into air and O_3 test strips for different irradiation durations (applied voltage, 10 kV; Ar gas flow rate, 10 L/min) (a) Plasma jet, (b) Before ejection, (c) Ejection for 1 s, (d) Ejection for 10 s, and (e) Ejection for 30 s.

Figure 3 shows photographs of the O_3 test strips during the measurement of the distribution of the O_3 concentration. When the plasma jet was ejected into the air [Fig. 3(a)], a total of 16 (4 × 4) O_3 test strips (dimensions of one test strip, 8 × 10 mm^2; dimensions of 16 test strips, 32 × 40 mm^2) were arranged and set up vertically immediately below the center of the quartz tube. When the plasma jet was irradiated onto an object [Fig. 3(b)], a total of 16 (4 × 4) O_3 test strips were placed immediately below the quartz tube.

3. Results and Discussion

3.1 *Ejection of atmospheric-pressure Ar plasma jet into air*

3.1.1 *Dependence of distribution of O_3 concentrationon plasma ejection duration*

Figure 4 shows photographs of the atmospheric-pressure Ar plasma jet ejected into the air and O_3 test strips for different plasma ejection durations. When an Ar plasma jet was generated with an applied voltage of 10 kV and an Ar gas flow rate of 10 L/min, an atmospheric-pressure Ar plasma jet with an inverse cone shape having a length of ~15 mm and a maximum diameter of 6 mm was ejected into the air [Fig. 4(a)]. As shown in Fig. 4(b), the color of the O_3 test strips remained white before the plasma ejection. After ejecting for 1 s [Fig. 4(c)], the color of the test strips that came into contact with the plasma jet remained white but thatin the vicinity of that area turned brown. From this result, it was found that O_3 was generated simultaneously with the ejection of the plasma jet in the region where the plasma jet came into contact with the air, but it was not generated in the plasma. The nearer the region was from the plasma jet, the greater the darkness of brown became. With further distance from the plasma jet, the color became lighter. This finding indicates that the O_3 generated through contact between the plasma jet and the air diffused in its vicinity. By comparing the darkness of the color of the O_3 test strips with the color chart, the O_3 concentration was found to be >210 μg/m^3 at the edge of the plasma jet (within a radius of ~4–8 mm from the center of the plasma) and was 150–210 μg/m^3 in its vicinity (within a radius of 8–20 mm from the center of the plasma). The shape of the white area was almost identical to that of the plasma jet. The length of the white area was ~16 mm and the width was ~10 mm at the top of the O_3 test strips (immediately below the quartz tube), which gradually decreased with distance from the top. After 10-s ejection [Fig. 4(d)], the color of the O_3 test strips in the vicinity became darker than that in the case of 1-s ejection. This finding indicates that the O_3 concentration increased; the O_3 concentration was found to be >210 μg/m^3 even in the vicinity. The size of the white area decreased slightly [~16 (L) mm × ~8 (W) mm]. After 30-s ejection [Fig. 4(e)], the color of the O_3 test strips in the vicinity became much darker. This finding indicates that the O_3 concentration further increased; the O_3 concentration was found to be >210 μg/m^3 even in the vicinity. The size of the white area was further decreased [~13 (L) mm × ~6 (W) mm]. With increasing plasma ejection duration, the white area decreased. This is because the O_3, which was generated at the site where the plasma jet came into contact with air, came into continuous contact with the O_3 test strips and changed the color of the test strips at the edge ofthe plasma jet. From the above findings, with increasing plasma ejection duration, the concentration of O_3 generated in the vicinity of plasma was found to increase. It is considered that the concentration of generated O_3 does not change with time and remains constant when measured in a completely open space. In our experiment, however, the O_3 concentration increased with the plasma ejection duration. This is because the O_3 test strips were placed in an acrylic container, which was only open at the front side and thus was not completely open. In this case, some of the generated O_3 remained in the container and the O_3 concentration increased with time.

In the study of Winter *et al*., a plasma jet of ~4 mm length was

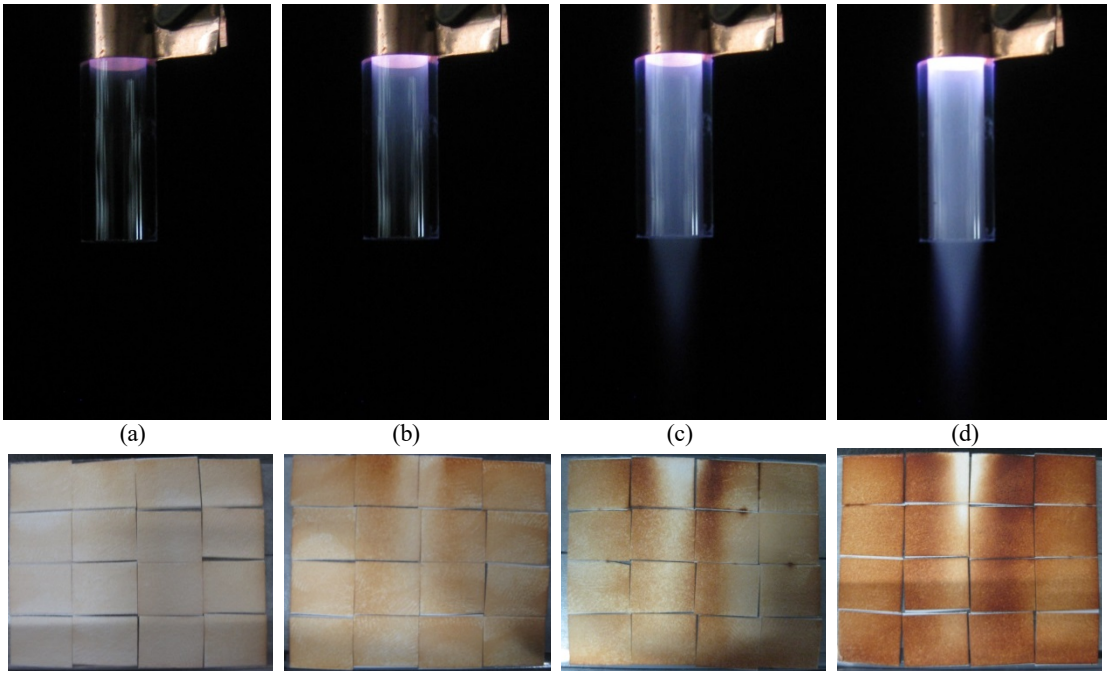

Fig. 5 Photographs of atmospheric-pressure Ar plasma jet ejected into air and O_3 test strips for different applied voltages (Ar gas flow rate, 10 L/min; plasma ejection duration, 30 s) (a, e) 3 kV, (b, f) 6 kV, (c, g) 8 kV, and (d, h) 10 kV.

generated by introducing a flow of an Ar gas [3 standard L/min (slm)] mixed with O_2 into a quartz capillary (inner radius, 0.8 mm) with a high-frequency applied voltage (~1 MHz, 2–6 kV_{pp}) [38]. The distribution of the O_3 concentration was studied by means of UV absorption at a wavelength λ = 254 nm using a D_2 lamp, a monochromator, an imaging spectrometer, and an iCCD camera. They reported that the O_3 concentration of 1.5 × 10^{16} cm^{-3} at the end of the plasma jet (position in the axial direction along the capillary, z = 4 mm) was the highest when the gas mixture of Ar +1.0% O_2 was used. With increasing distance in the ejection direction, the O_3 concentration gradually decreased to 2.5 × 10^{15} cm^{-3} at z = 19 mm. Regarding the spread of O_3 in the horizontal direction, the radius r of the plasma jet was 0.75 mm at z = 4 mm; it reached the maximum (r = 2.0 mm) at z = 15 mm and decreased to r = 1.75 mm at z = 19 mm. In the study of Zhang *et al*., a plasma jet of ~9 mm length was generated with a flow of Ar gas (2slm) mixed with 2% O_2 in a quartz tube (inner diameter, 1.8 mm) with a plasma power of 13.56 MHz and 6.5 W [39]. The distribution of the O_3 concentration was studied by means of UV absorption at a wavelength λ = 253.7 nm using a Hg lamp, a monochromator, and a photomultiplier. They reported that the O_3 concentration of 1.9 × 10^{15} cm^{-3} was the highest at 4 mm from the end of the plasma jet (z = 13 mm). With increasing distance in the ejection direction, the O_3 concentration gradually decreased to 6 × 10^{14} cm^{-3} at z = 25 mm. Regarding the spread of O_3 in the horizontal direction, the radius r of the plasma jet was 1.5 mm at the end of the plasma jet (z = 9 mm), reached the maximum (r = 2.5 mm) at z = 15 mm, and decreased to r = 1.5 mm at z = 19 mm. In the study of Deng *et al*., a plasma jet was generated with a flow of nitrogen (N_2) gas (8 slm) in the quartz tube (inner diameter, 5 mm) with the application of direct current (5–30 mA) [41]. By ejecting the plasma jet through a metal mesh, an afterglow was generated. They examined the distribution of the O_3 concentration from the afterglow using an O_3 monitor. In the case of the current of 25 mA, they reported that the O_3 concentration was ~22 ppm at 2 mm from the metal mesh (z = 2 mm). With increasing distance in the ejection direction, the O_3 concentration gradually increased, peaked (90 ppm) at z = 15 mm, and then gradually decreased to ~30 ppm at z = 30 mm.

3.1.2 *Dependence of distribution of O_3 concentrationon applied voltage*

Figure 5 shows photographs of the atmospheric-pressure Ar plasma jet ejected into the air and O_3 test strips for different applied voltages. At an applied voltage of 3 kV [Fig. 5(a)], a plasma jet was observed only in the vicinity of the electrode and it seemed that no plasma jet was ejected from the quartz tube. The color of the entire O_3 test strips turned slightly brown [Fig. 5(e)] and no white area indicating plasma ejection was observed. The O_3 concentration over the entirety of the O_3 test strips was 90–150

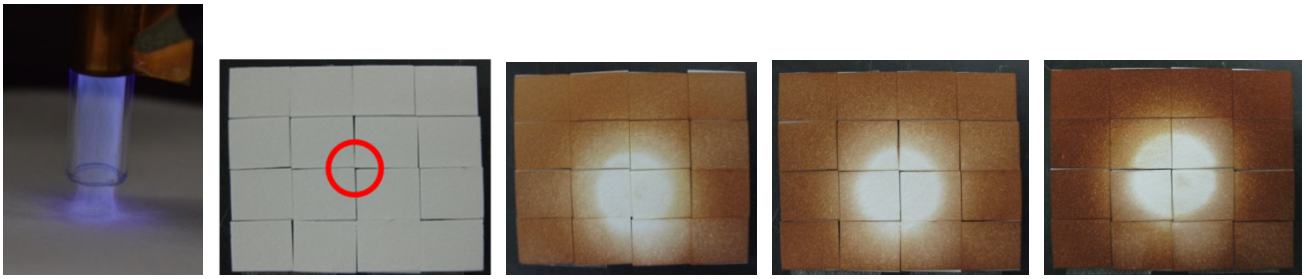

(a) (b) (c) (d) (e)

Fig. 6 Photographs of atmospheric-pressure Ar plasma jet irradiation and O_3 test strips irradiated with plasma jet for different irradiation durations (applied voltage, 10 kV; Ar gas flow rate, 10 L/min; irradiation distance, 5 mm)
(a) Plasma jet, (b) Before irradiation, (c) Ejection for 1 s, (d) Ejection for 5 s, and (e) Ejection for 10 s.

μg/m^3. This finding indicates that O_3 was generated in the quartz tube even when the plasma jet was not ejected from the quartz tube but generated in the quartz tube. At an applied voltage of 6 kV [Fig. 5(b)], no plasma was again ejected from the quartz tube. A small white area indicating plasma jet ejection was observed on the O_3 test strips [Fig. 5(f)]. The dimensions of the white area were ~16 (L) mm × ~7 (W) mm. The O_3 concentration was >210 μg/m^3 at the edge of the plasma jet and 150–210 μg/m^3 in its vicinity. At an applied voltage of 8 kV [Fig. 5(c)], a plasma jet appeared to be ejected from the quartz tube to a distance of ~10 mm. The white area indicating plasma jet ejection was observed on the O_3 test strips [Fig. 5(g)]. The dimensions of the white area were ~16 (L) mm × ~8 (W) mm. The O_3 concentrations were >210 μg/m^3 at the edge of the plasma jet and 150–210 μg/m^3 in its vicinity. At an applied voltage of 10 kV [Fig. 5(d)], the plasma jet was apparently ejected from the quartz tube to a distance of ~15 mm. A white area indicating plasma jet ejection was observed on the O_3 test strips [Fig. 5(h)]. The dimensions of the white area were ~13 (L) mm × ~6 (W) mm. The O_3 concentration was >210 μg/m^3 at the edge of the plasma jet and in its vicinity. Comparing the results in Figs. 5(f)–5(h), we can see that the color of the O_3 test strips became darker with increasing applied voltage. From this result, it was concluded that the O_3 concentration increased with increasing applied voltage, suggesting that the number of high-energy electrons is larger in a plasma jet generated at a higher applied voltage.

3.2 *Irradiation of atmospheric-pressure Ar plasma jet onto object*

3.2.1 *Dependence of distribution of O_3 concentration on irradiation duration*

Figure 6 shows photographs of plasma jet irradiation and O_3 test strips irradiated with the plasma jet for different irradiation durations. Filter paper, instead of O_3 test strips, was placed under the quartz tube to take a photograph shown in Fig. 6(a). The plasma jet reached the filter paper and extended horizontally on the filter paper. The diameter of the region over which the plasma extended was ~17 mm. The color of the O_3 test strips before plasma irradiation was white [Fig. 6(b)]. The plasma jet was ejected onto the center of the O_3 test strips. After plasma jet irradiation for 1 s [Fig. 6(c)], the color of the O_3 test strips turned brown except in the area irradiated with the plasma jet. This finding indicates that O_3 was generated immediately on the O_3 test strips irradiated with the plasma jet but was not generated in the region irradiated with the plasma jet. The diameter of the white area was ~12 mm, which was smaller than that of the region over which the plasma extended (~17 mm). This result indicates that O_3 was generated inside the edge of the region over which the plasma extended horizontally on the O_3 test strips. The area of the O_3 test strips that turned brown extended to a radius of at least 26 mm from the center of the region irradiated with the plasma and the O_3 concentration was >210 μg/m^3. Namely, when an object was irradiated with atmospheric-pressure Ar plasma jet for 1 s, O_3 with a concentration of >210 μg/m^3 was generated in the vicinity of the object. The region with a O_3 concentration >210 μg/m^3 was considered to extend to a radius of at least 26 mm from the center of the region irradiated with the plasma. As seen from the results in Figs. 6(c)–6(e), the brown color of the O_3 test strips became darker with increasing irradiation duration. This finding indicates that the O_3 concentration in the vicinity of the object increased with increasing irradiation duration. The diameter of the white area changed negligibly and was in the range of ~12–14 mm regardless of the irradiation duration. On the basis of the above findings, we concluded that O_3 was not generated in the region of the object irradiated with the plasma and no effect of O_3 was expected in this region.

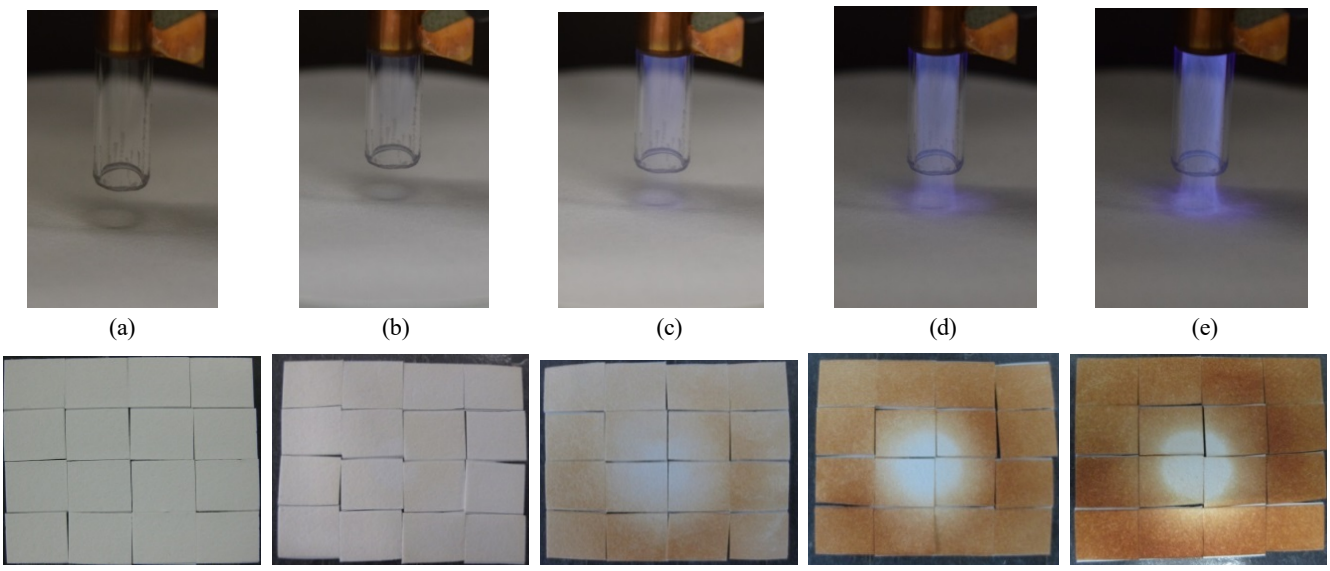

Fig. 7 Photographs of atmospheric-pressure Ar plasma jet irradiation and O_3 test strips irradiated with plasma jet for different applied voltages (Ar gas flow rate, 10 L/min; irradiation distance, 5 mm; irradiation duration, 10 s) (a, f) 3 kV, (b, g) 4 kV, (c, h) 6 kV, (d, i) 8 kV, and (e, j) 10 kV.

3.2.2 *Dependence of distribution of O_3 concentration on applied voltage*

Figure 7 shows photographs of plasma jet irradiation and O_3 test strips irradiated with the plasma jet for different applied voltages. At an applied voltage of 3 kV [Fig. 7(a)], no plasma was generated. As shown in Fig. 5(a), at the same voltage, a plasma jet was generated in the vicinity of the electrode. From this finding, an applied voltage of 3 kV is deemed the minimum voltage required for the generation of a plasma jet. At an applied voltage of 3 kV, the color of the O_3 test strips remained white, as shown in Fig. 7(f), because no plasma jet was generated. At an applied voltage of 4 kV [Fig. 7(b)], a plasma jet was generated only in the vicinity of the electrode. The color of the entirety ofthe O_3 test strips became slightly brown, as shown in Fig. 7(g). The O_3 concentration was <90 μg/m^3. This finding indicates that O_3 was generated and extended horizontally on the O_3 test strips to a radius of at least ~26 mm from the center of the region irradiated with the plasma jet, even when no plasma jet was ejected from the quartz tube. At an applied voltage of 6kV [Fig. 7(c)], a plasma jet was ejected from the quartz tube and came into weak contact with the O_3 test strips. As shown in Fig. 7(h), the color of the area irradiated with the plasma jet remained white but the color of the O_3 test strips in the vicinity of that area turned slightly brown, and the O_3 concentration was estimated to be 90–150 μg/m^3. At an applied voltage of 8 kV [Fig. 7(d)], plasma jet was ejected from the quartz tube, came into contact with the O_3 test strips, and then extended horizontally over the O_3 test strips. The diameter of the region over which the plasma extended was ~13 mm. As shown in Fig. 7(i), the brown color of the area on the O_3 test strips in the vicinity of the region irradiated with the plasma jet became much darker. The O_3 concentration was 150–210 μg/m^3. The diameter of the white area was ~12 mm, which is almost the same as that of the region over which the plasma jet extended. At an applied voltage of 10 kV [Fig. 7(e)], a plasma jet was ejected from the quartz tube, came into contact with the O_3 test strips, and then extended horizontally over the O_3 test strips. The diameter of the region over which the plasma extended was ~17 mm. As shown in Fig. 7(j), the brown color of the area on the O_3 test strips in the vicinity of the region irradiated with the plasma jet became much darker. The O_3 concentration was >210 μg/m^3. The diameter of the white area was ~12 mm. From the above findings, the diameter of the region over which the plasma extended was found to increase with increasing applied voltage. However, the diameter of the region where no O_3 was generated (white area) remained the same because the diameter of the area on the O_3 test strips that came into contact with the plasma jet remained the same. From these results, it was found that the O_3 concentration in the vicinity of an object increased with increasing applied voltage.

3.2.3 *Dependence of distribution of O_3 concentration on irradiation distance*

Figure 8 shows photographs of plasma jet irradiation and O_3

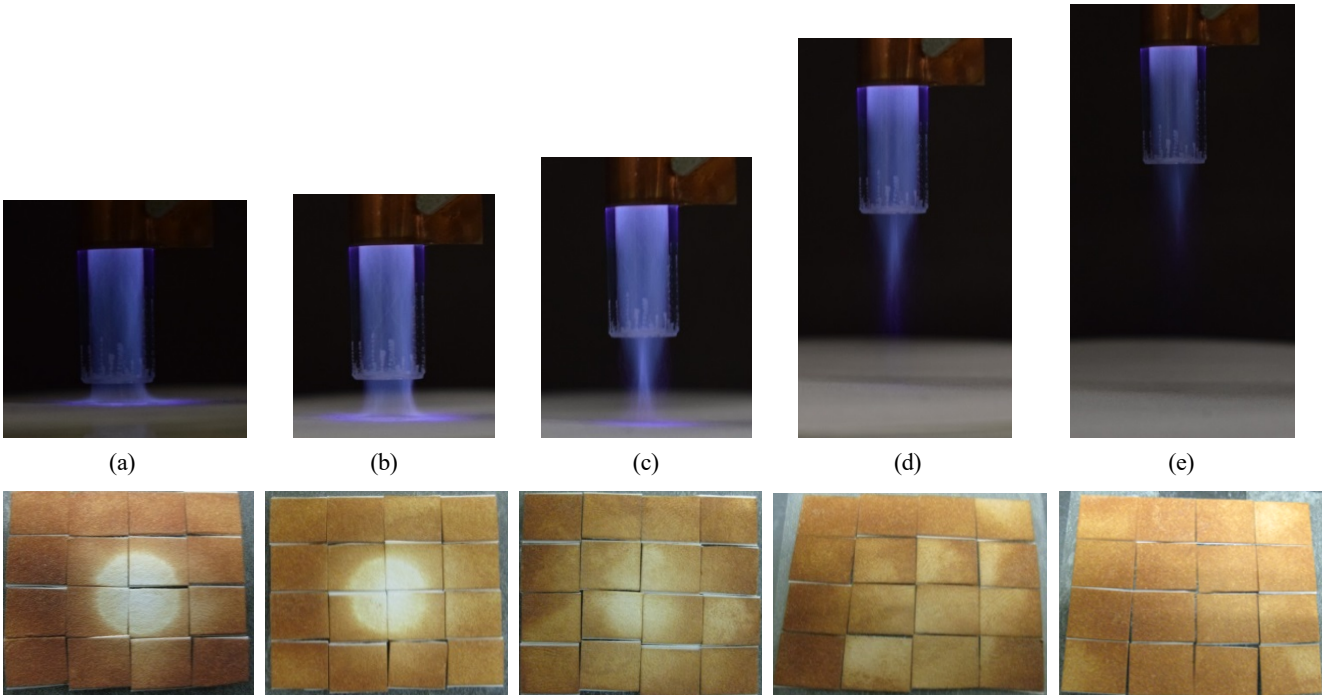

Fig. 8 Photographs of atmospheric-pressure Ar plasma jet irradiation and O_3 test strips irradiated with plasma jet for different irradiation distances (applied voltage, 10 kV; gas flow rate, 10 L/min; irradiation duration, 10 s) (a, f) 2 mm, (b, g) 5 mm, (c, h) 10 mm, (d, i) 20 mm, and (e, j) 30 mm.

test strips irradiated with the plasma jet for different irradiation distances. At irradiation distances of 2–10 mm [Figs. 8(a)–8(c)], a plasma jet was ejected from the quartz tube, came into contact with the filter paper, and then extended horizontally over the filter paper. However, at an irradiation distance of 20 mm [Fig. 8(d)] or 30 mm [Fig. 8(e)], a plasma jet ejected from the quartz tube did not come into contact with the filter paper. The diameters of the region over which the plasma extended were ~18, ~16, and ~13 mm at irradiation distances of 2, 5, and 10 mm, respectively. At irradiation distances of 2–10 mm [Figs. 8(f)–8(h)], the color of the region irradiated with the plasma jet remained white and the color of the O_3 test strips in the vicinity of this region turned brown. The O_3 concentration was >210 μg/m^3 regardless of the irradiation distance. The diameters of the white area were ~14, ~13, and ~11 mm at irradiation distances of 2, 5, and 10 mm, respectively. However, there were no white areas on the O_3 test strips at an irradiation distance of 20 or 30 mm, indicating that the diameter of the white area decreases with increasing irradiation distance. From these findings, when the irradiation distance was small (2–10 mm), no O_3 was generated in the region irradiated with the plasma jet and the effect of O_3 was not expected in this region. In contrast, when the irradiation distance was large (≥20 mm), the plasma jet did not come into contact with the object but the O_3 generated at the edge of the plasma was diffused over the vicinity of the target. Therefore, the effect of O_3 is expected when the irradiation distance is large.

4. Conclusions

The distributions of O_3 concentration generated by atmospheric-pressure Ar plasma jet ejection in air and irradiation on an object were visualized using O_3 test strips. The dependences of the distribution of O_3 concentration on plasma ejection/irradiation duration, applied voltage, and irradiation distance were clarified.

When the plasma jet was ejected into air, the color of the O_3 test strips that came into contact with the plasma jet remained white, but the color of the O_3 test strips in the vicinity of that region turned brown. The region of the shape of plasma jet ejection (inverted triangle) was white on the O_3 test strips. The O_3 concentration in the vicinity of the region was found to increase with increasing plasma ejection duration, and applied voltage.

When an object was irradiated with the plasma jet, the

color of the O_3 test strips irradiated with the plasma jet remained white but that in the vicinity of that region turned brown. The shape of the white area was circular. The O_3 concentration in the vicinity of the object was found to increase with increasing irradiation duration and applied voltage. The manner of contact between the plasma jet and the O_3 test strips differed depending on the irradiation distance. When the irradiation distance was large (≥20 mm), the plasma did not come into contact with the O_3 test strips and the entirety of the O_3 test strips turned brown. In contrast, when the irradiation distance was small (2–10 mm), the color of the O_3 test strips irradiated with the plasma jet remained white but the color in the vicinity of that region turned brown. The shape of the white area was circular. In addition, when the irradiation distance was smaller, no O_3 was generated at the region where the plasma came into contact with the O_3 test strips and the effect of O_3 is not expected in this region. Therefore, to induce the effect of O_3 on an object, it is necessary to eject the plasma jet from above the object so that the plasma jet does not come into contact with the object.

The results of this study demonstrated that the visualization of the distribution of the O_3 concentration generated by atmospheric-pressure plasma jet ejection into air and irradiation onto an object was possible using O_3 test strips.

References

1) S. Kanazawa, M. Kogama, T. Moriwaki, and S. Okazaki, Stable glow plasma at atmospheric pressure, J. Phys. D: Appl. Phys. **21** p.838 (1988).
2) M. C. Kim, S. H. Yang, J. –H. Boo, and J. H. Han, Surface treatment of metals using an atmospheric pressure plasma jet and their surface characteristics, Surf. Coatings Technol. **174-175** p.839 (2003).
3) Z. Fang, Y. Qiu, and E. Kuffel, Formation of hydrophobic coating on glass surface using atmospheric pressure non-thermal plasma in ambient air, J. Phys. D: Appl. Phys. **37** p.2261 (2004).
4) H. Kuwahata, T. Haraki, and I. Mikami, Superhydrophilization of Si Surface by Atmospheric-Pressure Plasma Jet Irradiation: Analysis by Time-of-Flight Secondary Ion Mass Spectrometry (TOF-SIMS), e-J. Surf. Sci. Nanotechnol. **11** p.36 (2013).
5) H. Kuwahata and T. Yamaguchi, Removal of Aluminum on Glass Substrate by Atmospheric-Pressure Plasma Jet Irradiation, e-J. Surf. Sci. Nanotechnol. **14** p.231 (2016).
6) H. Kuwahata, Y. Murata, N. Hashimoto, and R. Segawa, Superhydrophilization of Surface of Aluminum Thin Film by Atmospheric-Pressure Plasma Jet Irradiation, e-J. Surf. Sci. Nanotechnol. **16** p.27 (2018).
7) W. F. L. M. Hoeben, E. M. van Veldhuizen, W. R. Rutgers, and G. M. W. Kroesen, Gas phase corona discharges for oxidation of phenol in an aqueous solution, J. Phys. D: Appl. Phys. **32** L133 (1999).
8) T. Kuroki, K. Yoshida, H. Watanabe, M. Okubo, and T. Yamamoto, Decomposition of Trace Phenol in Solution Using Gas–Liquid Interface Discharge, Jpn. J. Appl. Phys. **45** p.4296 (2006).
9) H. Kuwahata, K. Kimura, and R. Ohyama, Decolorization of Methylene Blue Aqueous Solution by Atmospheric-Pressure Plasma Jet, e-J. Surf. Sci. Nanotechnol. **8** p.381 (2010).
10) M. Uchida, S. Kezuka, Y. Oda, M. Isomura, and H. Kuwahata, Decolorization of Methylen Blue Aqueous Solution by Atmospheric-Pressure Plasma Jet Irradiation: NMR and MS Analyses, Proc. Sch. Eng. Tokai Univ., Ser. J, **56** p.9 (2016) [in Japanese].
11) M. Laroussi and X. Lu, Room-temperature atmospheric pressure plasma plume for biomedical applications, Appl. Phys. Lett. **87**, p.113902 (2005).
12) S. Ikawa, K. Kitano, and S. Hamaguchi, Effects of pH on Bacterial Inactivation in Aqueous Solutions due to Low-Temperature Atmospheric Pressure Plasma Application, Plasma Process. Polym. **7** p.33 (2010).
13) H. Kuwahata, E. Kumazawa, R. Ohyama, and A. Itou, Scanning Electron Microscopy Image of Escherichia Coli Exposed with Atmospheric-Pressure Plasma Jet, e-J.Surf. Sci. Nanotechnol. **8** p.74 (2010).
14) K. Oehmigen, J. Winter, M. Hähnel, C. Wilke, R. Brandenburg, K. D. Weltmann, and T. von Woedtke, Estimation of Possible Mechanisms of Escherichia coli Inactivation by Plasma Treated Sodium Chloride Solution, Plasma Process. Polym. **8** p.904 (2011).
15) H. Kuwahata, T. Yamaguchi, R. Ohyama, and A. Ito, Inactivation of Escherichia coli using atmospheric-pressure plasma jet, Jpn. J. Appl. Phys. **54** 01AG08 (2015).
16) G. Fridman, G. Friedman, A. Gutsol, A. B. Shekhter, V. N. Vasilets, and A. Fridman, Applied Plasma Medicine, Plasma Process. Polym. **5** p.503 (2008).

17) M. G. Kong, G. Kroesen, G. Morfill, T. Nosenko, T. Shimizu, J. van Dijk, and J. L. Zimmermann, Plasma medicine: an introductory review, New J. Phys. **11** p.115012 (2009).

18) G. Y. Park, S. J. Park, M. Y. Choi, I. G. Koo, J. H. Byun, J. W. Hong, G. J. Sim, J. Y. Collins, and J. K. Lee, Atmospheric-pressure plasma sources for biomedical applications, Plasma Sources Sci. Technol. **21** 043001 (2012).

19) T. von Woedtke, S. Reuter, K. Masur, and K. -D. Weltmann, Plasmas for medicine, Phys. Rep. **530** p.291 (2013).

20) M. Laroussi, Low-Temperature Plasmas for Medicine?, IEEE Trans. Plasma Sci. **37** p. 714 (2009).

21) S. U. Kalghatgi, G. Fridman, M. Cooper, M. Nagaraj, M. Peddinghaus, M. Balasubramanian, V. N. Vasilets, A. F. Gutsol, A. Fridman, and G. Friedman, Mechanism of Blood Coagulation by Nonthermal Atmospheric Pressure Dielectric Barrier Discharge Plasma, IEEE Trans. Plasma Sci. **35** p.1559 (2007).

22) G. Isbary, G. Morfill, H. U. Schmidt, M. Georgi, K. Ramrath, J. Heinlin, S. Karrer, M. Landthaler, T. Shimizu, B. Steffes, W. Bunk, R. Monetti, J. L. Zimmermann, R. Pompl, and W. Stolz, A first prospective randomized controlled trial to decrease bacterial load using cold atmospheric argon plasma on chronic wounds in patients, Br. J. Dermatol. **163** p.78 (2010).

23) S. Kalghatgi, G. Friedman, A. Fridman, and A. M. Clyne, Endothelial Cell Proliferation is Enhanced by Low Dose Non-Thermal Plasma Through Fibroblast Growth Factor-2 Release, Ann. Biomed. Eng. **38** p.748 (2010).

24) G. Fridman, A. Shereshevsky, M. M. Jost, A. D. Brooks, A. Fridman, A. Gutsol, V. Vasilets, and G. Friedman, Floating Electrode Dielectric Barrier Discharge Plasma in Air Promoting Apoptotic Behavior in Melanoma Skin Cancer Cell Lines, Plasma Chem. Plasma Process. **27** p.163 (2007).

25) S. Iseki, K. Nakamura, M. Hayashi, H. Tanaka, H. Kondo, H. Kajiyama, H. Kano, F. Kikkawa, and M. Hori, Selective killing of ovarian cancer cells through induction of apoptosis by nonequilibrium atmospheric pressure plasma, Appl. Phys. Lett. **100** p.113702 (2012).

26) A. R. Gibson, H. O. McCarthy, A. A. Ali, D. O'Connell, and W. G. Graham, Interactions of a Non-Thermal Atmospheric Pressure Plasma Effluent with PC-3 Prostate Cancer Cells, Plasma Process. Polym. **11** p. 1142 (2014).

27) Y. Ogawa, N. Morikawa, A. Ohkubo-Suzuki, S. Miyoshi, H. Awakawa, Y.Kita, and S. Nishimura, An epoch-making application of discharge plasma phenomenon to gene-transfer, Biotechnol. Bioeng. **92** p.865 (2005).

28) Y. Sakai, V. Khajoee, Y. Ogawa, K. Kusuhara, Y. Katayama, T. Hara, A novel transfection method for mammalian cells using gas plasma, J. Biotechnol. **121** p. 299 (2006).

29) M. Leduc, D. Guay, R. L. Leask, and S. Coulombe, Cell permeabilization using a non-thermal plasma, New J. Phys. **11** p. 115021 (2009).

30) T. Nakajima, H. Yasuda, H. Kurita, K. Takashima, and A. Mizuno, Generation of Bactericidal Factors in the Liquid Phase and Approach to New Gene Transfer Technology by Low Temperature Plasma Jet Treatment, Int. J. Plasma Environ. Soc. Technol. **5** p.42 (2011).

31) S. Sasaki, M. Kanzaki, and T. Kaneko, Highly efficient and minimally invasive transfection using time-controlled irradiation of atmospheric-pressure plasma, Appl. Phys. Express **7** 026202 (2014).

32) J. C. Devins, Mechanism of Ozone Formation in the Silent Electric Discharge, J. Electrochem. Soc. **103** p. 460 (1956).

33) J. S. Chang, P. A. Lawless, and T. Yamamoto, Corona Discharge Processes, IEEE Trans. Plasma Sci. **19** p. 1152 (1991).

34) I. Somiya, The Ozone: I. Introduction on Ozonation, T. IEE Japan **114**-D p. 353 (1994) [in Japanese].

35) T. Ishijima, H. Hotta, H. Sugai, and M Sato, Multibubble plasma production and solvent decomposition in water by slot-excited microwave discharge, Appl. Phys. Lett. **91** p. 121501 (2007).

36) S. Kühn, N. Bibinov, R. Gesche, and P. Awakowicz, Non-thermal atmospheric pressure HF plasma source: generation of nitric oxide and ozone for bio-medical applications, Plasma Sources Sci. Thchnol. **19** 015013 (2010).

37) S. Reuter, J. Winter, S. Iseni, S. Peters, A. Schmidt-Bleker, M. Dünnbier, J. Schäfer, R. Foest, and K. -D. Weltmann, Detection of ozone in a MHz argon plasma bullet jet, Plasma Sources Sci. Thchnol. **21** 034015 (2012).

38) J. Winter, M. Dünnbier, A. Schmidt-Bleker, A. Meshchanov, S. Reuter, and K. D. Weltmann, Aspects of

UV-absorption spectroscopy on ozone in effluents of plasma jets operated in air, J. Phys. D: Appl. Phys. **45** p.385201 (2012).

39) S. Zhang, W. van Gaens, B. van Gessel, S. Hofmann, E. van Veldhuizen, A. Bogaerts, and P. Bruggeman, Spatially resolved ozone densities and gas temperatures in a time modulated RF driven atmospheric pressure plasma jet: an analysis of the production and destruction mechanisms, J. Phys. D: Appl. Phys. **46** p. 205202 (2013).

40) J. Winter, K. Wende, K. Masur, S. Iseni, M. Dünnbier, M. U. Hammer, H. Tresp, K. -D .Weltmann, and S. Reuter, Feed gas humidity: a vital parameter affecting a cold atmospheric-pressure plasma jet and plasma-treated human skin cells, J. Phys. D: Appl. Phys. p. 29540146 (2013).

41) X. L. Deng, A. Yu. Nikiforov, P. Vanraes, and Ch. Leys, Direct current plasma jet at atmospheric pressure operating in nitrogen and air, J. Appl. Phys. **113** 023305 (2013).

42) D. Ellerweg, A. von Keudell, and J. Benedikt, Unexpected O and O_3 production in the effluent of He/O_2 microplasma jets emanating into ambient air, Plasma Sources Sci. Technol. **21** 034019 (2012).

43) H. Kuwahata and T. Yamaguchi, Two-Dimensional Concentration Distribution of Hydrogen Peroxide Generated by Atmospheric-Pressure Plasma Jet Irradiation, e-J. Surf. Sci. Nanotechnol. **13** p.474 (2015).

44) R. Ohyama and A. Nagai, Japan Patent 244938 (2006).

Proc. Schl. Eng. Tokai Univ., Ser. E
45 (2020) 17-25
DOI: 10.18995/24343641.45.17

2D Hydrodynamic Simulation Model for Dam-Break Based on the Finite Difference Method

by

Sayed Masihullah AHMADI[*1], Yoshimichi YAMAMOTO[*2] and Maiki HAYAKAWA[*3]

(Received in Mar. 30, 2020, and accepted in June 19, 2020)

Abstract

Dam-break disasters keep happening many times each year all over the world. Examples from 2018 to early 2019 include the Brumadinho dam in Brazil, Swar Chaung dam in Myanmar, Xe-Pian Xe-Namnoy dam in Laos, Panjshir Valley dam in Afghanistan and Patel dam in Kenya. Each of these dam-breaks caused hundreds of fatalities or missing persons, with thousands of others being made homeless. The fact that causes of dam-breaks differ means that they are inevitable, therefore governments or companies that are responsible for the safety of a dam should always consider preparing hazard maps. Accordingly, investigation and research on dam-breaks are crucially important. This paper presents a two-dimensional simulation model assuming a rectangular-shape dam-break section of a dam with a reservoir. The model can calculate flow velocity and inundation heights at various time points from the time of the break. The hydrodynamics of the model are calculated using two-dimensional nonlinear shallow water equations, which are solved by the finite difference method. To verify the applicability of the model, the tsunami caused by the 2011 Great East Japan Earthquake is simulated in the Sendai-Natori area with acceptable relative accuracy, and then the Amagase dam-break is simulated as an example.

***Keywords*:** Shallow water equation, Dam-break model, Long-wave flood, Hydrodynamic simulation model

1. Introduction

There are many hydrodynamic simulation models for a dam-break scenario, which are capable of simulating both 2D and 3D models. To name a few of the accurate models for simulation of the flood due to a dam-break. HEC-RAS V.5, MIKE 21 and TUFLOW models are among the most famous flood simulation models that are available for either educational or business purposes. These software can evaluate the extent of the flooded area, flood distribution depths at times, flood velocities at times, flood arrival times to target locations, and the respected flood duration. These software are already extensively being used for different hydrodynamic flood simulation purposes and there are many researchers who have confirmed their accuracy specifically for dam-break scenarios like “Landslide dam and subsequent dam-break flood estimation using HEC-RAS model in Northern Pakistan” (Butt, Umar, and Qamar 2013)[1].

To verify the dam-break simulation model, we need real case dam-break data to compare the simulation results with them and then discuss the accuracy of the model. Because it is difficult to find and measure the hydrodynamic data in case of a dam-break, in this paper, we introduce a flood simulation model that we had developed for tsunami simulations and have confirmed its reproducing ability by simulating some flood cases due to existing tsunamis. Because in the literature, floods due to a tsunami and a dam-break are categorized into the same long-wave motion or in other words, a flood is expressed with the same motion equation as that of tsunami since the flood is the plane 2D nonlinear long-wave like a tsunami. Therefore, we have only to input water from the mountainside instead of inputting water from the sea. Moreover, existing numerical models developed for a river flow are applicable only to movement, which always flows

*1 Architecture and Civil Engineering Course, Graduate School of Science and Technology, Tokai University, Hiratsuka, Kanagawa, Japan,

*2 Department of Civil Engineering, School of Engineering, Tokai University, Hiratsuka, Kanagawa, Japan,

*3 Graduate School of Engineering, Tokai University, ditto.

from the upstream side to the downstream side of the river. However, when the flood overflowed out of the river, since a device to run-up process is necessary at uphill places, we had better use the numerical model for tsunami, which is applicable to uphill places. With this in mind, we could modify our model for dam-break flood-simulation purpose with minor changes on an input method. Our proposed model solves the continuity equation (Eq.(1)) and the two-dimensional non-linear shallow water equation (Eq. (2&3)), by finite difference method using the Crank-Nicholson scheme. As a numerical simulation method using a digital computer, since use of FDM is the very rational, FDM has been vastly used in numerical simulations of the hydrodynamics field, and many support programs exist. Therefore, we adopted FDM. For the data input purpose of the model, we need to have the real topography of downstream of the dam to the desired extent. It is worth mentioning that the wider we choose the target area, the higher capacity of workstation-computer is required. The model has a side application software (CONTWIN) which is able to convert Digital Elevation Models (DEM) or DXF format of topography maps into the desired grids. The accuracy of the calculations can be controlled based on the mesh size we choose in this step. Break dimension (width and height), dam basin area and discharge volume, calculation range, desired calculation time interval, land use data (the ratio of buildings, forests, cultivation and flat area in a mesh) are input data sets.

To confirm the accuracy of the proposed model in the case of hydrodynamics, the flood simulation due to a tsunami is executed on the Sendai-Natori area.

To confirm the workability of our simulation model, we chose Amagase dam, located in Kyoto Prefecture of Japan as a sample dam-break scenario. The main purpose of the Amagase dam is flood control and the dam was constructed in 1964. The dam is a 73 m tall, 254 m long variable-radius arch type with a structural volume of 162,000 m^3. The dam withholds a reservoir called Lake Hōō (Hōō-ko, lit. "Lake Phoenix") of 26,280,000 m^3 of which 20,000,000 m^3 is active or "useful" storage. It has a surface area of 1.9 km^2 and it is worth mentioning that at the downstream of Amagase Dam, there is a densely populated residential area of over 100,000 individuals which can be a reason for this simulation.

2. Calculation Methods

Since there are many numerical methods for dam-break flows. They can be classified into three broad types: finite-difference methods, finite-element methods, and finite volume methods (Zhang and Wu 2011)[2]. In this paper, we have used the finite-difference method to solve the hydrodynamic equations. For hydrodynamic calculations, we have used the popular equation of continuity (Eq.(1)) and two-dimensional nonlinear shallow water equations (Eq. (2 & 3)).

$$\frac{\partial f_y q_x}{\partial x}+\frac{\partial f_x q_y}{\partial y}+\frac{\partial S\eta}{\partial t}=0 \tag{1}$$

$$\begin{aligned}&\frac{\partial q_x}{\partial t}+\frac{1}{S}\frac{\partial}{\partial x}\left(\frac{Sq_x^2}{d}\right)+\frac{1}{S}\frac{\partial}{\partial y}\left(\frac{Sq_x q_y}{d}\right)+\\&gd\frac{\partial \eta}{\partial x}-\frac{1}{S}\frac{\partial}{\partial x}\left[d\nu_t S\frac{\partial(q_x/d)}{\partial x}\right]-\\&\frac{1}{S}\frac{\partial}{\partial y}\left[d\nu_t S\frac{\partial(q_x/d)}{\partial y}\right]+\frac{f_c}{d^2}Qq_x=0\end{aligned} \tag{2}$$

$$\begin{aligned}&\frac{\partial q_y}{\partial t}+\frac{1}{S}\frac{\partial}{\partial x}\left(\frac{Sq_y q_x}{d}\right)+\frac{1}{S}\frac{\partial}{\partial y}\left(\frac{Sq_y^2}{d}\right)+\\&gd\frac{\partial \eta}{\partial y}-\frac{1}{S}\frac{\partial}{\partial x}\left[d\nu_t S\frac{\partial(q_y/d)}{\partial x}\right]-\\&\frac{1}{S}\frac{\partial}{\partial y}\left[d\nu_t S\frac{\partial(q_y/d)}{\partial y}\right]+\frac{f_c}{d^2}Qq_y=0\end{aligned} \tag{3}$$

Where q_x & q_y are the horizontal fluid fluxes in the x & y directions respectively. η is the water surface elevation, f_x & f_y are the x & y direction ratios of the wet portion in a calculation mesh. S is the area ratio of the wet portion in a calculation mesh. d is the water depth from the static water surface η. g is the gravitational acceleration, ν_t is the eddy viscosity coefficient. $Q=\sqrt{q_x^2+q_y^2}$ is the compound value of q_x & q_y. To calculate the bottom friction coefficient, the following equations are used;

$$f_c=\frac{gn^2}{d^{1/3}} \tag{4}$$

$$n^2=n_0{}^2+0.020\frac{\theta}{100-\theta}d^{4/3} \tag{5}$$

$$n_0{}^2=\frac{n_1{}^2A_1+n_2{}^2A_2+n_3{}^2A_3}{A_1+A_2+A_3} \tag{6}$$

Here, n is the Manning's roughness coefficient. θ is the building ratio (= the ratio of the area of all vertical objects like houses and trees to the mesh area). n_0 is the weighted average roughness coefficient of areas like farms, roads, and waste& wetlands, $A_{1,2,\&3}$, with relative roughness coefficients of $n_{1,2,\&3}$.

The cause for a dam-break is varied in each dam-break case where the most common causes can be great earthquakes, overtopping due to heavy flash floods (this failure cause is expected to increase in the following decades due to climate changes) and the aging of a dam. A more complete list of the most prominent causes of dam-break are listed in the US Army Corps of Engineers Hydrologic Engineering Center, Flood Emergency Plans, Guidelines for Corps Dams as (1)

Earthquake; (2) Landslide; (3) Extreme storm; (4) Piping; (5) Equipment malfunction; (6) Structure damage; (7) Foundation failure; (8) Sabotage (Owen 1980)[3]. For each of these different failure causes, the break sections may vary which means the discharge rate is sentenced to change as well. This change in the rate of discharge makes the simulation and accurate calculations very complex. Many researchers have already developed models to simulate the dam breach scenarios on different types of dams and as well as different failure cases. "Methodology for Earthen Dam Breach Analysis" (Yue Sheng, Damisse Emile, and Ansar Matahel 2016)[4], "Hydrodynamic Dam Breach Modelling of Earthfill Saddle Dam" (Sidek 2011)[5], "Analysis of Hydrograph by Dam Breach Shapes" (ki-bum Park 2019)[6] are some of the papers which concentrates more on the failure shapes and the discharge rates of different dam type's failure with various break sections, however, in this paper, the main focus is the flood plain and hydrodynamics calculations following a dam-break. For this purpose, we have assumed a trapezoidal break section and derived new equations for calculating a run-off rate to this dam-break as follows;

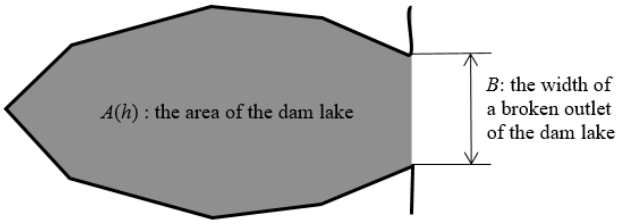

Fig. 1 Dam-break section plan view.

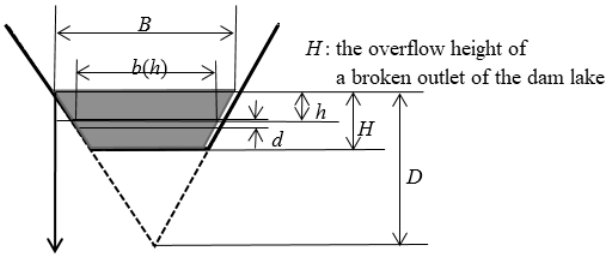

Fig. 2 Dam-break cross-section view.

The run-off rate from the dam lake in the case that the overflow height H is constant (water supply is infinite) can be calculated from bellow equations;

$$Q = \int_0^H b(h) \times c\sqrt{2gh}\, dh = \int_0^H \frac{B(D-h)}{D} c\sqrt{2gh} dh \tag{7}$$

$$Q = \frac{B}{D} c\sqrt{2gh}\left[D\frac{2}{3}h^{3/2} - \frac{2}{5}h^{5/2}\right]_0^H \tag{8}$$

$$Q = \frac{B}{D} c\sqrt{2g}\left(\frac{2}{3}DH^{3/2} - \frac{2}{5}H^{5/2}\right) \tag{9}$$

Since the case of finite water supply from a dam lake is more realistic in the actual dam-break cases, in this paper, we have used the equation for run-off rate from the dam lake by following equations;

$$Q = A(h) \times \frac{dh}{dt} \tag{10}$$

$$Q = \frac{B}{D} c\sqrt{2g}\left(\frac{2}{3}D\left(H - \frac{dh}{dt}T\right)^{3/2} - \frac{2}{5}\left(H - \frac{dh}{dt}T\right)^{5/2}\right) \tag{11}$$

Here, T is the run-off elapse time (sec), V is the total volume of discharge water, and c is the flow rate coefficient (=0.61).

$$V = \int_0^H A(h)dh = \int_0^{H/\frac{dh}{dt}} QdT \tag{12}$$

$$V = \int_0^{H/\frac{dh}{dt}} \frac{B}{D} c\sqrt{2g}\left(\frac{2}{3}D\left(H - \frac{dh}{dt}T\right)^{3/2} - \frac{2}{5}\left(H - \frac{dh}{dt}T\right)^{5/2}\right)dT \tag{13}$$

$$= \frac{B}{D} c\sqrt{2g}\frac{1}{dh/dt}\int_H^0 \left(\frac{2}{3}DX^{3/2} - \frac{2}{5}X^{5/2}\right)dX \tag{14}$$

$$= \frac{B}{D} c\sqrt{2g}\frac{1}{dh/dt}\left[\frac{4}{15}DX^{5/2} - \frac{4}{35}X^{7/2}\right]_H^0 \tag{15}$$

$$Here, X = H - \frac{dh}{dt}T \tag{16}$$

$$\frac{dX}{dT} \approx \frac{dh}{dt}\ , T = 0 \to T = \frac{H}{dh/dt}, X = H \to X = 0 \tag{17}$$

Thus,

$$\therefore V = \frac{B}{D} c\sqrt{2g}\frac{+1}{dh/dt}\left(\frac{4}{15}DH^{5/2} - \frac{4}{35}H^{7/2}\right) \tag{18}$$

$$\therefore \frac{dh}{dt} = \frac{Bc\sqrt{2g}}{DV}\left(\frac{4}{15}DH^{5/2} - \frac{4}{35}H^{7/2}\right) \tag{19}$$

$$\therefore T_{total} = \frac{H}{dh/dt} = \frac{DV}{Bc\sqrt{2g}}\frac{1}{\frac{4}{15}DH^{5/2} - \frac{4}{35}H^{7/2}} \tag{20}$$

Here, D is the imaginary depth from the dam crown height and it is assumed 1000m in this simulation.

3. Hydrodynamic verification

For the hydrodynamics verification calculations of our proposed model, the great tsunami of the 2011 Japan earthquake is simulated in the Sendai-Natori area. The destination area is located in Miyagi Prefecture of Japan, where Sendai City is on the north of Natori River and Natori City on the south. Natori River is flowing to the Pacific Ocean, west-east. Fig. 3 shows the existing topography of the area. The ground height from the coastline of less than 4 km is very low. Fig. 4 shows the area ratio of buildings or trees to a mesh, the dark area larger than 30 percent means the area occupied by buildings, the green area larger than 5 percent is the forest area, the yellowish-green area larger than 1 percent is the cultivated & paddy area, and the white area is the sea area. In the numerical simulation model, the mesh size was 25 m.

The incident tidal data on the offing boundary line of this

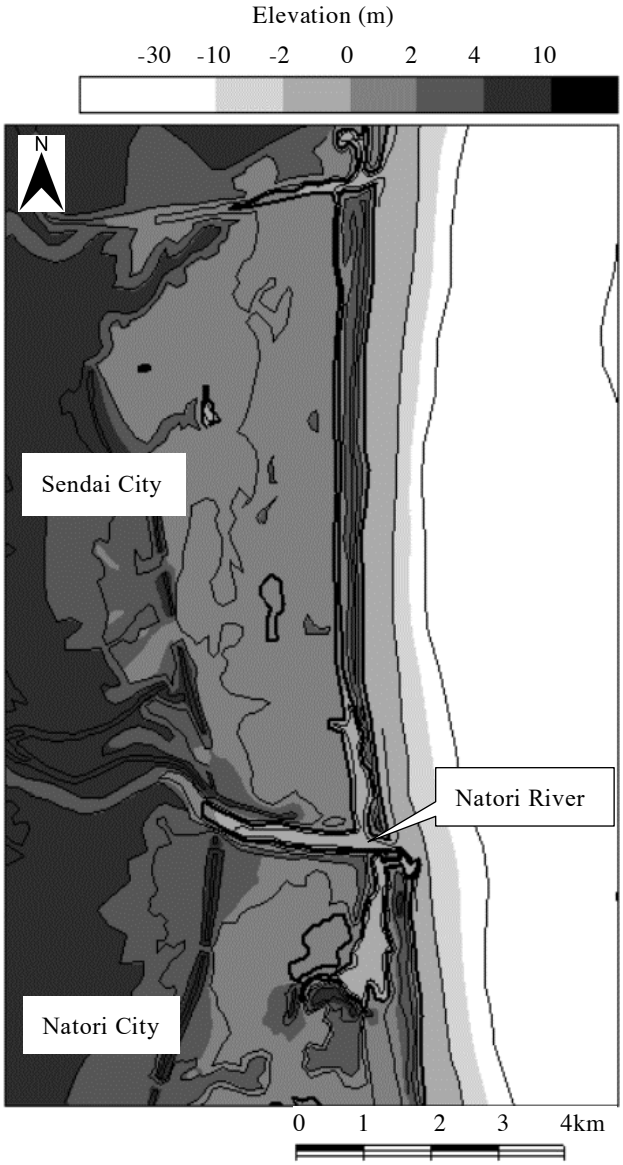

Fig. 3 Topography of calculation area (Sendai - Natori Coast).

simulation was set with reference to Fig. 3.2.3 of Technical Note No.1231 of PARI (2011)[7]. However, since missing data are in the tidal data on the offing of Miyagi Prefecture, average data between Fukushima Prefecture and Iwate Prefecture were used. Moreover, the maximum tidal height on the offing boundary line was estimated to be 10 m, and the time of the incident phase & the whole period of the first wave became 30 minutes and 48 minutes respectively. The maximum tsunami height on the shoreline appears after about 28 minutes of the calculation start, and according to Fig. 5 which shows the water depth in the sea and the inundation height on the land after 28 minutes, the maximum height on the shoreline is 6~12 m. On the other hand, according to Figs. 5.3.8.1~5.3.8.4 of Technical Note No.1231, measured maximum tsunami height is 6~12 m, so the reproduction accuracy of the calculated height is good. The maximum velocity near the coastline is 6~10 m/s as shown in Fig.6 which shows the tsunami velocity in on-offshore direction after 28 minutes. On the other hand, according to Fig. 3 in the paper of Hayashi et al. (2013)[8], since

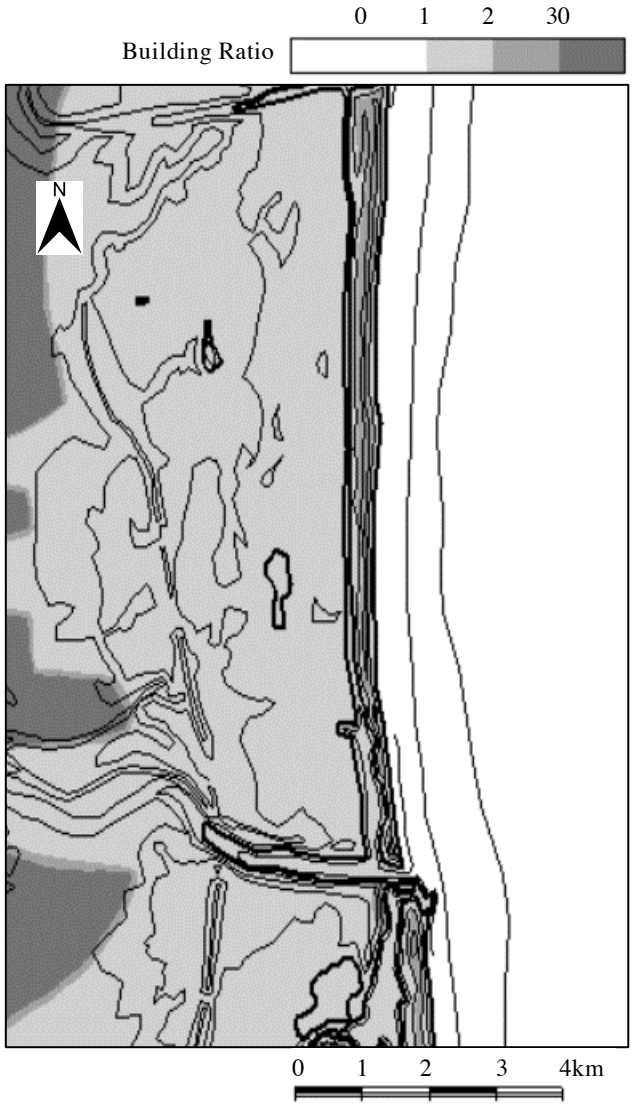

Fig. 4 Area ratio of buildings or trees to a mesh.

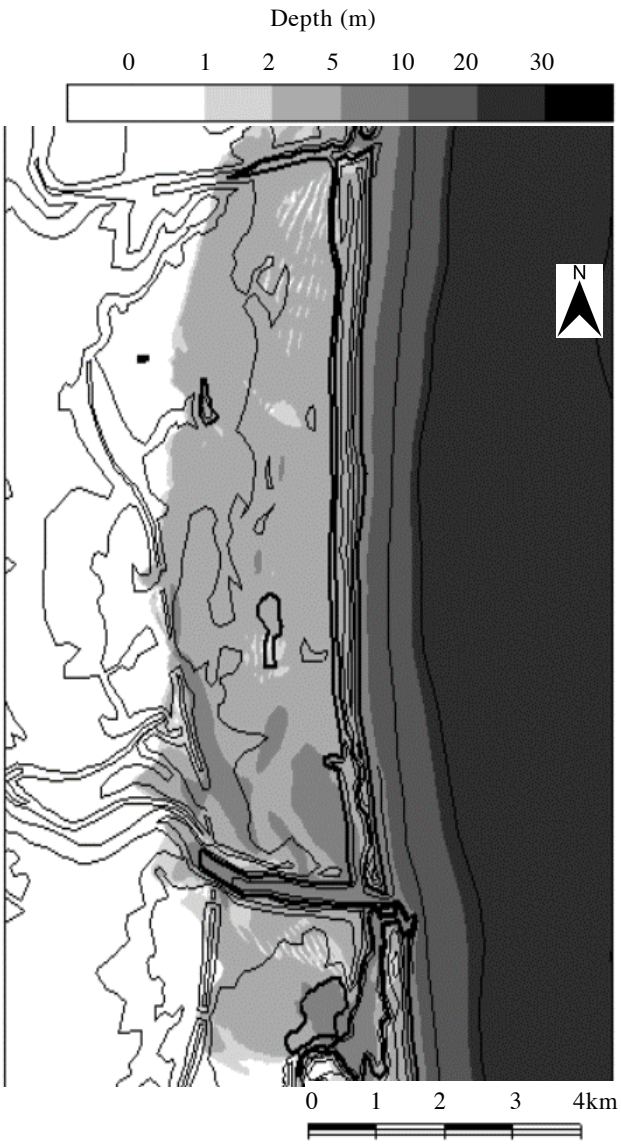

Fig. 5 Water depth in the sea and inundation height of the land after 28 minutes of the calculation start.

Fig. 6 Tsunami velocity after 28 minutes of the calculation start.

the measured maximum velocity near the coastline is 5~8 m/s, the reproduction accuracy of the calculated velocity is moderately good.

4. Amagase Dam-Break Simulation

Amagase Dam is located in Uji city in Kyoto Prefecture Japan. Fig. 7 shows its location on google map. For the break simulation purpose, the height and width of the broken section of Amagase Dam are assumed 50m and 200m respectively. The area of the dam lake is considered as 1,880,000 square meters. Although this dam is not a mega-scale dam when we compare it to other huge dams in the world, it's worth mentioning that, around 100,000 individuals are living downstream of it, where if the dam-breaks, a catastrophic disaster is predictable which makes this practice simulation model a more demanding case.

Fig. 8 shows the topography map and the calculation range, which are used in the simulation. As it is common by other simulation software, our proposed model uses the existing Digital Elevation Models (DEMs) available now worldwide with relatively different accuracies. For this simulation, however, we have used a 10 m accuracy DEM for developing the existing topography meshes. The area ratio of buildings, dense forests or trees, cultivated or paddy area in a mesh is depicted in Fig. 9. (distribution of θ of Eq. (5)). The gray area means the area occupied by all types of buildings and the occupying ratio in a mesh is about 30 percent of a mesh area, the medium gray area shows the heavy forest area which relatively occupies up to 30 percent of a mesh area. The light gray area shows the category of other areas including grass area and light cultivated area. The white area shows the water area.

In the Amagase dam-break simulation model case, the mesh size was set to 20m. The output interval was set to every 60 seconds. The total duration of 2400 seconds was set as the calculation time limits.

Now that the input datasets are ready, using our numerical simulation model, we could generate a set of useful output data. Fig. 10 shows the inundation depths 40 minutes after the dam-break happens. The very light gray and gray color shows a depth of 1-5 meter inundation and dark gray shows a depth of 5-10 meter inundation while dark gray and black area shows depths of 10-20 meter of inundation. According to the inundation height output, a wave of 2-5 meters in height will most probably strike the nearby densely populated area at the downstream which can cause a catastrophic disaster.

Fig. 11 shows the flow velocity 20 minutes after the break. The flow velocity varies from zero to 10 meters per second, which the distribution is depicted by the gray color chart. It's worth mentioning that, since at this time, the amount of return flows (negative velocity) is very small, it is very difficult to distinguish, however, at later calculation times, the model can reproduce the return flows as well.

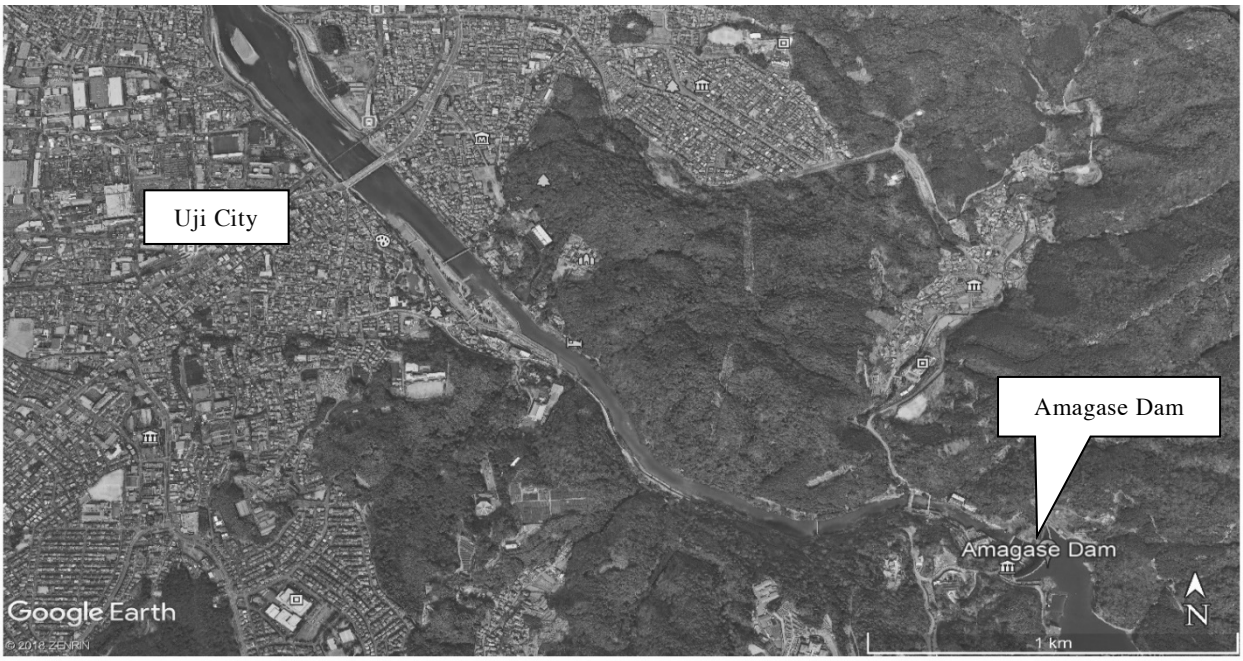

Fig. 7 Amagase dam location (google map).

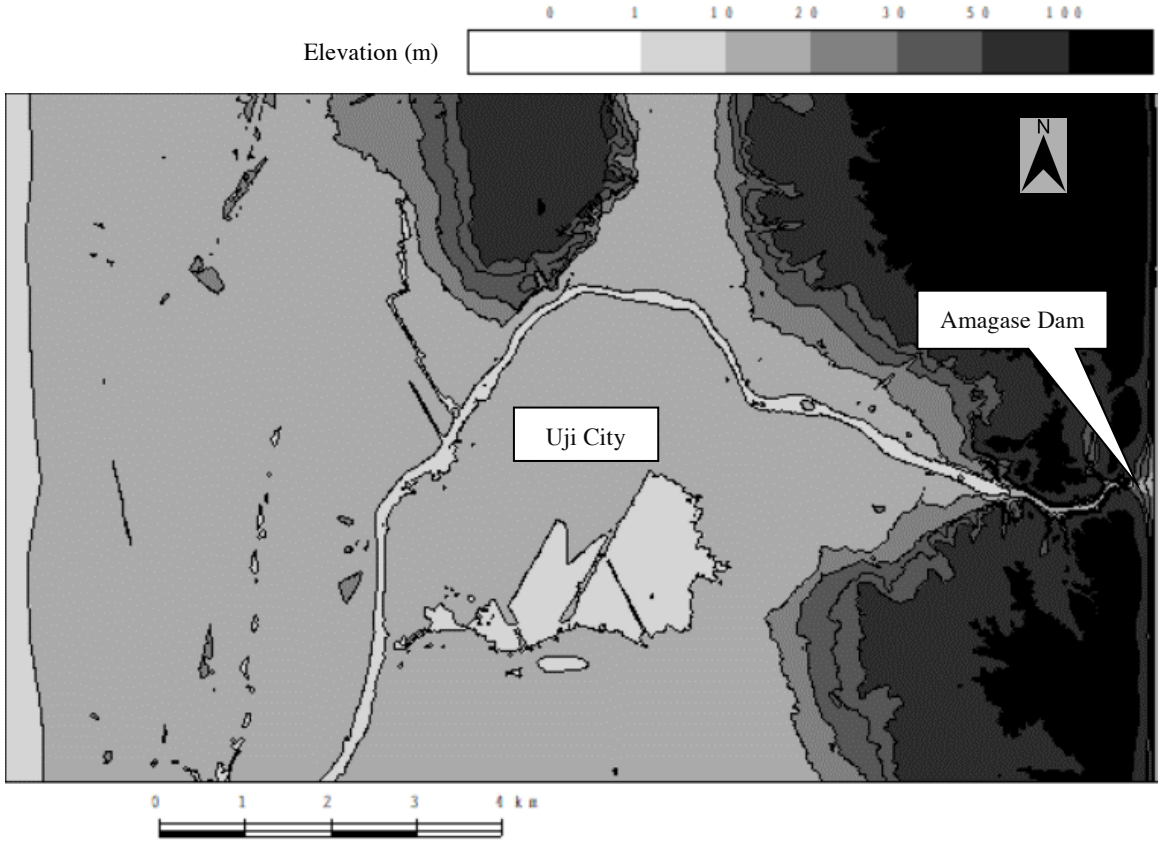

Fig. 8 Topographic map and calculation range.

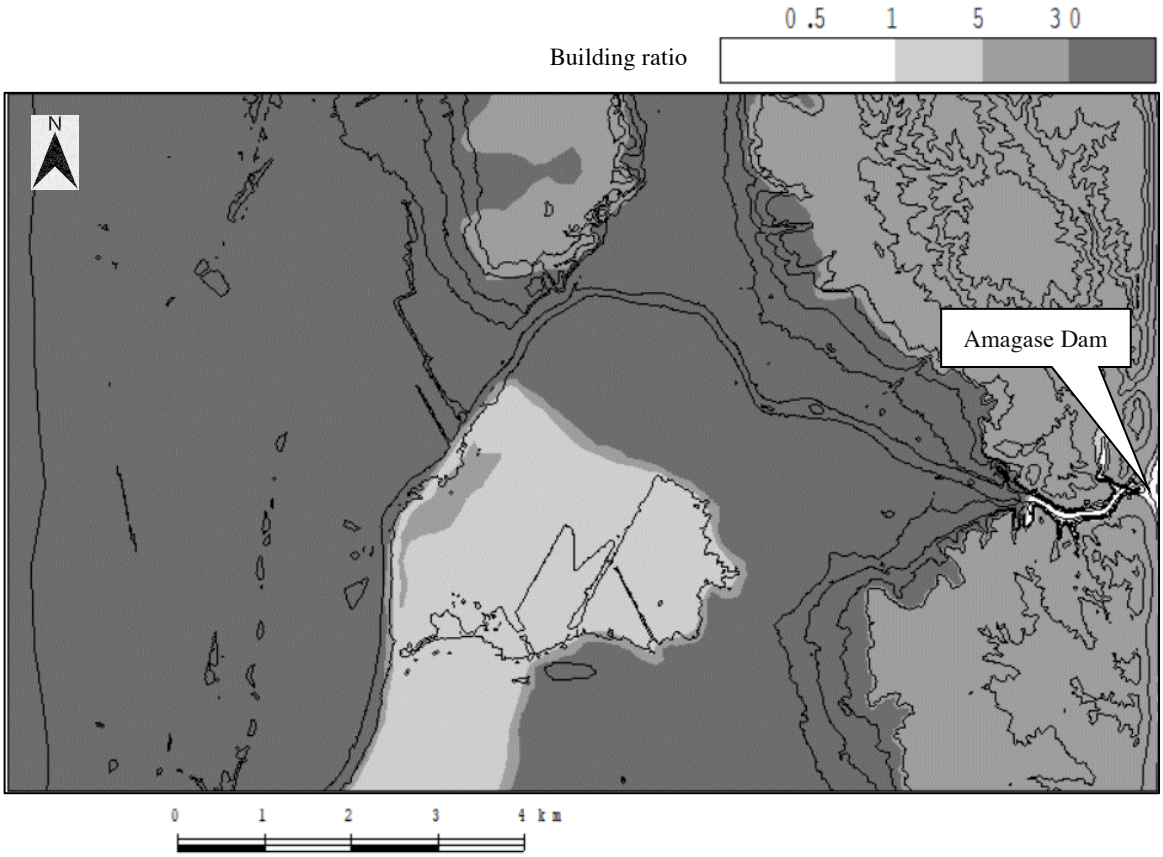

Fig. 9 Area ratio of buildings or trees to a mesh.

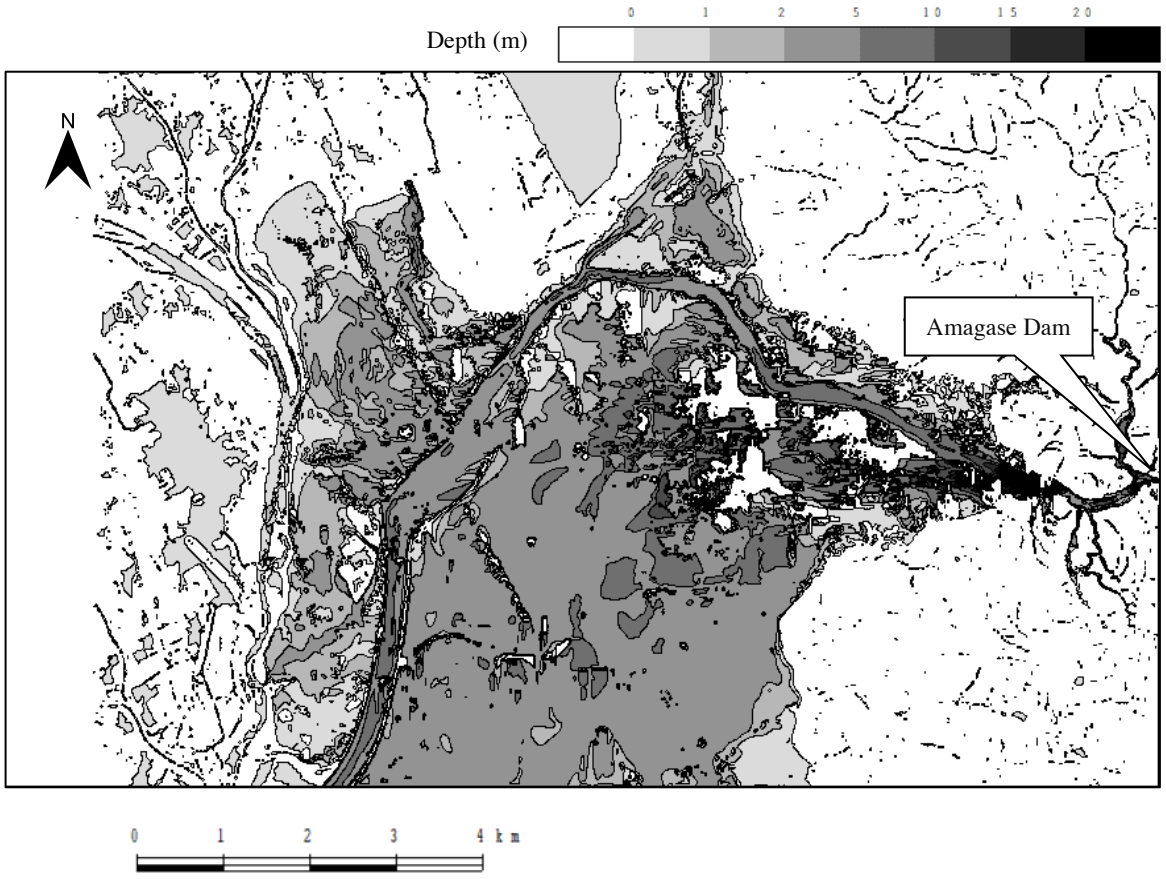

Fig. 10 Inundation depth 40 minutes after the break.

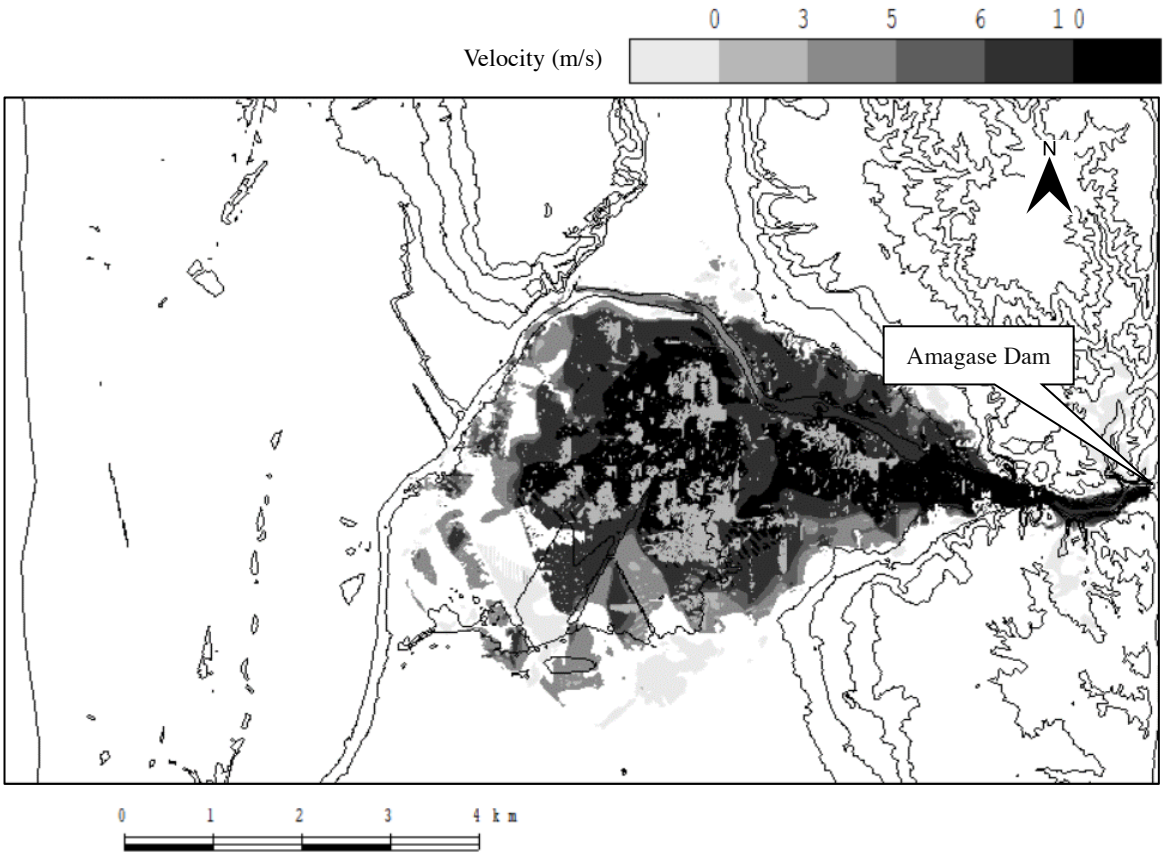

Fig. 11 Flow velocity 20 minutes after the break.

5. Conclusions

In the last decades, the life safety demand has increased in the world while hazards are increasing as well, to balance this situation; we need to focus on safety measures as far as possible. The dam-break or levee failure may lead to huge floods that cause catastrophic damage and life losses if proper considerations are not taken on time. A dam-break may occur due to many reasons such as heavy flush floods, aging, or sabotage. Hence, accurate flood simulation models must be developed which greatly helps in hazard map preparation. Many scientists have already developed flood simulation models either 2D or 3D, which can reproduce almost accurate floods due to dam-breaks, but since the number of variations is too many to consider in a single model, still this topic is under progression and development.

In this paper, a simulation model was presented which uses the common continuity equation and nonlinear two-dimensional shallow water equation for the hydrodynamic calculations. The flood simulation due to the 2011 Japan tsunami executed and evaluated with acceptable results to confirm the applicability of this model and then the same model was modified for the dam-break simulation scenario. For this purpose, the new run-off rate equations were derived and used for discharge calculations from a break section. To confirm the applicability of the proposed model, Amagase dam-breaks simulation is executed. The results of the simulation show the maximum inundation depth of about 20 meters and a wave of 2-5 meter in height will most probably strike the nearby densely-populated area at the downstream of Amagase dam which can cause a catastrophic disaster in case of a dam-break.

6. References

1) Butt, Mohsin Jamil, Muhammad Umar, and Raheel Qamar: Landslide Dam and Subsequent Dam-Break Flood Estimation Using HEC-RAS Model in Northern Pakistan. Natural Hazards Vol.65, No.1, pp.241–254 (2013).
2) Zhang, Mingliang, and W. M. Wu: A Two Dimensional Hydrodynamic and Sediment Transport Model for Dam-break Based on Finite Volume Method with Quadtree Grid. Applied Ocean Research Vol.33, No.4, pp.297–308 (2011).
3) Owen, H. J: Flood Emergency Plans: Guidelines for Corps Dams, Fort Belvoir, VA, Defense Technical Information Center. (1980). http://www.dtic.mil/docs/citations/ADA158679, accessed June 24, 2019.
4) Yue Sheng, Damisse Emile, and Ansar Matahel: Methodology for Earthen Dam Breach Analysis, World Environmental and Water Resources Congress. Proceedings: pp.100–110 (2016).
5) Sidek, Lariyah Mohd: Hydrodynamic Dam Breach Modeling of Earthfill Saddle Dam. Journal of Energy &amp, Environment. (2011). https://www.academia.edu/6434237/Hydrodynamic_Dam_Breach_Modeling_of_Earthfill_Saddle_Dam, accessed June 24, 2019.
6) ki-bum Park: Analysis of Hydrograph by Dam Breach Shapes.ResearchGate. https://www.researchgate.net/publication/263361604_ accessed June 24, 2019.
7) Port and Airport Research Institute “Urgent Survey for 2011 Great East Japan Earthquake and Tsunami Disaster in Ports and Coasts,” Technical Note of PARI, No.1231, p.200 (2011).
8) Hayashi Satomi, Narita Yuya, and Koshimura Shunichi: Developing Tsunami Fragility Curves from the Surveyed Data and Numerical Modeling of the 2011 Tohoku Earthquake Tsunami, Journal of Japan Society of Civil Engineers, B2 (Coastal Engineering), Vol.69, No.2, pp.386-390 (2013).

Proc. Schl. Eng. Tokai Univ., Ser. E
45 (2020) 27-36
DOI: 10.18995/24343641.45.27

Impacts of Development-induced Displacement on Informal Households –A Case Study from Qala-e-Musa, Kabul–

by

Osama HIDAYAT[*1] and Yoshitaka KAJITA[*2]

(Received in Mar. 30, 2020, and accepted in June 19, 2020)

Abstract

Cities in Afghanistan are experiencing unprecedented growth. which is often accompanied by the negative impacts of car-dependent urbanization such as congestion, air pollution, inefficient use of energy and time, and social inequality of accessibility. Therefore, many inner-city neighborhoods need to be upgraded or readjusted to give way to infrastructure and commercial developments, and generally, to a more modern living environment. These ambitions often lead to manifold displacement and resettlement projects that affect the livelihoods of the residents, including many from informal settlements. Based on research conducted in Qala-e-Musa, Kabul, this paper discusses the impacts of project-induced displacement and redevelopment on affected informal settlement households. This study draws on interviews with displaced households, as well as interviews with key informants during field investigation. The findings highlight that displaced informal households in Qala-e-Musa endure several adverse impacts on their physical, financial and social aspects. The study conclusively argues that housing and planning policies should carefully consider the everyday life activities, issues and needs of communities within neighborhoods.

***Keywords*:** Urbanization, Kabul, Informal settlement, Redevelopment, Livelihood impacts

1. Introduction

Urban redevelopment policies in emerging cities of developing courtiers often include land readjustment and displacement projects, which is a substantial threat to informal settlements (Patel, Sliuzas, & Mathur, 2015). Recently adopted visions and development plans of new cities and social housing In Afghanistan are aimed at improving the quality of life of the rapidly growing urbanization and empowering local economies (JICA, 2017). These urban plans require investments in urban infrastructure, public facilities, housing development and other services. The implementation of such plans often has profound implications in terms of inhabitant's relocation. This means the displacement of many urban dwellers, especially the squatter settlements, who are frequently located in central and well-located locations. Urban land acquisition for public and private investments, and the subsequent involuntary development-induced displacement and resettlement processes of urban households through urban renewal and redevelopment policies, are almost inevitable during the current period of fast economic development in many countries (Noorloos & Kloosterboer, 2018). Informal settlements are often the most affected by urban renewal and redevelopment projects (Bogumil Terminski, 2013). The households displaced by such urban development initiatives are either resettled on-site through land-sharing and site reconstruction or off-site, away from their original settlements, mostly in urban peripheries or rural areas

Development-induced displacement and resettlement occur when people are forced to leave their homes and/or land as a result of development. This subset of forced migration has been historically associated with the construction of dams for hydroelectric power and irrigation but is also the result of various development projects such as mining, agriculture, the creation of military installations, airports, industrial plants, railways, road developments, urbanization, conservation projects, and forestry (Davidson, Zaaijer, Peltenburg, & Rodell, 1993; Koenig, 2011).

Development-induced displacement is a social problem affecting multiple levels of residents, from tribal and village

*1 PhD, Fellow, Department of Civil Engineering, Tokai University
*2 Dr. Eng., Prof., Department of Civil Engineering, Tokai University

communities to well-developed urban areas. Development is widely viewed as an inevitable step towards modernization and economic growth in developing countries; however, for those who are displaced, the result is most often the loss of livelihood and impoverishment.

Project-affected peoples have various rights, including the basic human rights that are common to all people everywhere. They also have legal rights, which vary across jurisdictions. They may have customary or traditional rights and entitlements in some instances. There are also international standards governing how resettlement should be undertaken, what compensation should be provided, and what outcomes are expected. However, these rights and standards do not guarantee that the harm from resettlement can be avoided. Projects that are in the indisputable public interest may have land acquisition requirements that necessitate the resettlement of some people. No matter how effectively this resettlement is undertaken, there is always some negative socio-economic impacts. Based on the general introduction some of the key questions arise that; what constitutes appropriate compensation, how effective are the redevelopment processes being implemented and how can resettlement practice be improved (Davidson, Mirjam, Peltenburg, & Rodell, 1993; Viratkapan & Perera, 2006).

The purpose of this study is to set the scene for a discussion of these and related questions by providing a general overview of resettlement practice and the issues that arise in project-induced displacement and resettlement. This paper is intended to raise awareness of the issues associated with resettlement, especially to people in the impact assessment community who may not be fully familiar with resettlement. There is ongoing improvement in the discourse and practice of resettlement (CRIDA, 2019).

In the following section, we give a brief description of the study area, the selected research sites, and introduce the research methodology. Section three discusses the identified displacement and resettlement livelihood impacts on affected informal settlement dwellers in Kabul. In section four, we discuss the implications of the research findings and recommendations for future research directions and the final section presents present our conclusions.

2. Methodology

2.1 *Study area background*

In recent years, Kabul city has expanded into a bustling metropolitan area, the exponential growth in this ancient and important city of Afghanistan has had considerable consequences. From a population perspective, a city which was originally planned for 700,000 people in now home to upwards of five million residents. This surge in population has Kabul grappling with serious challenges including; lack of infrastructure, resources, modern urban management, good governance, access to sustainable human development, provision of public services, equal access to facilities and most importantly dealing effectively with security issues. Security of the capital is of utmost importance with Kabul being home to a considerable concentration of the nation's population as well as housing various diplomatic missions and international organizations. To tackle these challenges, in recent years, numerous important programs are initiated and have been implemented. One such initiative is the alternate road of Wazir Akbar Khan (Qala-e-Musa), this landmark project was initiated by the directive of H.E. President Mohammad Ashraf Ghani and implemented by the Capital Region Independent Development Authority (CRIDA) under its "Upgrading and Renovation of Unplanned Areas Program" to overcome some of the above-mentioned challenges (Fig. 1). The proposed route passes through homes and graveyards, requiring the acquisition of properties and relocation of gravesites having cultural and social sensitivities. While there were immense challenges in the implementation the project, CRIDA was able to effectively overcome the hurdles through their expertise, close coordination with government and non-government organizations, and effective and considerate negotiations with the affected residents. The controversial issue of relocation 4,700 graves was solved by taking (Fatwas) religiose decrees issued by the Ulema Council of Afghanistan as per the Islamic rites. After completion of determining the land ownership process and approval of the property prices by the cabinet of the Islamic Republic of Afghanistan, a total of 181 properties were acquired out of which 179 were private homes. This road, named Jamhoryat (Republic), is 2.7 km long with 20 m width, starting from the 4th Macroryan intersection passing through Qala-e-Musa and Qala-e-Khater areas and reaching to the British Cemetery in the new intersection which will be called Tawsea (Development) intersection and will be connected to the road extending to Haji Yaqoub square. Construction of this road is not only going to decrease traffic and improve security in Wazir Akbar Khan (Diplomatic enclave) and surrounding areas, but it will also improve the living conditions and access to people living along the route.

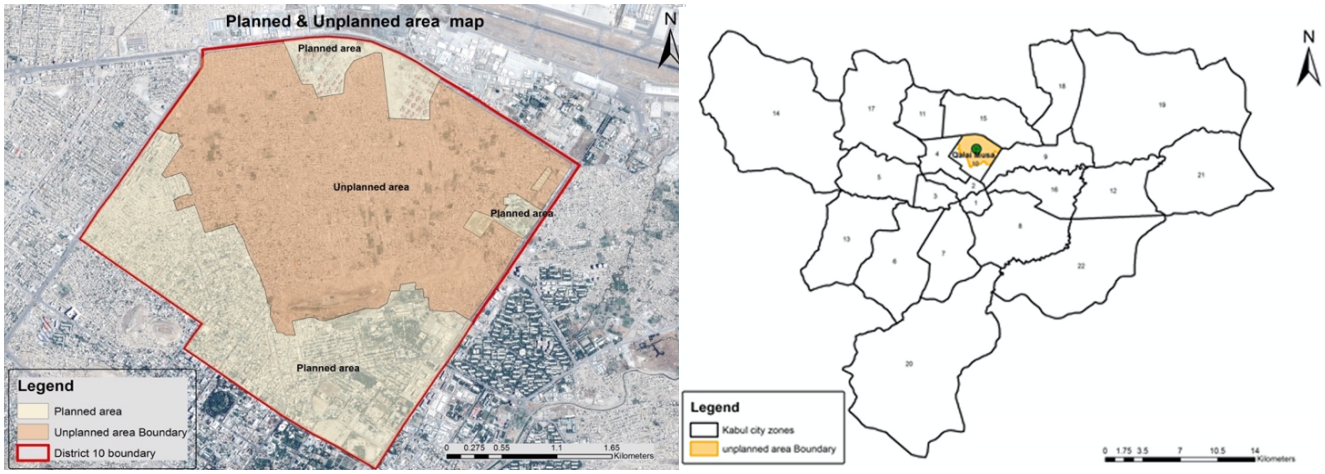

Fig. 1 (A) Map of the selected research site. (B) Location of Qala-e-Musa area in Kabul city Zones. drafted by author 2019.

2.2 *Research site*

This research is been conducted on an informal settlement in 10th district of Kabul city encompasses an area of 1289 ha. The total planned area is 539 and Qala-e-Musa encompasses 749 ha area alongside Kabul Airport road. The site is among the largest informal settlement in Kabul. It is surrounded by new, well-planned residential and commercial areas. Due to its location and physical characteristics, Existing land-use patterns not only have a significant impact on the development of the future land use plan, but they affect circulation within the area and the demand for community facilities and services as well.

As Aria Township and air force, residential blocks are located within the boundary of Qala-e-Musa, it affects its vicinity land uses concerning socio-economic and cultural aspects. Therefore, these areas have also been considered while preparing the upgrading development plan. These two townships impact will help the development process in terms of lifestyle and quality of life transformation of informal settlements. (see Fig. 2 and Table 1)

As Qala-e-Musa is an unplanned area and According to the Housing Typology, which is based on the construction material, four types of housing have seen in this area. Majority of the houses are made of Mixed-brick wooden flat roof with concrete floor and some houses are made of Mudbricks with wooden beams, recently concrete houses also have been made in this area. The houses are irregular and unstable; orientation is another problem which has not taken into consideration while constructing the houses. Some houses are made of modern and new construction materials which do not have any suitable consistency with each other and not match with the residential character of the area.

Fig. 2 Arial photo of the study area during development.

2.3 *Data collection and analysis*

The research uses a mixed-method, primary data collected using household interviews (189) (see Table 2), focus group discussions, key informant interviews, and field observations during fieldwork conducted between July and August 2018. Interviews, with households to be displaced, were carried out

Table 1 Overview of research site.

Existing Land use of Qala-e-Musa	
Land-use type	Area (Ha)
Air Force Res. Blocks	19.88
Agriculture Area	97.25
Hills	4.99
Greenery	33.27
Area Township	59.22
Cemetery	21.78
Sport Complex	0.68
Parking Lots	2.64
Masjid	1.4
Residential	326
Commercial	3.33
Educational Institute	2.5

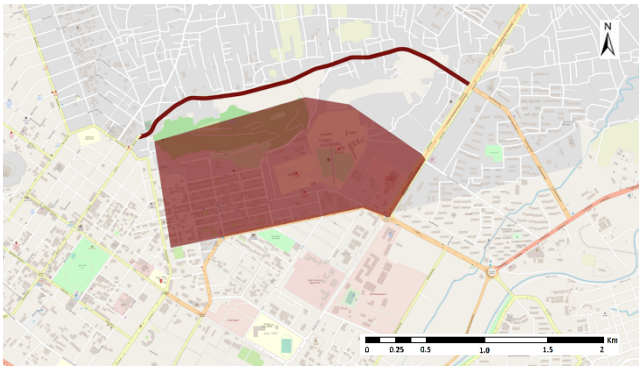

Fig. 3 Satellite image showing Qala-e-Musa redevelopment site, drafted by author (2019).

to obtain insights into their experiences with displacement. And semi-structured interview data were collected from a purposive subset of the survey population during the same period.

2.4 *Household surveys*

In August and October 2018, CRIDA research and development department division have located approximately 363 households in the study area and succeeded in surveying 189 households, consisting of 1723 individuals. Surveys were conducted with the male and/or female head of household and the questionnaire focused on topics including property and asset ownership, housing typology, household income, household composition, and demographic and socioeconomic characteristics. The questionnaire includes contact information (addresses and/or telephone numbers) for the household to obtain information on how to locate each household after displacement.

Using this contact information collected during the baseline survey as well as word of mouth, information was obtained on the post-displacement locations of approximately 189 households.

3. Recognize and measure the Impacts

This section discusses the livelihood impacts experienced by informal households during the displacement.

Table 2 gives a summary of the identified impacts of redevelopment and/or displacement on the livelihood of affected informal households. The compensation categorized into 3 cocategories (category1 is 8,000 Afghani/m^2, category 2 is 27,000 Afghani/m^2 and category 3 is 54,000 Afghani/m^2) are according to act.22 of the land acquisition law no.1321 of the Islamic Republic of Afghanistan (CRIDA, Planning and Policy, 2019).

The findings of the statistical analysis focused on the mean, variance and standard deviation, to structure the important indicators while investigating the priorities in the respondents' view.

3.1 *Loss of Social networks*

Poverty and insecurity in Afghan cities are intricately intertwined with conditions of "informality." The term and the realities it describes refers to living situations in which basic needs and activities such as work, housing, and social security are unprotected by-laws and standards.

Informal households in Kabul claimed that social networks are crucial in their everyday lives. Informal settlement dwellers depended on the networks as one of their job searching strategies. Merchants and small shop owners reported that they rely heavily on the networks with the wholesalers located in the inner-city where they get commodities and pay after selling them. Others mentioned that friends in their networks are the ones who inform them when there is a job opportunity. Also, community-based savings groups provide crucial financial support opportunities. Despite this importance, resettlement can disturb existing social networks.

We found that social network destructions, such as regular gatherings of the residents of the neighbourhood, their self-organised literacy courses, the bakery of the female households, the nearby school for their girls, all these things were seriously endangered. Fortunately, the households managed to find places not far from their old residence, enabling the family to keep up social relations.

For the households to be displaced, the anticipated impact on their social networks varies according to the relocation options. Respondents to be resettled to the adjacent municipality perceive the risk of losing customer-seller networks for home-based businesses.

3.2 *Insecurity of tenure*

The problem of the informality of land and housing is widespread but takes on different forms in the various study locations. Most questionable is the situation in Kabul, where the World Bank estimated that 69 % of its total urban area is informal and lacks municipal acceptance, thereby accommodating 80 % of the total city population. This development has been very effective in preventing homelessness in the Afghan capital, but lack of legal status and exclusion from service provision in these settlements pose

serious problems for inhabitants.

The insecurity of tenure was the immediate and highest adverse impact by informal households yet to be displaced in Qala-e-Musa. According to the survey, involuntary relocation can lead to a form of tenure insecurity. Such perceptions of insecurity were experienced by many dwellers. Two main reasons could explain their insecurity. First, for the households living in high-risk locations, will be resettled by the government and compensated with land plots in remote areas, where they would have lack of facilities and services and their socioeconomic conditions will be ruined. However, at the time of the survey, which households that would be entitled to new plots were not yet known. Most of the respondents living in high-risk zones placed themselves in a relatively weak negotiation position. For example, regarding their compensation, most the households located at high risk had fear that they don't have any right to compensation until the city authority recently decided that all the houses will at least be given land at a safe location. Second, the households who knew they would be compensated, where the land was to be acquired by the government for the development, also perceived insecurity of tenure associated with the feeling that they will not receive fair compensation, as the government categorized by housing typology, to justify the demolition. Therefore, many respondents cited insecurity concerning property value.

3.3 *Loss of income after induced development*

Informality is the basic feature of urban livelihoods in Afghanistan. This is not only in terms of land and housing but also concerning work and income opportunities. Informal employment is a lifeline for the great majority of the urban population. The problem is, as the main source of livelihoods, the informal economy is characterised by irregularity, low wages, unreliability, high competition and seasonality. Despite being the single most important source of work, its size is not sufficient to accommodate the steadily growing urban population. Although the number of households with no loos in income has the highest rate shown in table 3, while the majority of households lost their income from renting their properties and homes-based businesses as per the demolition of their houses. the study found that the number of households

Table 2 Indicators of impacts on four livelihood capitals in study area. (*=Least significant, **=Significant and ***=Very Significant)

No		Indicators	Respondents Views			Mean	Variance	SD	Sign.
1	Social	Social	Better	The same	Worse	63.0	1297	36.01	**
			102	56	31				
2	financial	Decrease & potential loss of income)	No loss	Home-based Business/Employment	Loos of income from renting	61.3	122.3	11.06	*
			73	51	60				
3	Readjustment	Destination	Did not Move	Moved to Adjacent precinct	Moved to a further precinct	62.3	5766.3	75.9	***
			150	20	17				
		Demolition	Completely Demolished	Partial Demolition (40-60) %	Minor Demolition (10-20) %	63	1083	32.9	**
			26	89	74				
		Loos of Infrastructure	Better	The same	Worse	62.3	1336.3	36.5	**
			55	102	30				
4	Entitlement	Perceived insecurity of tenure	Low	Not At all	High	62.3	1126.3	33.5	**
			30	60	97				
		Compensation	Category 1	Category 2	Category 3	61.6	7109.3	84.3	***
			159	15	30				

without occupations increased after redevelopment.

The number of workers in their most common employment types before slightly decreased after the project. These changes in income were attributed to the increased distances to new places of job opportunities, the cost of transportation to areas of job opportunities, and a lack of job and business opportunities in the new area. This lack of employment opportunities resulted in the risk of inability to use previous skills and ways for income generation. Among the lacking opportunities that meet the skills of the resettled people include informal employment, such as buying food from wholesale markets and reselling in the neighbourhoods, becoming home-based merchants and casual workers. Renting small house units for income generation and using space in their houses for home-based shops is common in many informal settlements in Kabul. Thus, according to the households, receiving only one small house as compensation will result in a loss of space for income generation. Specifically, the owners of homes for rent anticipate a loss of income from renting small houses. The loss of income and loss of space is the reason most households to be displaced on-site perceived the risk of losing their self-employment as a result of the loss of capital for investment and operational spaces. Moreover, in addition to the loss of self-employment opportunities, the households to be relocated off-site anticipate also a loss of wage employment as a result of distance.

The nature of job opportunities in the study area points to why poor urban families are struggling to survive. First, access to quality work opportunities is often determined by connections, which not many people have. Besides, the types of occupations usually available in the informal sector do not offer regular numbers of workdays, leading to lower compensation. Other jobs are also seasonal, forcing workers to frequently jump from one employment to another. High flexibility is required to make and maintain a living. Many members of the study area regularly switched between and within occupational categories and households pursued various labour mobilisation strategies in response to seasonal changes.

3.4 *Readjustment after the project*

In this section three indicator are considered including displacement, demolition and access to infrastructure. Access to basic infrastructure and services is interpreted in the context of Kabul as access to facilities, such as the city centre, schools, hospitals, markets, water, electricity, and public transportation. Our research found that most of the affected households have reasonable accessibility to infrastructure and public facilities, as shown in table 2. Majority of the household remained in the area with partial or minor demolition to their properties. In general, resettled households reported betterment in access to public facilities a decreased distance to the city centre and fair markets located in the inner-city.

The households displaced to a further municipality anticipate impacts due to the loss of good accessibility to important locations. However, the households to be resettled adjacent municipality were concerned by the potential loss of income.

4. Discussion

Understanding residents' views and perceptions are important to the adverse impacts of the development-induced displacement. The resident's perceptions, priorities and ambitions reflect their experience of everyday activities, quality of life and continuity in way of development regarding current urban challenges.

In this study, four essential sectors have been identified,

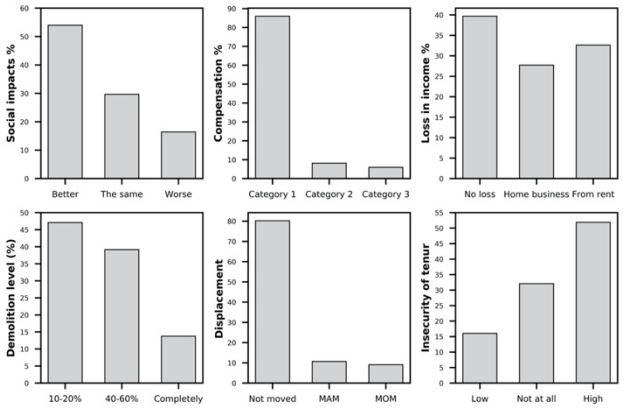

Fig. 4 Bar graphs for all analysed indicator.

looking at social and economic impacts and displacement and land tenure. These have been integrated and connected as the result of induced development produced by the project. Figure 4. Is the result of a multi-criteria assessment and weighing system through data analysis. The graphs show that there is a high potential for future redevelopment in Kabul city. The development potential based on each criterion is indicated the aforementioned table; based on improvement in social impact, compensation provided to the households and the lowest displacement index shows the effectiveness of infrastructure induced-development in the study area. To conclude this discussion, the specific successor of this project along with recommendations for future redevelopment are summarized as

follow:

4.1 ***Improvement in the traffic situation***

As a result, the project transferred the informal site into on of the largest urban redevelopment project in Kabul and has been recognized for bringing residents closer to the city centre, which has greatly reduced their commuting times and needs for a private vehicle and managed urban sprawl.

The traffic assignment conducted for this route indicates that almost 15,000 PCU will be using this route daily. On the other hand, the result indicates that the current PCU amount of Wazir Akbar khan and surrounding routes are 18,000 PCU. Result of this analysis shows that the construction of the new road will decrease congestion and traffic jams and commuting from security restricted (Green area) area of Kabul city (CRIDA 2019).

Based on the intended concept of urban accessibility in this study, the provision of good urban accessibility contributes directly to the boosting of the socio-economic activities. Simply this means more economic opportunities to the local poor households, reducing urban poverty, eliminating the social exclusion, and this is why good urban accessibility can efficiently contribute to the enhancement of the quality of urban life and to make informal areas sustainable.

4.2 ***Increased land value***

Land value is the value of a piece of property, including both the value of the land itself as well as any improvements that have been made to it (Investopedia, 2019). Within the framework of informal settlements, the most important factors to value a piece of land are the access way and the location. This is not the case in the historical and old fabric of the city where the process of land valuation is different. Therefore, parcels closer to arterial road and main streets tend to have higher value and are least desirable for redevelopment due to their relatively higher market values while parcel with no driveway have lower value and are more desirable for infill development.

4.3 ***Low-cost apartments as a solution***

To ensure a smooth relocation process and to prevent any impact, negotiations between the dwellers with the national assembly member and developers should be conducted on the matters regarding the price and the design of housing unit, temporary shelters and other compensations and claims. Households must be briefed on the relocation policy and the proposed plan, questions about their new homes

The low-cost housing should comprise of one and two-storey low-cost houses, and low-cost high-rise apartments, where the displaced households should be given the choice of selecting different types of housing.

4.4 ***Planning implication***

For the implementation of future induced development projects, some serious and untiring efforts are needed which must be according to Afghanistan's specific contexts such as economy, society and politics especially through the interventions of the governmental bodies and the private sector developers.

Initially, all those who are involved directly or indirectly with redevelopments such as the Afghan government, international donors and stakeholders should maintain a long term and highly compelling development vision with its essential drivers. In the near term, the development will be supported by it in such a way that households can take benefit of it sooner or later and also assist in the sustainable development of the area.

Furthermore, though a significant level of land transfer and housing development is taking place in Kabul, overlapping claims on land, weak systems of land administration, and inadequate enforcement of land ownership underpin low intensity and low-efficiency development. Improving the security, legally enforceability and marketability of land rights requires significant investment in land administration systems, alongside large-scale programmes of formal land registration. which can also play an important role in enabling the transformation of current land use. By registering land, low-income households are given security of tenure beneficial to themselves that can allow for further investment in durable, better quality housing.

Moreover, in many developing cities, government plans for urban spatial development have been designed without adequate consultation with communities. In the context of Afghanistan, the local council head (wakeel guzar) have local knowledge, information and community networks that can be mobilized to make civic engagement meaningful and effective, and they know community issues and assets. their advice and input is representative of a wide range of citizens in their community and can encourage the households to participate.

Finally, based on the bar-graph, the corresponding ρ -

Table 3 Estimation of correlation coefficient ρ of induced development components.

Indicators	Social	Loss of infrastructure	Financial (compensation)	Financial (Income)	House demolition level	Physical (Destination)	The insecurity of land tenure before resettlement
Social impacts	1						
Loss of infrastructure	0.17 ns	1					
Compensation	0.94 ***	-0.15 ns	1				
Financial (Income)	0.71 ***	-0.55 **	0.67 **	1			
House demolition level	0.60 **	0.89 **	0.55 **	0.82 ***	1		
Physical (Destination)	0.94 ***	-0.15 ns	0.99 ***	0.69 ***	0.62 **	1	
Insecurity of land tenure	-0.97 ***	-0.39 *	-0.02 ns	0.72 **	0.42 *	0.11 ns	1

values of each indicator estimated in table 6 indicate that the relationship of most indicators was found to be significant.

The specific elements assessed in the study have been summarized as in Table 3.

The correlation coefficient ρ is used to characterize the linear relationship between two continuous variables. Estimates of the correlation (r) that are close to 0 indicate little association between the two variables, whereas values close to 1 or -1 indicate a strong association. The sign of the correlation estimate, either positive or negative, reflects the direction of the relationship. This type of data has a variation between the subjects as well as variation within the repeated measurements on each subject which is accounted for.

5. Conclusion

The current rapid growth of cities in Afghanistan is characterised by different ambitions that are increasing the number of urban populations displaced from provinces and returning refugees from neighbouring countries, especially informal settlement dwellers.

The socioeconomic-based evaluation has been applied to a variety of indicators and their characteristics and interactions, whose dynamics depend on the development type and how local communities take advantage of the proposed development. These also depend on the different characteristics of the built environment, related use functions and features of the communities. Finally, as the involved indicators are interconnected, a systemic perspective should be applied to make the development process more efficient.

Furthermore, clear and transparent guidelines on compensation and entitlements for each displacement type need to be disclosed in the early stage and discussed with affected households. Based on this information, affected households can then engage appropriately with related stakeholders for inclusive project implementation.

Also, our research shows that resettled informal settlement dwellers experienced several impacts on their livelihood, including social disarticulation, potential loss of income, insecurity of tenure, and other basic amenities, of which the intensity is varied depending on the property. Most of these risks are more severe in the case of moving to a further precinct than moving to the adjacent precinct. They mainly derive from exclusion in decision-making processes and the consequent lack of consideration of needs and the interests of resettled households. This should be adequately addressed in unplanned settlement relocation laws and policies.

The households to be resettled should be key actors in resettlement planning and decision-making on crucial issues, such as housing design, resettlement site selection, and livelihood security. Although we acknowledge that some resettled informal dwellers who were living in poor and unsafe housing conditions before their relocation might benefit from an improved shelter in safer locations, this study confirms that the current exclusionary practices are more likely to lead to the impoverishment of affected informal households than to improvements in their livelihoods.

By identifying displacement impacts, this study provides a general picture of the potential impacts of urban displacement and resettlement processes on informal settlement dwellers. We argue that both the pre-and post-displacement impacts should be considered in the practice of the livelihoods affected informal households, are to be effectively protected and improved through induced development.

Although impacts might differ by induced development

site, our empirical findings offer important insights into the impacts of redevelopment projects on informal households. We acknowledge that some of the impacts perceived by the households to be relocated, for example, housing-related risks and loss of access to jobs, might be influenced not only by the planning practices, but also by their needs, interests, acceptance, or resistance toward the relocation. Therefore, we encourage conducting more in-depth research into the planning and decision-making processes by all stakeholders, for example, on how government and different actors and their interaction fit into the bigger picture of the processes.

Acknowledgement

This research is mainly informed by the findings of the socio-economic survey undertaken in August to October 2018 in Kabul. The authors gratefully acknowledge the assistance provided by Planning and Policy division and specifically Mr Faridullah Nasiri, senior manager at Capital Region Independent Development Authority (CRIDA) in Kabul, Afghanistan for all their effort in facilitating survey and providing the required data for this research. and the research support from Dr Eng. Yoshitaka KAJITA for his constructive comments of on the first draft of this work.

Conflict of Interests

The author declares no conflicts of interest regarding the publication of this paper.

References

1) Jo Beall and Stefan Schutte, Urban Livelihoods in Afghanistan, Synthesis paper series, Afghanistan Research and Evaluation Unit, pp.1-5 (2006).
2) Guidance notes on national sustainable development strategies in post-conflict countries; UN, Division for sustainable development. (2011).
3) HEATHER RANDELL, The short-term impacts of development-induced displacement, World Dev. Vol.87, pp.385–400 (2016).DOI:10.1016/j.worlddev.2016.07.005.
4) Frank Vanclay, Project-induced displacement and resettlement: from impoverishment risks to an opportunity for development?, Impact Assessment and Project Appraisal, Vol.35, No.1, pp.3-21 (2017). DOI: 10.1080/14615517.2017.1278671
5) Ilija Gubic * and Oana Baloi, Implementing the New Urban Agenda in Rwanda: Nation-Wide Public Space Initiatives, Urban Planning (ISSN: 2183–7635), Vol.4, No.2, pp.223-236 (2019).
6) Cernea, M, The risks and reconstruction model for resettling displaced populations. World Development, Vol.25, No.10, pp.1569–1587 (1997). https://doi.org/10.1016/S0305-750X (97)00054-5.
7) Alice Nikuze∗, Richard Sliuzas, Johannes Flacke, Martin van Maarseveen, Livelihood impacts of displacement and resettlement on informal T households - A case study from Kigali, Rwanda, Habitat International Vol.86, pp.38–47, (2019). https://doi.org/10.1016/j.habitatint.2019.02.006
8) Chengri Ding, Gerrit J. Knaap, Lewis D. Hopkins, Managing Urban Growth with Urban Growth Boundaries: A Theoretical Analysis, Journal of Urban Economics, Vol.46, No.1, pp.53-68 (1999).
9) Liz Alden Wily, Land Rights in Crisis; Restoring Tenure Security in Afghanistan, Issues Paper Series, Afghanistan Research and Evaluation Unit, pp.19-25 (2006).
10) Larsson, G, Land readjustment: A tool for urban development, Habitat International, Vol.21, No.2, pp.141-152 (1997).
11) Choi, N, Impacts of displacement on urban livelihoods: a railway project in Metro Manila, Development in Practice, Vol.25, No.5, pp.643-654 (2015). https://doi.org/10.1080/09614524. 2015.1051948.
12) Robina Manandhar, Land Readjustment for Regularization of Informal Settlements, JSCE Vol.6, pp.40-50 (2019).
13) Peter Gaimpaoli, Land Tenure and property tights in Afghanistan, 2010, accessed online on March 12, 2020, at https://www.land-links.org/issue-brief/land-tenure-and-property-rights-in-afghanistan/
14) Stefan Schütte, Informal insecurity in urban Afghanistan, Iranian studies, Vol.42, No.3, pp.465-491 (2009).
15) Van der Geer J, Hanraads JAJ, Lupton RA. The art of writing a scientific article. J Sci Commun Vol.163, 51-9. (2000).
16) United Nations, Department of Economic and Social Affairs, Population Division. World Urbanization Prospects: The 2014 Revision, Highlights (ST/ESA/SER.A/352) (2014).
17) Strunk Jr W, White EB, The elements of style. 3rd ed. New York: Macmillan (1979).
18) Mettam GR, Adams LB, How to prepare an electronic version of your article. In: Jones BS, Smith RZ, editors. Introduction to the electronic age. New York: E-Publishing Inc, pp.281-304 (1999).
19) Litman, T., Social inclusion as a transport planning issue. Victoria, Canada: Victoria Transport Policy Institute

(2003).
20) Faziawati Abdul Aziz, Suzanne Speak, and Tim Townshend, Social Implication of Squatter Relocation: The Case of Desa Mentari, Urban and Transit Planning. Advances in Science, Technology & Innovation (IEREK Interdisciplinary Series for Sustainable Development). Springer (2020).
21) UN-HABITAT (n.d.) Operational policy framework to address the shelter needs of urban poor particularly those living in informal settlements volume I of III.
22) The World Bank, Kabul Urban Policy Notes Series n.2, Washington, DC: World Bank (2006).
23) Amiri B.A. and Lukumwena N. Suitability Analysis for Infill (Re)development Within Informal Context of the City: A Case Study of Hothkhel, Kabul City. Urban and Transit Planning. Advances in Science, Technology & Innovation (IEREK Interdisciplinary Series forSustainable Development). Springer (2020).
24) Paul Collier, Priya Manwaring, Michael Blake., Policy options for Kabul's informal settlements, International growth centre. (2018).
25) The author used and cited clause from Afghanistan National laws related to the study listed as follow: 1st Housing and Urban Development (2017) Ministry of Urban Development and Housing, 2nd Afghanistan Informal Settlement Law (2017) Ministry of Justice, 3rd Afghanistan Land Management Law (2017) Ministry of Justice and Afghanistan National Housing Policy (2018).

Proc. Schl. Eng. Tokai Univ., Ser. E
45 (2020) 37-43
DOI: 10.18995/24343641.45.37

Impact Absorption Characteristics of a CFRP Member for the Front Part of an Automobile in the Axial Compressive Direction: Experimental Consideration on Protection for Structural Parts

by

Kento NIISHIYAMA[*1], Kohei NARIKAWA[*1], Hideaki KATO[*2] and Takayoshi NARITA[*3]

(Received on May. 11, 2020 and accepted on Jul. 24, 2020)

Abstract

The energy-absorption ability of the front part of vehicles should be improved to absorb more energy with less deformation of structural parts. This study investigated the use of carbon fiber reinforced plastic (CFRP) for only the crash box (CB) to absorb impact energy, with steel used for the front side member (FSM) of structural members. We focused on CFRP, which is a high-performance material for energy absorption, and experimentally examined the structure of a CB that can effectively be crushed and absorb energy while maintaining the original shape of the FSM. A test piece was fabricated by joining a cylindrical CFRP member as the CB with varying number of layers and a cylindrical steel member assumed as the FSM. A drop weight test was performed and the crushing characteristics of the CFRP and steel member were investigated. The results showed, that our proposed CFRP pipe, in which the number of laminations of the CFRP prepreg decreases the structural strength of the CB facing the impactor, reduce the peak load in the initial stage of crushing and maintained the shape of structural parts.

***Keywords*:** Carbon fiber reinforced plastic, Crash box, Impact absorption, Front side member

1. Introduction

The collision safety standards for automobiles are becoming stricter year by year to increase the survival rate of pedestrians and cyclists in traffic accident. On the other hand, from the viewpoint of additional value for the customer, automobiles are required more large volume as possible in the cabin. In conventional vehicles, a crash box (CB) for absorbing the impact energy is mounted at the tip of the front side member (FSM), which is the main frame of the vehicle. The front part of the vehicle should improve its energy-absorption ability to absorb greater energy with less deformation. Furthermore, it is required that the front part of vehicle be compact to increase the volume of the cabin. In generally, metals such as steel and aluminum are often used as energy absorbing members, but carbon fiber reinforced plastic (CFRP) has been focused as a new material for reducing the weight of vehicle bodies.

*1 Undergraduate Student, Department of Prime Mover Engineering
*2 Junior Associate Professor, Department of Prime Mover Engineering
*3 Assistant Professor, Department of Prime Mover Engineering

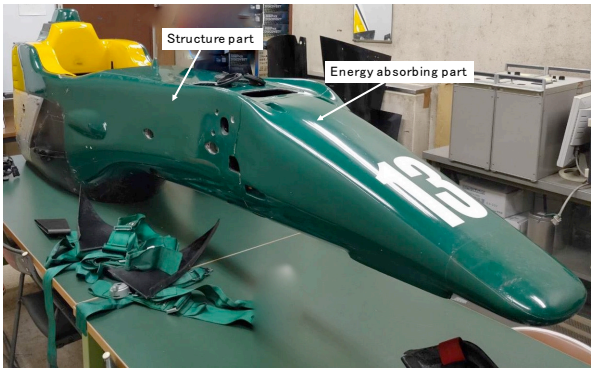

Fig. 1 Racing car manufactured by CFRP.

It has been reported that CFRP which is easy to be formed any shape of member exhibits high energy absorption performance[1, 2]. In racing cars, many parts, such as CB and structural members including FSM, are manufactured by CFRP as shown in Fig. 1[3-5]. However, in general passenger cars, the use of CFRP components is limited from the viewpoint of cost and productivity. Therefore, this study investigated in the case that CFRP is used for only CB to absorbing impact energy and steel is used for FSM of structure member.

CFRP can be installed in a small space in front of the car, since it has high formability and performance of energy absorption. Therefore, it is expected to absorb the collision energy with a small amount of crushing. We fabricated cylindrical CFRP specimens with a partially changed number of plys and evaluated the energy absorption performance of the specimens by a drop weight test. From the experimental results, it has been confirmed that the energy absorption performance of the test piece can be controlled by changing the number of plys[6].

On the other hand, if the structural strength of the CB is higher than the FSM, the FSM may buckle firster than CB in collision. It would make damage the passenger's lower limbs[7]. In order to prevent the FSM from buckling first, it is necessary to increase the structural strength of both the FSM and the CB, and to design the strength so that it crushesd from the CB. Some researchers have reported that the energy absorption characteristics of members such as CBs and bumpers to protect passengers and pedestrians previously[8,9]. However, it has not reported that energy absorbing performance of the member which consist of the CB needed to crush for energy absorb and FSM needed to maintain the structure without crush.

Therefore, this study focuses on CFRP, which is a high-performance material of energy absorb, and experimentally examines the structure of CB that can effectively crush and absorb energy while maintaining the original shape of FSM. A test piece was fabricated by joining a cylindrical CFRP member assumed as CB with a partially different number of layers and a cylindrical steel member assumed as FSM. Furthremore, a drop weight test was performed and investigated the crushing characteristics of the CFRP and steel member.

2. Energy absorbing performance of test piece connected with CFRP and steel member

2.1 *Outline of drop weight test*

To evaluate the energy absorbing performance of test pieces, drop weight test was carried out. A drop weight tester was shown in Fig. 1. The drop weight as impactor is lifted by the winch, and the drop weight falls at the start of the test, crushing the test piece placed under the drop weight. The test piece was placed on a steel plate processed with spot facing, as illustrated in Fig. 2, and fixed by filling it with molten metal U-alloy. A laser displacement sensor for measuring the displacement of the impactor and a load cell for measuring the load were installed under the test piece, and the measurement was performed at a sampling frequency of 500 kHz. In this section, the mass of the impactor was 17.9 kg and the height was 2.5 m. The test piece was manufactured by connecting a CFRP pipe assumed CB and a steel can assumed FSM. The CFRP pipe with a height of 100 mm, an inner diameter of 50 mm was manufactured by 3 plied prepreg of plain weave which bundled of 3000 fibers. The CFRP pipe and the steel can were connected with adhesive of the metal lock manufactured by CEMEDINE co. ltd. The height of the steel can was 104 mm, the inner diameter was 52 mm, and the thickness was 0.2 mm. To compare the connected test piece of CFRP and steel member, we fabricated 2 test pieces that is the test piece connected 2 steel cans (hereafter Steel + Steel) and the steel can and the CFRP pipe (hereafter CFRP 3Ply + Steel) as shown in Fig. 4. Figure 5 shows the equipment used for video recording.

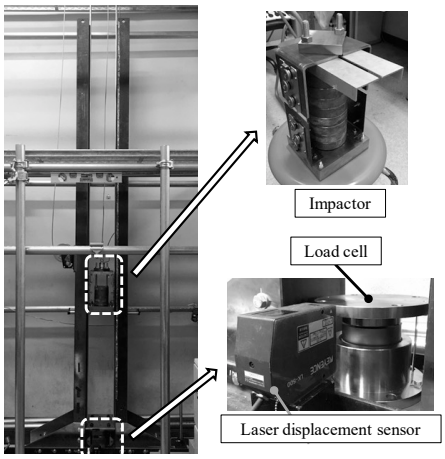

Fig. 2 Photograph of drop weight tester.

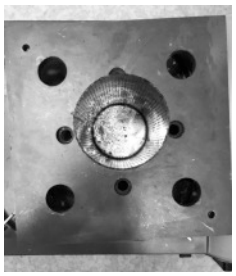

Fig. 3 Test piece fixed with fusible alloy.

(a) Steel + Steel (b) CFRP 3Ply + Steel

Fig. 4 Connected test piece.

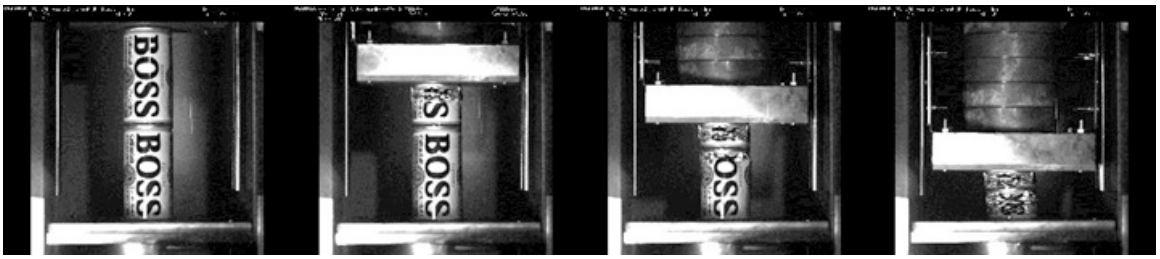

(a) Steel + Steel test piece

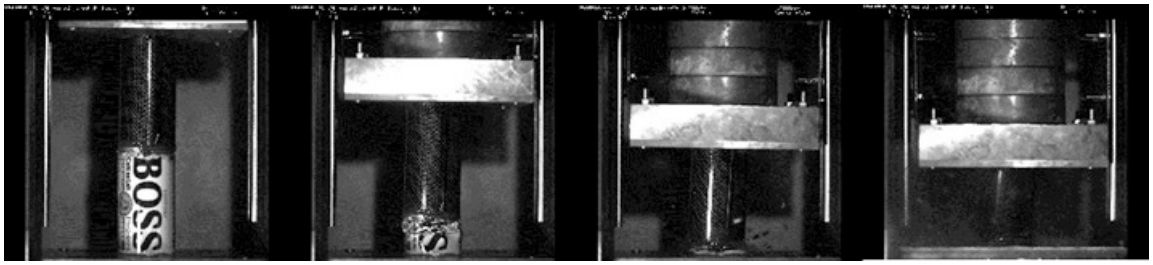

(b) CFRP 3Ply + Steel test piece

Fig. 7 Connected test piece was being crushed by impactor taken with the high-speed camera.

Fig. 5 High speed camera.

(a) Steel + Steel (b) CFRP 3Ply + Steel

Fig. 6 Comparison of the test piece crushed in the drop weight test and the test pieces before the test.

2.2 *Experimental result of drop weight test*

Figure 6 shows the comparison of the test piece crushed in the drop weight test and the test pieces before the test. Although the Steel + Steel test piece was completely crushed, the CFRP 3Ply + Steel test piece was completely crushed at steel can part and remained its structure at CFRP part. Figure 7 shows how the test piece was being crushed by impactor taken with a high-speed camera. Figure 7 (a) shows that the steel can part which face to impactor was crushed at first in Steel + Steel test piece. On the other hand, the CFRP 3Ply + Steel test piece was crushed at the steel can part which did not face to impactor, as shown in Fig. 7 (b). Moreover, the crushing at CFRP part occurred at the side not to face to the impactor. In order to quantitatively evaluate the progress of crushing, the ratio of the amount of crushing δ to the length L of the entire test piece was defined as δ / L. Figure 8 shows comparison of these test pieces at approximetly $\delta / L = 0.4$. In each test piece, it is confirmed that buckling occurred in the steel can part. From these results, it is considered that the

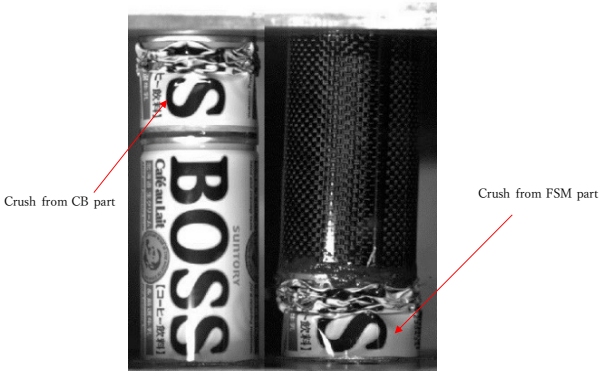

Fig. 8 Detail buckling of each test piece.

structural strength of CFRP part assumed as CB is extremely greater than steel can part assumed as FSM.

Figure 9 shows the load-displacement diagrams of the drop weight test in each test piece plotted by displacement measured by the laser sensor and load detected by the load

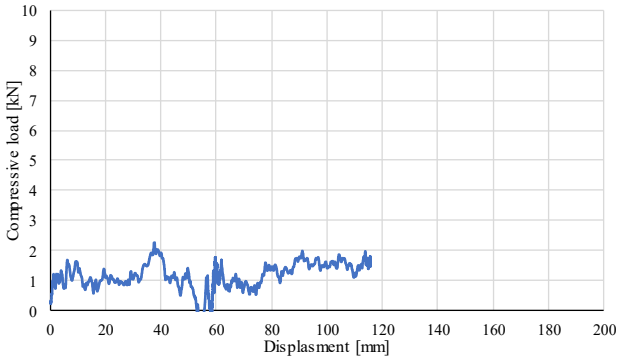

(a) Steel + Steel test piece

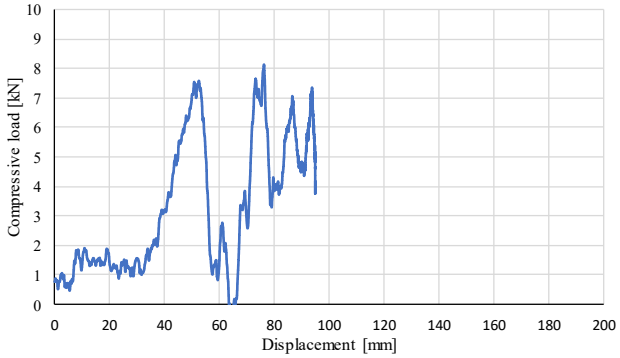

(b) CFRP 3Ply + Steel test piece

Fig. 9 Load-displacement diagrams in drop weight test.

cell. In this study, the point at which the load detected by the load cell started to increase after the impactor falling was defined as the contact between the impactor and test piece, and crushing began; the displacement at this time was defined as 0 mm. At first, the tendency of both test piece was same when the steel can part was crushed. Then, at the crush amount δ = 37 mm, the load of CFRP 3Ply + Steel test piece increased drastically when the crushing occurred at the CFRP part. Finally, the total crushing amount was 116 mm at Steel + Steel test piece and 95 mm at CFRP 3Ply + Steel test piece.

Assuming that the impact load at a minute crushing amount ds [mm] of the test piece is $f(s)$ [kN], the absorption energy U when the impactor is displaced by x [mm] can be expressed by the following equation[6]:

$$U = \int_0^x f(s)\,ds \,. \tag{1}$$

By using eq. (1), the absorption energy at the crushing rate δ / L = 0.1, 0.3, 0.5 and crushing completed were summarize to Table 1. From these experimental results, Steel + Steel test piece could not completely absorb the energy of the impactor. Although CFRP 3Ply + Steel test piece was able to completely absorb energy, the steel can which assumed as FSM was completely crushed. Therefore, it is necessary to study the structural strength of CB that can absorb energy while maintaining the structure of FSM.

Table 1 Absorption energy of each test piece.

	Steel+Steel [J]	CFRP3 Ply+Steel [J]
δ/L = 0.1	7.8	16.2
δ/L = 0.3	50.6	68.8
δ/L = 0.5	60.2	158.6
Crushing completed	134.6	305.2

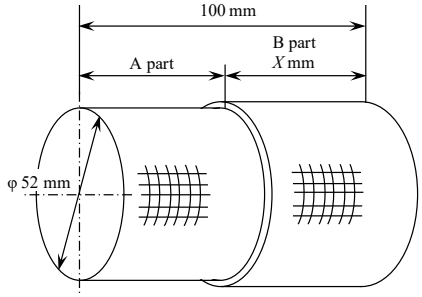

Fig. 10 Schematic diagram of CFRP test piece with different ply numbers.

3. Consideration to maintain the FSM structure by using CFRP test piece which the number of plies partly changed

3.1 *CFRP test piece which the number of plies partly changed*

Experimental results in previous section shows that it is important to control the strength of the CFRP part to maintain the structure of the FSM. In our previous study, we have confirmed that partial change of the ply number of prepreg in cylindrical CFRP test piece can control the energy absorption performance[6]. In this section, it is investigated that the CFRP test piece partly changed the ply number was applied in CB to maintain the structure of the FSM made of the steel can. Moreover, we aim to clarify the condition so that the CB is firstly crushed.

The CFRP pipe was manufactured by laminating CFRP prepreg of CF / PPG / 3KP / 33G manufactured by CAST co. ltd. and forming to the cylindrical test piece. Figure 10 shows a schematic diagram of the manufactured test piece with a total height of 100 mm, an inner diameter of 52 mm. Part A is the side that contacts the impactor, and part B is the side that is fixed to the steel can assumed as FSM. To decrease the structural strength comparing to the test piece in previous section, the number of plies was 1 ply in part A and 2 plies in part B. To change the structural strength of the CFRP part, 3 CFRP pipes with the height of part B X = 50 mm, 75 mm, and 100 mm were manufactured.

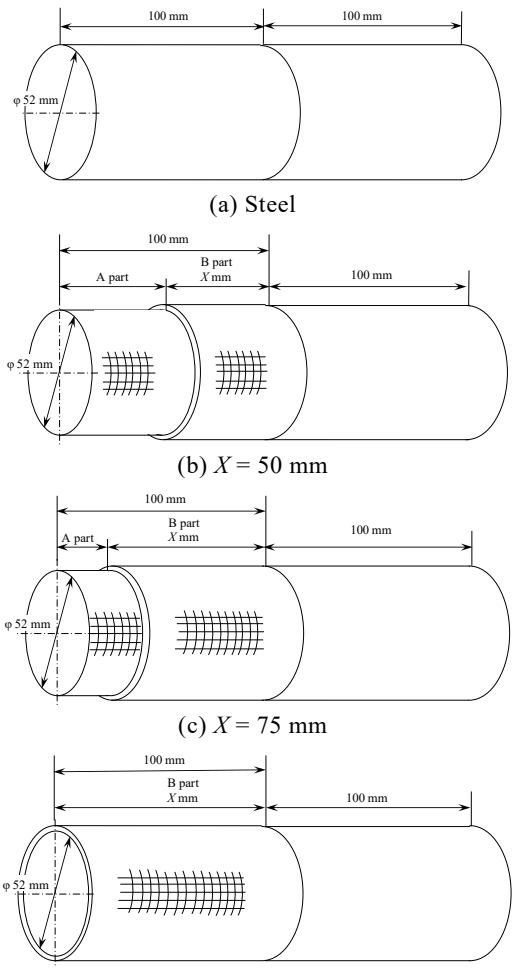

Fig. 11 Schematic diagrams of constructed test piece.

3.2 *Experimental condition of drop weight test*

The drop weight test was performed to investigate crush characteristics of the test piece connected the steel can assumed FSM to the manufactured CFRP pipe assumed CB as the same to previous section. In this section, the mass of the impactor was 17.9 kg and the height of the impactor was 1.5 m. We constructed 4 types of test piece which changes CB part connected to the FSM of the steel can as follows; (a) steel can (hereafter Steel, which is same to Steel + Steel test piece in previous section), (B) CFRP pipe with X = 50mm, (c) X =75mm, and (d) X = 100 mm. Figure 11 shows schematic diagrams of these test pieces.

3.3 *Experimental result of drop weight test*

Figures 12 shows photographs of the crushed test pieces. The measured crush amount of FSM part, which is red line shown in Fig. 12, is shown in Fig. 13. Although the FSM part could almost be remained in test pieces of (a) Steel and (c) X = 75 mm, the FSM part was completely crushed before crushing CB part in the test piece of (d) X = 100 mm. Figure 14 shows the load-displacement diagrams in each test piece. In two types of test pieces shown in Figs. 14 (b) and (c), the

(a) Steel (b) X = 50 mm (c) X = 75 mm (d) X = 100 mm

Fig. 12 Photograph of the crushed test pieces.

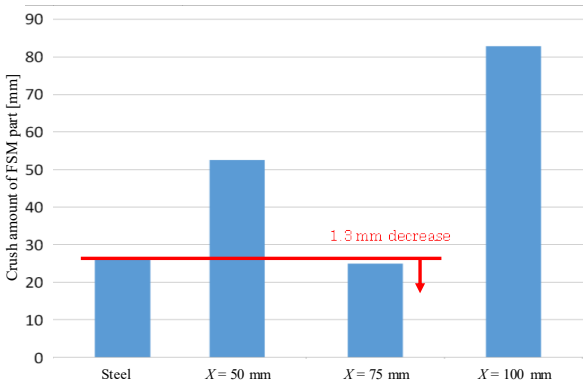

Fig. 13 Measured crush amount of FSM part.

measured load was less than the Steel test piece in the initial stage of crushing. Then, the load increased after the crushing of part A was completed, and the amount of the load was almost the same as the result of the (a) Steel test piece. On the other hand, in the result of (d) X = 100 mm as shown in Fig. 14 (d), a large load was measured after the impactor immediately contacted to the CB part.

The amount of energy absorbed by the CB part is clarified, and the relationship between the amount of energy absorbed by the CB and the fracture size of the FMS part is quantitatively explained. For the purpose of this study, we compare (a) CFRP [X = 50 mm] and (c) CFRP [X = 75 mm] for steel materials, and link the knowledge obtained from this comparison with the establishment of design guidelines for high-efficiency CB that can effectively crush and absorb energy while maintaining the original shape of FSM. Figure 15 shows the maximum load peak in Fig. 14 of each test piece in the initial stage of crushing which we defined in the range of δ / L = 0 ~ 0.25. The CB with X = 50 mm had the lowest load peak at the initial stage of crushing. However, the CB with X = 50 mm crushed completely and the FSM also crushed. As the height of 2 Ply part X increases, the initial load peak also increases. The initial peak at X = 75 mm was almost equal to Steel test piece, and the result at X = 100 mm was larger than the result of the Steel. However, the absorption energy as shown in Fig. 16 was minimum at X =

100 mm. It was shown that the CB with X = 100 mm could not absorb the impact energy.

From these results, it is considered as follows. In the case of X = 50 mm and 75 mm, the load increased smoothly by intentionally reducing the structural strength of the CB facing the impactor. It is considered that the load in the initial stage of crushing was lower than the structural strength of the FSM, thereby preventing the buckling of the FSM. It is probable that the impact energy could not be completely absorbed by CB alone because CB with X = 50 mm had too weak a structural strength. In the case of X = 100 mm, the load in the initial stage of crushing increaseddrastically, and the maximum load was greater than the structural strength of the FSM. Therefore, the buckling of the FSM could not prevent.

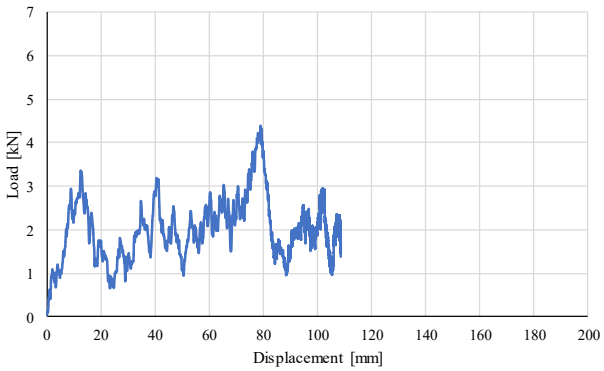

(a) Steel

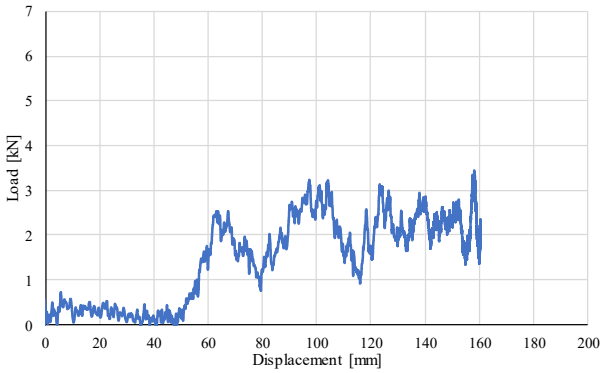

(b) X = 50 mm

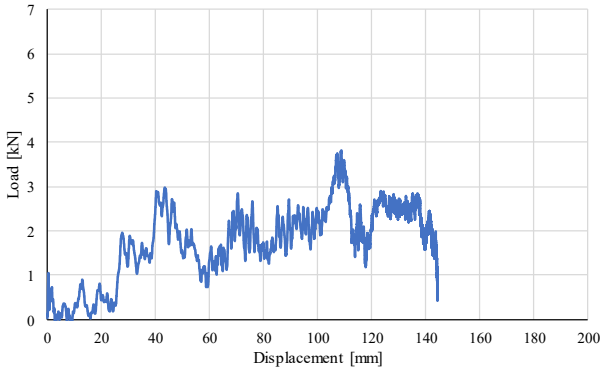

(c) X = 75 mm

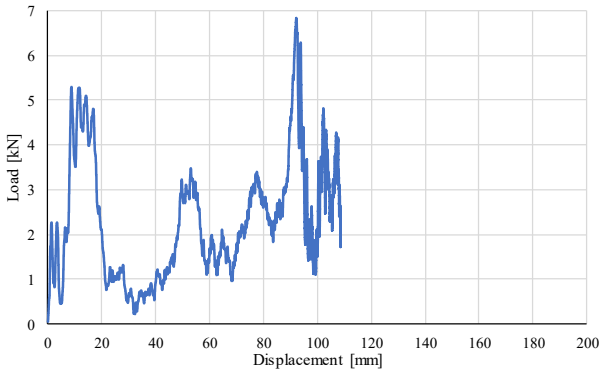

(d) X = 100 mm

Fig. 14 Load-displacement diagrams in each test piece.

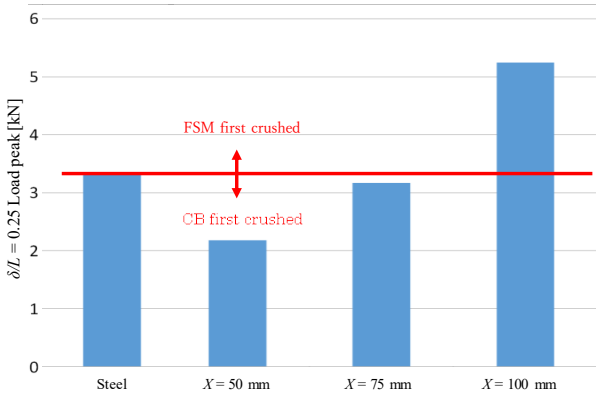

Fig. 15 Maximum load peak in the initial stage of crushing (δ / L = 0 ~ 0.25).

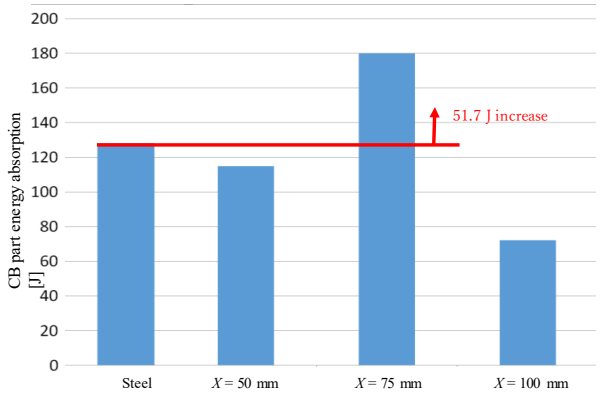

Fig. 16 Absorption energy in the initial stage of crushing (δ / L = 0 ~ 0.25).

4. Conclusion

In order to establish a design guideline for a highly efficient CB that can effectively crush and absorb energy while maintaining the original shape of FSM, the crushing characteristics of the test piece, which consist of the CFRP pipe assumed as CB and the steel can assumed as FSM, was investigated by the drop weight test. From experimental results, the CB which has excessive structural strength could not absorb the impact energy and maintain the structure of

the FSM part. In especially, it was found that the FSM tend to crush firstly due to the large load peak occurred in the initial stage of crushing in the case of the excess structural strength of the CB. Therefore, the our proposed CFRP pipe which the laminate number of CFRP prepreg was partly changed was applied to CB connected with the FSM. The proposed CFRP member intendedly decrease the structural strength of the CB facing to impactor, and the load peak in the initial stage of crushing was able to be reduced. This reduction of the initial stage peak allowed the FSM structure to be maintained. From this result, in order to design a CB that can maintain the structure of FSM, it is necessary to have sufficient strength to absorb impact energy and reduce the initial stage peak of load. In the future, we would investigate the energy absorbing characteristics of the CFRP member in more detail when the number of plies, laminate direction and shape of the member is changed.

References

1) T. Futatsuka, T. Fujita, Y. Yamasaki and T. Urabe: Development of Collision Energy Absorption Parts Energy-Derivative Method, Journal of Society of Automotive Engineers of Japan, Vol.46, No.4, pp. 799-804 (2015).
2) T. Matsuo, M. Mitsuharu, K. Furukawa, T. Sumiyama, H. Enomoto, K. Sakaguchi, Investigation about Axial Collapse Crashworthiness of Thermoplastic CFRP Crash Boxes by Out-of-plane Damage Finite Element Modeling Energy-Derivative Method., Journal of Society of Automotive Engineers of Japan, Vol.48, No.2, pp.549-554 (2017).
3) G. Savage, I. Bomphray and M. Oxley: Exploiting the fracture properties of carbon fibre composites to design lightweight energy absorbing structures, Engineering Failure Analysis, Vol.11, pp.677–694 (2004).
4) P. Feraboli, C. Norris and D. McLarty, Design and certification of a composite thin-walled structure for energy absorption, International Journal of Vehicle Design, Vol.44, No.3/4, pp.247–267 (2007).
5) J. Obradovic, S. Boria and G. Belingardi, Lightweight design and crash analysis of composite frontal impact energy absorbing structures, Composite Structures, Vol. 94, pp.423–430 (2012).
6) T. Tanaka, S. Nakata, S. Sugisaki, H. Kato and T. Narita: A Basic Study of the Impact Absorption Performance of a CFRP Cylindrical Shell Member with Changes in Ply Number in Half of the Member, Proceedings of the School Engineering Tokai University, Vol.44, pp.27-33 (2019).
7) M. Sakurai, Accident Reconstruction to Analyze Impact of Injured Drivers in Collision -Ankle Fracture in Car-to-Car Offset Frontal Collision Journal of Society of Automotive Engineers of Japan, Vol.28, No.4, pp.117-122 (1997).
8) K. Nagasaka, K. Mizuno D. Ito and N. Saida: Calculation Method to Determine the Structural Component's Contribution on the Deceleration of a Passenger Compartment in Vehicle Crashes Based on the Energy-Derivative MethodJournal of Society of Automotive Engineers of Japan, Vol.48, No.4, pp.879-884 (2017).
9) T. Yabu, S. Yasuhara and M. Kashiwagi, Research of Design Method of Crash Box Made by Thermoplastic GFRP Energy-Derivative MethodJournal of Society of Automotive Engineers of Japan, Vol.48, No.4, pp.945-951 (2017).

Proc. Schl. Eng. Tokai Univ., Ser. E
45 (2020) 45-50
DOI: 10.18995/24343641.45.45

A Cylindrical Linear Induction Motor for Vertical Transfer: A Fundamental Consideration on Thrust Characteristics

by

Sora ISHIHARA*1, Ryo NAKASUGA*2, Yasuhiro NARAWA*1,
Ryo YAMAGUCHI*1, Takayoshi NARITA*3 and Hideaki KATO*4

(Received on May 11, 2020 and accepted on Jul. 24, 2020)

Abstract

In a conventional elevator, the vibration and twisting of the cable become a serious problem when the cable is very long. Therefore, an elevator using a method that omits the counterweight and is moved by an actuator on a single cable with both ends fixed was considered. However, contact between the actuator and the cable decreases the efficiency and damages the cable owing to the inclusion of foreign matter. Therefore, this paper proposes a vertical transportation system which moves above a long and uniform conductor cable without contact by using a cylindrical linear induction motor (LIM) as the actuator. A cylindrical LIM above the reaction plate, which is a cylindrical shell-shaped conductor, has an advantage that the magnetic force acts on the reaction plate uniformly. This is expected to suppress the vibration in the gap direction. However, a conventional LIM drives the mover in the horizontal direction, and system design guidelines for a device that can directly exert thrust in the vertical direction have yet to be established. Therefore, we constructed a model for analyzing the cylindrical LIM and performed electromagnetic field analyses by the finite element method. The thickness of the reaction plate was varied in the analyses and the effect on the generated thrust was investigated. From the analysis results, the optimum thickness of the cable was determined by obtaining the range of the magnetic flux density acting on the cable.

***Keywords*:** Cylindrical linear induction motor, Electromagnetic field analysis, Actuator, Elevation

1. Introduction

In recent years, many large structures such as high-rise buildings have been constructed. In such a large building, a device such as an elevator is used when carrying a person or a luggage. In general, in a conventional elevator, a cargo area carrying a person or luggage, and a counterweight having substantially the same weight as that of the cargo, are connected by a wire, and the cargo operated by a cable moves up and down[1]. However, if building heights increase in the future, the cable will become extremely long, and thus the vibrations and twisting of the cable will become a serious problem[2, 3]. Therefore, some researchers have proposed an elevator using a method that omits the counterweight and moves by an actuator on a single cable with both ends fixed, as shown in Fig. 1. The general actuator for such the elevator

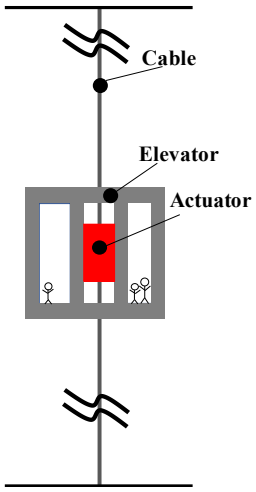

Fig. 1 Schematic diagram of an elevator that omits the counterweight and moves on a single cable.

*1 Graduate Student, Course of Mechanical Engineering
*2 Undergraduate Student, Department of Prime Mover Engineering
*3 Assistant Professor, Department of Prime Mover Engineering
*4 Junior Associate Professor, Department of Prime Mover Engineering

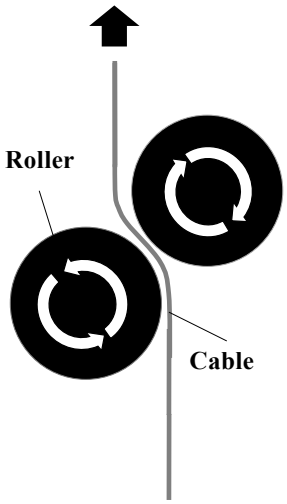

Fig. 2 Conventional method to generate a frictional force for elevation.

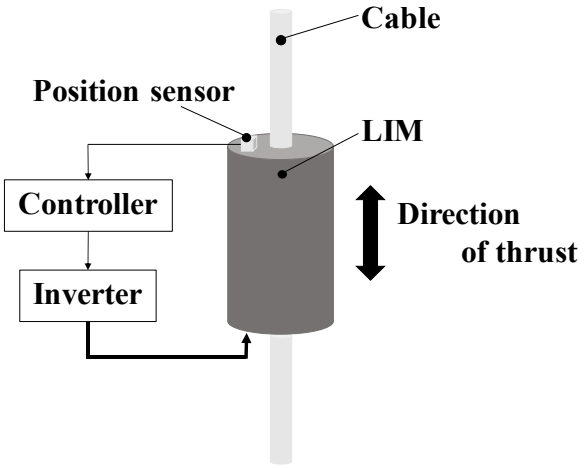

Fig. 3 Schematic illustration of proposed actuator.

has rollers or tires that are driven by an electrical motor and generates a frictional force by contact between the cable and the pully or tire, as shown in Fig. 2[4-6]. However, the elevation device requires a frictional force that exceeds the weight of the lifted object. To generate a highly frictional force, some method is considered. One is an increase in the friction coefficient by some surface treatment to the cable or pully. The other is an increase in the force in the contact surface direction. Conversely, these methods decrease the efficiency and damages the cable owing to the inclusion of foreign matter. The maintenance of the devices and a reduction of the number of replacements are considered to be major issues in the vertical transportation system on the extremely long cable.

To extend the life of such a device, a device that can move vertically without mechanical contact is required. To realize the device, some researchers proposed to use a linear synchronous motor or a linear switched reluctance motor[7]. Although these linear motors need installation of permanent magnets or uneven surface processing on the extremely long cable, these methods lead to increase the weight and decrease the strength of the cable. A uniform shaped object is superior to the installed cable or the processed cable from the viewpoint of weight and strength. Therefore, a linear induction motor (LIM) that moves above the uniform shaped conductive reaction plate without contact is expected in the vertical transportation system in extremely long cable[8,9]. A general LIM which is installed above a plane-shaped reaction plate generates a driven force and a perpendicular force to the driving direction. The perpendicular force presses the LIM itself against the reaction plate and changes the gap between the surface of the LIM and the reaction plate. This change causes the vibration of LIM and contacts to the reaction plate. Additionally, it is difficult for the LIM of plane type to maintain the gap between the LIM and the reaction plate against the vibrations caused by various disturbances and torsion.

In contrast, a cylindrical LIM above the reaction plate which is a cylindrical shell-shaped conductor has an advantage that the magnetic force acts on the reaction plate uniformly. This is expected to suppress the vibration in the gap direction. However, a conventional LIM is a system that drives the mover in the horizontal direction, and system design guidelines of a device that can directly exert power in the vertical direction have yet to be established. Therefore, in this paper, our research group proposed a cylindrical LIM that moves vertically above the uniform conductive cable as a reaction plate and investigated the possibility of the proposed LIM for vertical transportation. We constructed an analysis model of the cylindrical LIM and performed electromagnetic field analyses by the finite element method to discuss the vertical transportation performance of the LIM. In addition, assuming that this LIM is used as an actuator that vertical transfer on a super high-rise structure, it is required that the reaction plate be as thin as possible. Therefore, the thickness of the reaction plate was changed in the analyses, the effect on the generated thrust was investigated.

2. Vertical Transfer Actuator Using Cylindrical LIM

Figure 3 shows the proposed actuator using the cylindrical LIM installed above the cable-shaped conductor as a reaction plate. The proposed system used for a position sensor to measure radial and axial displacements. The measured displacements are input to a controller. The controller calculates a control output to maintain the radial gap and axial velocity. The obtained control output is input to a polyphase inverter, and a generated current for driving is input to the LIM. The sinusoidal currents having different phases are input to plural coils in the LIM, and a moving

Table 1 Specifications of the analysis model.

Material	Core	S45C
	Bobbin	Plasstic
	Coil	Cu
	Cable	Cu
LIM	Outer diameter	174 mm
	Inner diameter	100 mm
	Height	264 mm
Cable	Outer diameter	98 mm
	Thickness	1-20 mm
Number of coils		6
Air gap		1 mm

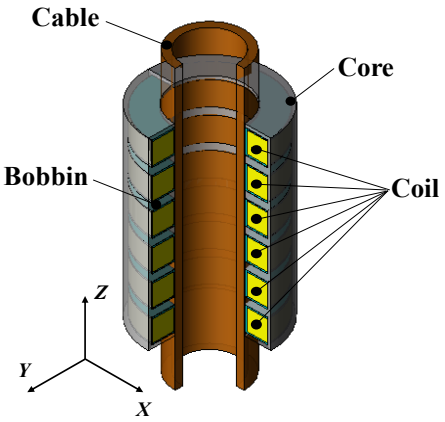

Fig. 4 Analysis model of proposed LIM.

magnetic field is generated. An eddy current is induced in the conductor cable by the generated moving magnetic field. The proposed system uses the Lorentz force generated by the generated eddy current and moving magnetic field to generate thrust.

3. Electromagnetic Field Analysis of the Proposed LIM

3.1 *Analysis condition*

To evaluate the thrust characteristics and lifting performance of the LIM for vertical movement, an analytical model of the LIM was created and an electromagnetic field analyses were performed. The analysis model is shown in Fig. 4. As shown in Figure 4, the axial direction of the cable was defined as the *Z* axis and the radial directions of the actuator were defined as the *X* and *Y* axes. Table 1 shows the specifications of the proposed analysis model. The LIM which consisted from a core, bobbin, and electrical coils had an outer diameter with 174 mm, an inner diameter with 100 mm, and height with 264 mm. The LIM was made of S45C for the core and plastic for the bobbin. The coils were installed at six locations in the core, and a phase difference was created in the coils using a three-phase AC power source.

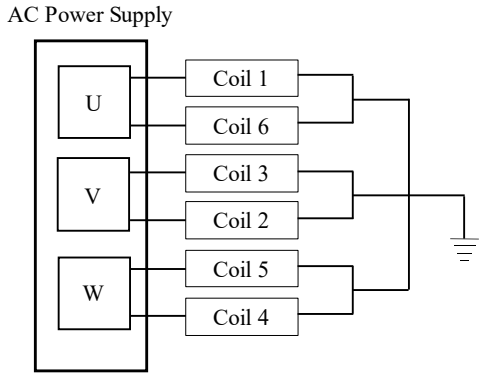

Fig. 5 Circuit diagram of the LIM analysis model.

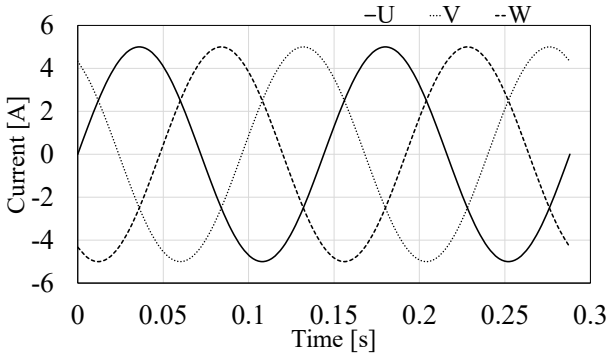

Fig. 6 Time history of input AC power from three-phase inverter.

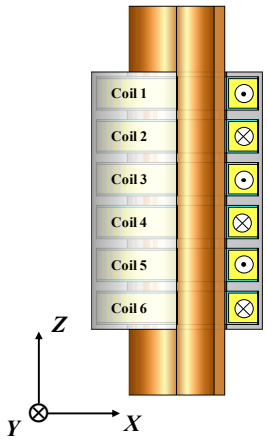

Fig. 7 Analysis model section view.

Figure 5 shows a circuit diagram of the analysis model used to generate a moving magnetic field. In the analysis conditions, the connection method was delta connection. The AC current which consists of U-V-W phase, as shown in Fig. 6, is applied to each coil. Figure 7 shows the arrangement and inflow direction of the coils. The coil can generate a phase difference of 60 degrees. In this study, the effect of changing the cable shape on the LIM thrust was investigated using electromagnetic field analysis. The materials used in the

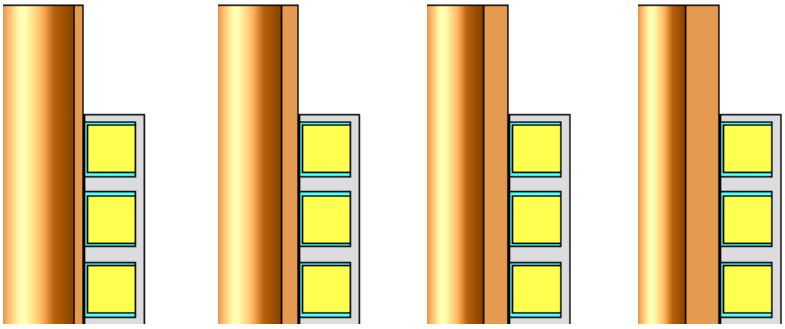

(a) h = 5 mm (b) h = 10 mm (c) h = 15 mm (d) h = 20 mm

Fig. 8 Analysis model in each cable thickness

cable with outer diameter 98 mm was copper. To examine the effect of the change in the cable thickness on the thrust, the thickness h of the cable was changed from 1 mm to 20 mm under the fixed outer diameter condition. Therefore, the gap between the inner surface of the LIM and the outer surface of the cable was constantly 1 mm in any analysis conditions.

3.2 *Finite element analysis model*

Figure 8 shows the analytical model when the cable thickness is 5, 10, 15, and 20 mm. The current amplitude was 5 A and the frequency of the AC current was 7 Hz. The analysis time was set to include two cycles of the AC current in 7 Hz. The mass of the analysis model was 17 kg. Therefore, the LIM was required a thrust of about 166.8 N or more to vertical transfer. Transient response analyses were performed under the above conditions. The analyzed electromagnetic forces in the Z axis direction were evaluated as the thrust characteristics.

4. Analysis Result of Thrust Generated by Proposed LIM

From the analysis results obtained by electromagnetic field analyses, Fig. 9 shows the time histories of analyzed thrust generated in the LIM at thicknesses h of the cable with (a) 5 mm, (b) 10 mm, (c) 15 mm, and (d) 20 mm. Analyzed thrusts of all analysis models increased rapidly in the initial term of the analyses. Then, thrusts converged fluctuating to each constant value of thrust. When the thickness of the cable increased, the thrust overshot largely and needed more time to saturate. It is considered that the inductance of the LIM increased owing to an increase in the thickness of the cable.

Figures 10, 11, and 12 show the analyzed magnetic flux densities, current densities, and Lorentz forces at thicknesses h of 5 mm, 10 mm, 15 mm, and 20 mm. In Fig. 10, although the magnetic flux density near the coils 3 and 6 acts strongly to the inner surface of the cable with thickness h within 10 mm, the flux density on the inner surface decrease when the thickness h was more than 15 mm. It is considered that the

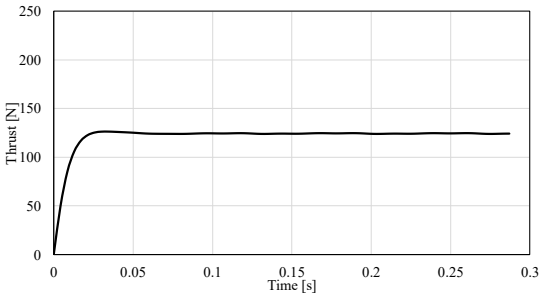

(a) h = 5 mm

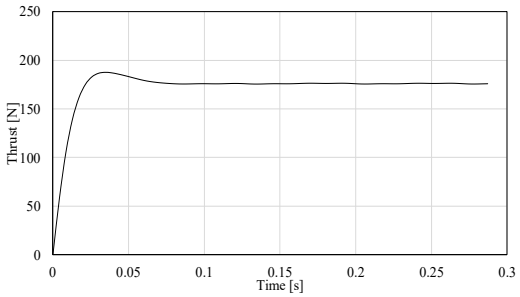

(b) h = 10 mm

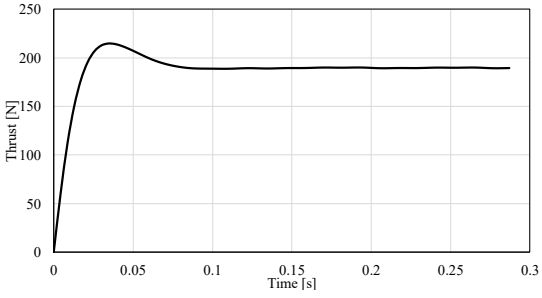

(c) h = 15 mm

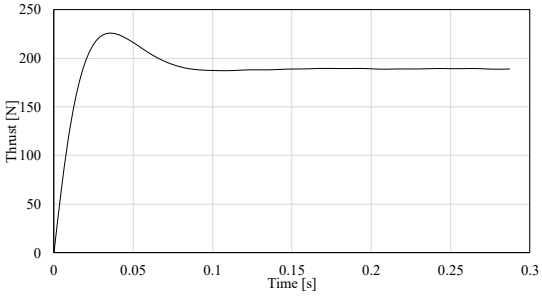

(d) h = 20 mm

Fig. 9 Time historys of thrust generated in the LIM.

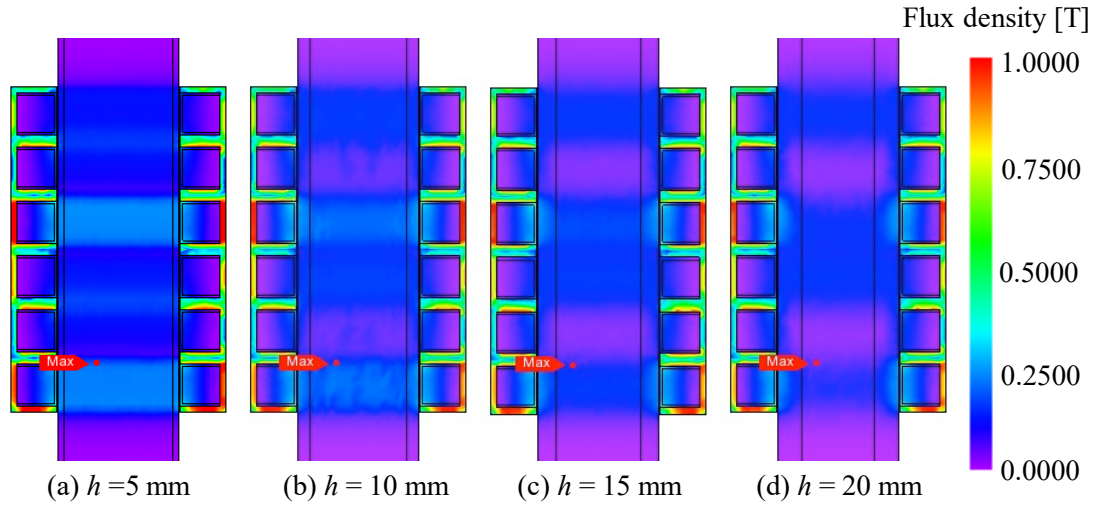

Fig. 10 Contour plot of magnetic flux density.

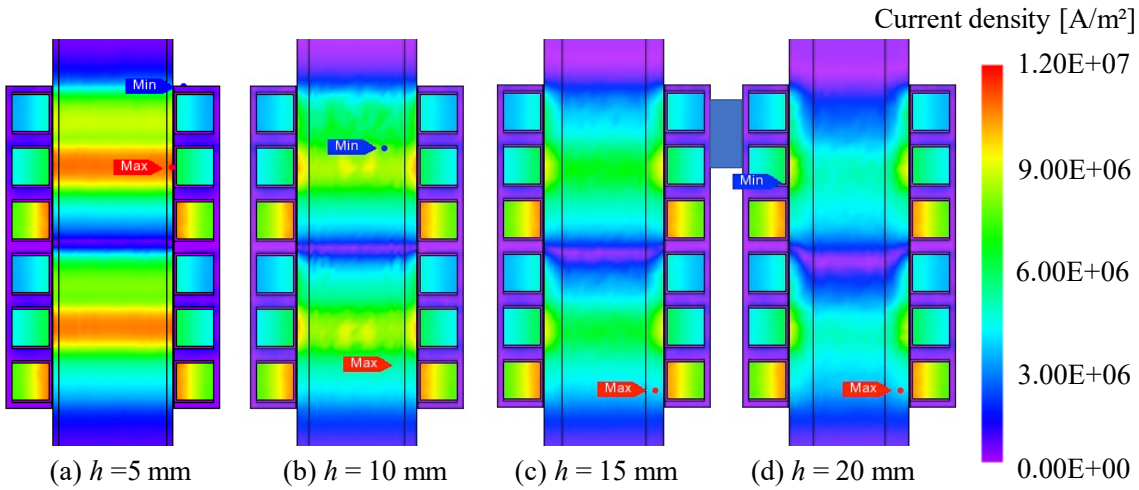

Fig. 11 Contour plot of current density.

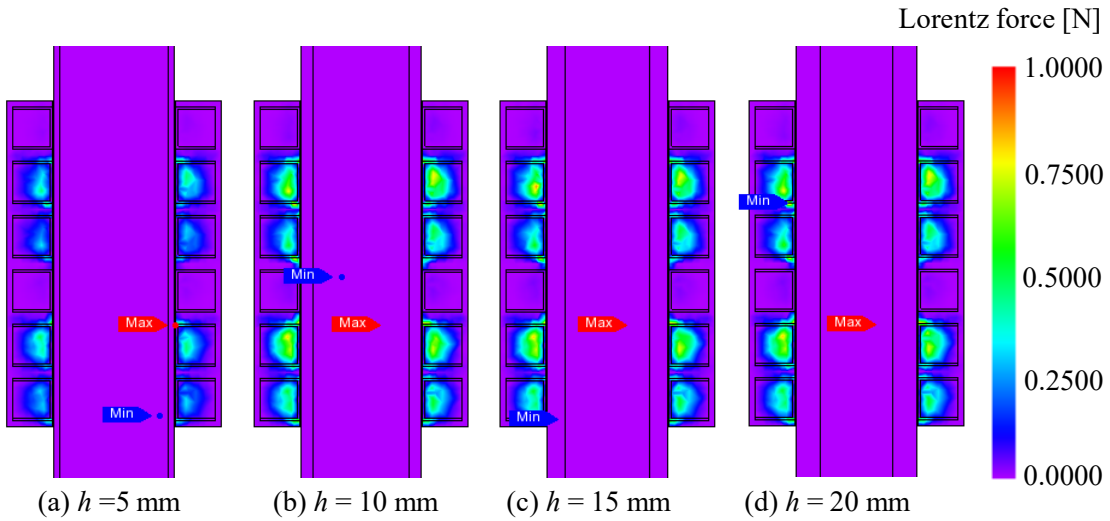

Fig. 12 Contour plot of Lorentz force.

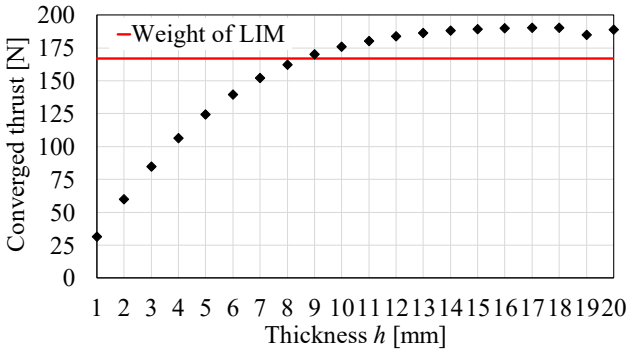

Fig. 13 Relationship between the thickness h and the converged thrust.

cable was too thick for the magnetic flux to through the cable. In Fig. 11, the current density occurred greatly at the coils 3 and 6, and in the cable near the coils 2 and 5. It is considered that the current in the cable was eddy-current which is inducted by the moving magnetic field. The current density acting on the cable was reduced by increasing the thickness of the cable. Therefore, Lorentz force as shown in Fig. 12 was greatly generated at the coils 2, 3, 5, and 6 since a Lorentz force was obtained by a cross-product of a magnetic flux and a current. It was confirmed that the current density acting on the cable was reduced by increasing the thickness of the cable, and the thrust increased by increasing the thickness of the cable. Figure 13 shows the relationship between the thickness h and the converged thrust. The converged thrust increased as the cable thickness increased, and saturated in the cases that the cable was thicker than 14 mm. The weight of the LIM is 166.8 N, hence the LIM can generate the thrust to lift itself in the case that the thickness h is thicker than 9 mm.

5. Conclusion

This paper proposed the vertical transportation system which moves above a long and uniform conductor cable without contact by using the cylindrical LIM as the actuator. We constructed an analysis model of the cylindrical LIM and performed electromagnetic field analyses by the finite element method to investigate the possibility of the cylindrical LIM as an actuator for vertical movement. From the analysis results, the thrust tended to increase by increasing the thickness of the cable. However, it was found that the thrust was not increased when the thickness exceeded a certain value since the magnetic flux density acting on the cable decreases with increases in cable thickness. Assuming that it is used as an actuator that vertical transfer on a super high-rise structure, it is required that the reaction plate be as thin as possible. From these conditions, the optimum thickness of the cable was able to be determined by obtaining the range of the magnetic flux density acting on the cable enough. In the future, we will perform the analysis by changing the material of the cable and adopting a material with high conductivity to improve the thrust characteristics. Furthermore, we will investigate the thrust during running, and a non-contact actuator using a LIM will be realized.

References

1) T. Matsuno: Recent Elevator Control, Journal of The Society of Instrument and Control Engineers, Vol.21, p.717 (1982).
2) T. Fujitani and H. Kimura: Vibration analysis of Elevator Rope with One Vibration Suppressor, Transactions of the JSME, Vol.89, 18-00048 (2018).
3) S. Jia: Optimal Configuration Analysis of Superconducting Cable Based on the Self-twist Discrete Element Model, Powder Thecnology, Vol.320, p.462 (2017).
4) Y. Ishikawa, K. Otsuka, Y. Yamagiwa and H. Doi: Effects of ascending and descending climbers on space elevator cable dynamics, Acta Astronautica, Vol.145, p.165 (2018).
5) K. Ishizaki, K. Soonsu, F. Inoue, E. Omoto and Y. Ishihkawa: Design and Analysis of Driving Roller for Climber in Space Elevator, The Proceedings JSME annual Conference on Robotics and Mevhatronics, 2A2-17b2 (2016).
6) Y. Aoki: Study on Climber of Space Elevator and Prototype Design of the Autonomous Probe Climber, Aeronautical and Space Sciences Japan, Vol.62, p.325 (2014).
7) R. Coa, E. Su and M. Lu: Comparative Study of Permanent Magnet Assisted Linear Swiche Reluctance Motor and Linear Flux Switching Permanent Magnet Motor for Railway Transportation: IEEE Transactions on Applied Superconductivity, Vol.30, p.3601205 (2020).
8) S. Watanabe, T. Koseki, Y. Noda and M. Miyatake: Optimized Energy-Saving Profile in Linear-Motor Railway System, IEEJ Transactions pn Industry Applications, Vol.137, p.44 (2017).
9) T. Mizuno: Present Status and Prospect on Linear Motor Drive Transport System, IEEJ Transactions pn Industry Applications, Vol.120, p.479 (2000).

Proc. Schl. Eng. Tokai Univ., Ser. E
45 (2020) 51-57
DOI: 10.18995/24343641.45.51

Ride Comfort Estimation Method Using Biological Information and Subjective Evaluation: A Fundamental Consideration Focusing on Jerk of Vertical Vibration

by

Takahiro OHTA[*1], Keigo IKEDA[*2] Ayato ENDO[*2]
Hideaki KATO[*3] and Takayoshi NARITA[*4]

(Received on May 11, 2020 and accepted on Jul. 24, 2020)

Abstract

In recent years, due to environmental problems and the aging society, the demand for ultra-compact vehicles has increased. One advantage of such vehicles is that they can be used on narrow or rough roads. However, such roads have many level differences and surface irregularities, which are likely to degrade the ride quality. We have proposed mounting a small active suspension device to the seat to improve ride comfort. To improve the ride comfort, a method for evaluating psychological state is needed. In this study, we researched a quantitative and objective method for evaluating ride comfort. First, the ride comfort of subjects was evaluated using a visual analog scale (VAS) of subjective evaluation and biological information in actual experiments. Jerk, which is the derivative of acceleration, is one of the indices that influences ride comfort. Therefore, experiments focusing on the jerk of vertical vibration were performed. Heart rate variability and cerebral blood flow were used as biological information in the experiments. Second, a function for estimating subjects' ride comfort was established from a model of the relationship between biological information and VAS value. Finally, we compared the predicted VAS value to the VAS value reported by the subjects. Thus, we researched the relationship between biological information and subjective evaluation of ride comfort.

***Keywords*:** Multiple regression analysis, Ride comfort, Subjective evaluation, Biological information, Active seat suspension

1. Introduction

In recent years, ultra-compact vehicle which is a car for one to two passengers has been proposed. The ultra-compact vehicle has an opportunity that runs on the narrow or unpaved road than a conventional vehicle. Even if the speed of the vehicle is relatively low, the ride quality of the vehicle would deteriorate due to a bad road. Therefore, Oshinoya et al. had proposed an "active seat suspension" to improve the ride comfort of the mobility[1]. We had conducted a study on vibration reduction using the active seat suspension and confirmed its effectiveness[2].

To improve the ride comfort of the vehicle, the vibration control system considering the psychological state of an occupant under vibration condition is required. Therefore, it is necessary to establish a method for estimating the feelings of an occupant. Conventionally, the sensory evaluation by a skilled person has been used to evaluate the ride comfort of vehicles[3]. In addition, the quantification of subjective evaluation based on physical quantities of vibration such as acceleration and frequency has been performed[4]. However, it is difficult to quantify the ride comfort of an occupant by the physical quantity of vibration because there are individual differences in sensation for each occupant. Therefore, the ride comfort evaluation using biological information that can objectively evaluate with considering the individual differences had been proposed as follows. Nakagawa et al. proposed a method of evaluating psychological state using electroencephalogram of train driver during driving[5].

*1 Undergraduate Student, Department of Prime Mover Engineering.
*2 Graduate Student, Course of Science and Technology.
*3 Junior Associate Professor, Department of Prime Mover Engineering.
*4 Assistant Professor, Department of Prime Mover Engineering.

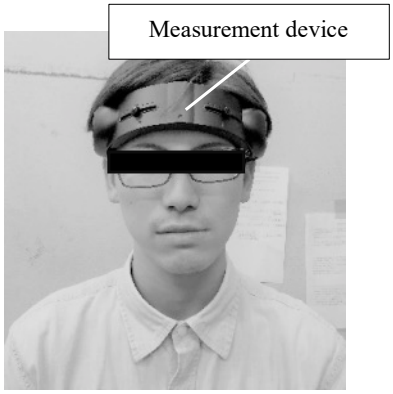

(a) Installation drawing

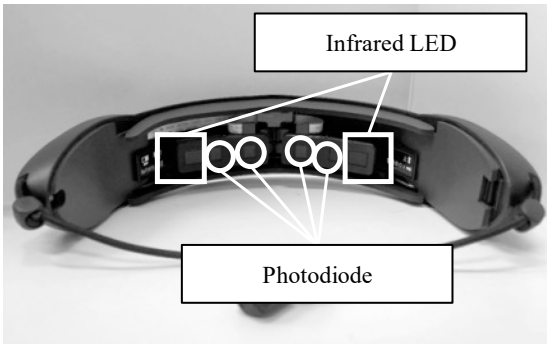

(b) Back side

Fig. 1 Measuring device for cerebral blood flow.

Shimizu et al. proposed a method to evaluate burden of driving operation using cerebral blood flow of driver[6]. In addition, we researched that change of heartbeat interval (hereafter heart rate variability) reflected autonomic nervous system activity was responded to the frequency of vibration[7]. Moreover, we researched that cerebral blood flow was affected by vibration[8),9)]. However, these studies do not clarify the relationship between the response of biological information and the ride comfort of the actual feelings of occupants. It is necessary to clarify the relationship between the ride comfort and biological information we become able to evaluate the ride comfort objectively. Furthermore, one of factor to deteriorate ride comfort is jerk which is rate of acceleration changes with respect to time. Wang et al. evaluated relationship between ride comfort and longitudinal jerk using subjective evaluation considering continuous[10]. However, the evaluation has problem with objectivity.

In this study, the relationship between ride comfort of jerk and biological information was researched. First, the experiments in which subjects were exposed to vibration were performed to investigate the changing of ride comfort by jerk that is a factor of discomfort. Biological information of vibrated subjects was measured during the experiments. In addition, subjects evaluated the feel of ride comfort of the experiments by a visual analog scale (VAS), and the results were digitized to VAS values which were able to quantitively evaluated the ride comfort. Moreover, the relationship between occupants' biological information and their VAS values was modeled by using multiple regression analysis, and the estimation function of the occupants' ride comfort was established from the model. Finally, we compared the predicted VAS value obtained from the subjects' biological information by the established function to VAS value which the subjects evaluated subjectively. Therefore, the possibility of objective evaluation for subjective ride comfort was researched using the model.

2. Measurement and Evaluation of Biological Information

In this study, cerebral blood flow and heart rate variability were selected for estimating the ride comfort of the driver because the relationship of these biological signals and the ride comfort were researched[7-9].

The cerebral blood flow, which reflects central nervous system activity, was reported to increase right cerebral activity when the occupant was stressed and to increases left cerebral activity when the occupant was relaxed[11]. Therefore, the amount of increased cerebral blood flow in the right was used as an evaluation index in this experiment. That index was obtained by comparison between cerebral blood flow for 30 seconds from the start of the experiment and for 30 seconds till the end of the experiment. Laterality index at rest (LIR)", which indicates the relationship of the whole brain, was evaluated as an evaluation index of central nervous activity[12]. LIR is defined by following eq. (1).

$$LIR = \frac{\Sigma[(R_t - R_{min}) - (L_t - L_{min})]}{\Sigma[(R_t - R_{min}) + (L_t - L_{min})]} \quad (1)$$

Where, the right cerebral activity in the measurement interval is R_t, the left cerebral activity is L_t, the minimum value of the right cerebral activity is R_{min}, and the minimum value of the left cerebral activity is L_{min}. Figure 1 shows a cerebral blood flow meter which is a device consisting of two near-infrared LEDs and four photodiodes was mounted on the front.

Then, the following shows a method of calculating the value for evaluation of psychological state using heart rate variability[13]. In the electrocardiogram, the peak that appears periodically that shows the contraction of the left ventricle is called the R wave. The interval from the R wave to the next R wave was called RRI, and it shows heart rate variability. The power spectrum density was calculated by frequency analysis using the time history of the RRI. The integrated

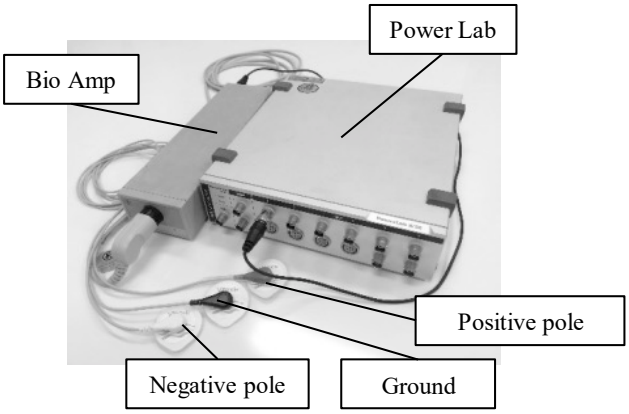

(a) Bio amp and power lab

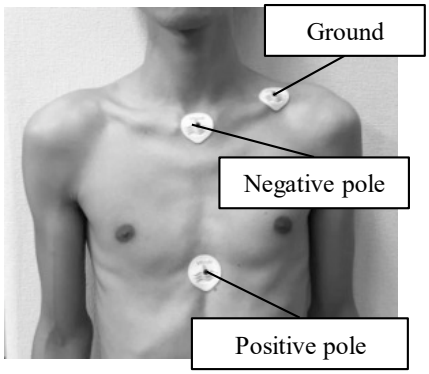

(b) Photograph of pasting position of electrode

Fig. 2 ECG measuring device.

value of the low frequency (LF: 0.04 to 0.15 Hz) component and the high frequency (HF: 0.15 to 0.4 Hz) component were calculated, and the ratio of these components was set to LF/HF. Subjects felt stress when the LF/HF is high and felt relaxation when LF/HF is low[13]. In this experiment, the electrodes were attached according to the NASA lead method of the electrocardiogram measuring device (Power Lab and Bio Amp, manufactured by AD Instruments) as shown in Fig. 2.

3. Quantitative Evaluation for Ride Comfort by Subjective Evaluation

In this study, the VAS which can evaluate ride comfort quantitatively was used as a subjective evaluation of the ride comfort[14]. Figure 3 shows an example of the VAS questionnaire. In VAS, a straight line of 10 cm was prepared for one question. The answer to the question was described at both ends of the straight line, the left end was indicated the most negative answer, and the right end was indicated the most positive answer. The subjects were instructed to freely draw a line intersection that indicating the current state as the answer to the question. After that, the distance from the left

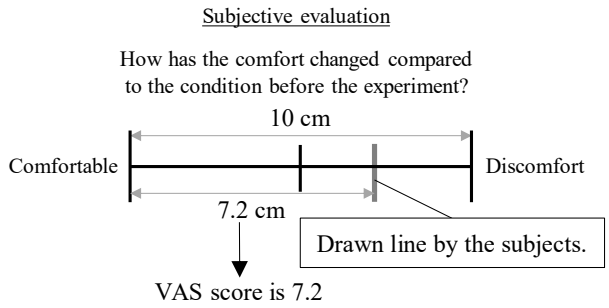

Fig. 3 Example of subjective evaluation.

end to the intersection line was measured and the value was considered as the score of the subjective evaluation. If the response is large, the reaction to the question is positive, and if it is small, then the reaction to the question is negative. In this experiment, the question was asked, "Show the current ride comfort compared to the state before the experiment.", and the answer was set at the left end indicating good ride comfort and at the right end indicating bad ride comfort. The subjects were told that, the center of the line indicated the state in which the test subjects themselves did not feel changes compared to the state before the experiment.

4. Design of Exposing Experiment

In this paper, subjective evaluation and biological signals were measured in experiments exposing the subjects to vibration. In this chapter, the apparatus and experimental design were explained.

The ultra-compact vehicle which was mounted the active seat suspension was used in the experiments as shown in Fig.4(a). The subjects were exposed to vibration by active seat suspension. During the experiment, as shown in Fig. 4 (b), subjects who wore measuring devises for cerebral blood flow and electrocardiogram set on the active seat suspension retaining the driving posture. Figure 4 (c) shows time chart. At first, the subjects were tasked for 1 minute of the arithmetic calculations. Next, the subjects were exposed to the vibration for 3 minutes. Finally, the subjects were tested VAS. At the first section, the subjects did the arithmetic calculations mentally that were displayed in monitor as shown in Fig.4(b). Were calculated by the mind of subjects. By this task, psychological state was matched every experiment.

In these experiments, it is necessary to research effect to ride comfort by change of jerk. Therefore, exposing condition of experiments is two jerk types. It is possible to change jerk by adjusting waveform or frequency of vibration. However, frequency is one of factor to effect ride comfort besides jerk[14]. It is necessary to maintain frequency at a constant.

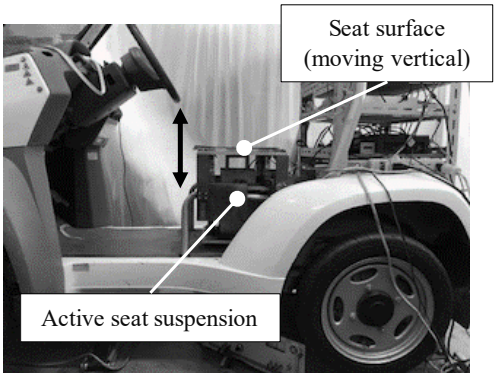

(a) Experimental system

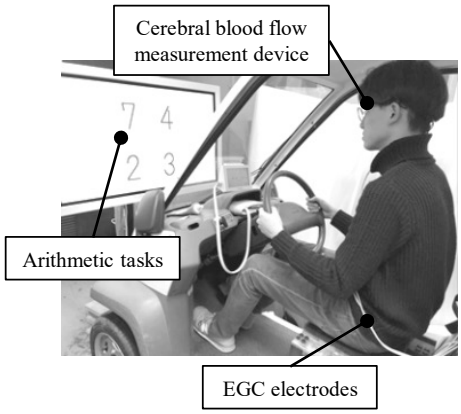

(b) State of subject

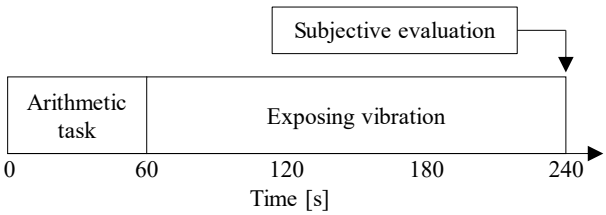

(c) Time chart

Fig. 4 Photograph of state of experiment and flow of experiment.

Hence, the acceleration waveform of exposing vibration was 5 Hz sine wave or square wave as shown in Fig. 5. Therefore, the sine wave (small magnitude jerk) and square wave (large magunitude jerk) were used in these experiments. Moreover, it is necessary that subjects feel exposing vibration fully. Matsumoto et al. reported that resonance point of sitting human is 5 Hz[15], subjects feel 5 Hz vibration sensitively. Therefore, frequency of vibration was 5 Hz in every experiment.

The experimental vehicle was jacked up to eliminate other vibration exclusive of exposing vibration by the active seat suspension. The experiment was conducted with 15 male students. The experiment was approved on the "Research targeting people (No. 19058)" by the Research Ethics Committee of Tokai University. Before experiments, subjects were informed about the study and experiments.

5. Multiple Regression Analysis

In this chapter, the relationship between the biological information and the VAS value was researched by a comprehensive analysis of multi biological information in experiments. The multivariable regression analysis is widely used to obtain the correlation of many variables in the statistics[16]. Therefore, in this study, the relationship between the biological information and subjective evaluation was researched using multiple regression analysis.

In this analysis, the biological information described in chapter 3 was used for the evaluation of the ride comfort. Moreover, normalized biological information values were used because the biological information was affected by the state of the subjects at starting experiments. It is ideal that the biological information before experiments was adjusted the same value. However, it was difficult that biological information was adjusted the same value because the biological information changes every moment. Therefore, the measured biological information was normalized by two standard values obtained from the state of the subjects before the exposing experiment. One of the standard values for normalization was obtained from the biological information measured when all subjects was sitting, relaxing, and closing eyes before the vibration experiment. The other was obtained from the biological information in the arithmetic task just before the exposing experiments. The ratios of the measured biological values to these standard values were calculated for normalized evaluation of the experimental results.

Equation (2) shows the multiple regression equation.

$$y = b_0 + b_1 x_1 + b_2 x_2 + b_3 x_3 + \cdots + b_i x_i \quad (2)$$

We defined the evaluation values, which were calculated from measured biological information of the subjects and used for multiple regression analysis in eq. (2), as follows; x_1: LIR, x_2: LF/HF, x_3: Right cerebral blood flow increases, x_4: LIR normalized on eyes closed state at resting time, x_5: LF/HF normalized on eyes closed state at resting time, x_6: LIR normalized on mental arithmetic time, x_7: LF/HF normalized on mental arithmetic time, x_8: LIR with eyes closed time, and x_9: LIR with eyes closed time. The multiple regression analysis performed to each experimental result of sinusoidal and square wave vibration and obtained coefficient b_i which shows the gradient with respect to the variation of each explanatory variable x_i. In this study, we aimed to

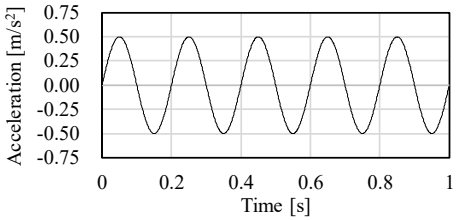

(a) Acceleration of sine wave

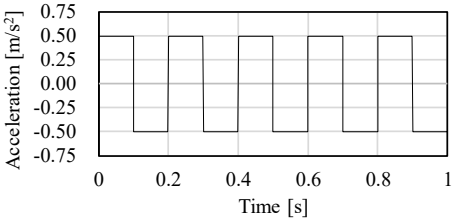

(b) Acceleration of square wave

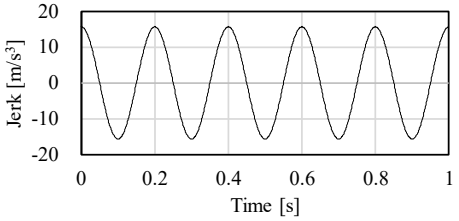

(c) Jerk of sine wave

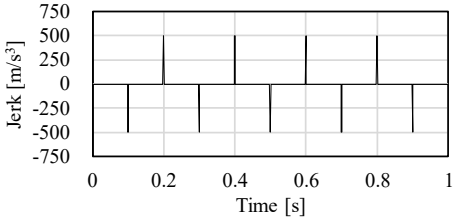

(d) Jerk of square wave

Fig. 5 Time histories of acceleration and jerk of seat surface.

estimate the VAS score by using the biological information. The objective variable y was set to VAS score for the ride comfort. If a coefficient b_i of the sinusoidal condition is large than b_i of the square wave, it means that the explanatory variable x_i corresponding to the b_i is more reflectable for the ride comfort. On the other hand, if a coefficient b_i is zero, it means that the explanatory variable x_i corresponding to the b_i does not react to the ride comfort.

From the results of multiple regression analysis, coefficients b_i in the case of sinusoidal and square vibration were obtained as shown in Table 1. Established prediction equation in sinusoidal and square vibration was expressed as eq. (3) and (4).

$$y = 2.75 - 0.261x_2 + 0.384x_3 + 4.13x_4 + 1.16x_5 + 2.10x_6 + 0.888x_7 + 0.588x_8 + 0.037x_9 \quad (3)$$

$$y = 8.14 - 0.316x_1 - 0.006x_2 + 3.73x_3 - 2.26x_4 + 0.160x_5 - 0.656x_7 + 1.98x_8 + 0.815x_9 \quad (4)$$

Coefficients of analysis results were shown that the effect for the ride comfort was different in each biological information. In the case of the square wave, coefficients of the cerebral blood flow affected the ride comfort because the absolute value of those coefficients was large. In the case of the sine wave, b_5 calculated using heart rate variability was large in addition to large coefficients in the square wave. Therefore, it was researched that estimating characteristics of the ride comfort were changed by the jerk of vibration.

Table 1 Explanatory variables and their values.

i	Variable x_i	coefficient b_i	
		Sine	Square
0	Constant	2.750	8.140
1	LIR	0.000	0.316
2	LF/HF	-0.262	-0.006
3	Right cerebral blood flow increases	0.384	-3.730
4	LIR normalized on eyes closed state at resting time	4.130	-2.260
5	LF/HF normalized on eyes closed state at resting time	1.160	0.160
6	LIR normalized on mental arithmetic time	2.100	0.000
7	LF/HF normalized on mental arithmetic time	0.888	-0.656
8	LIR with eyes closed time	0.588	1.980
9	LIR with eyes closed time	0.037	0.815

6. Objective Evaluation of Ride Comfort

In this chapter, we researched the possibility of estimating the ride comfort objectively using the results of the multiple regression analysis. From the measured biological information, the VAS score for the ride comfort was predicted eq. (3) and (4). Used biological information and VAS value in this chapter were the same as data analyzed in chapter 5. The method of evaluating the accuracy of estimating ride comfort is the comparison of “predicted VAS

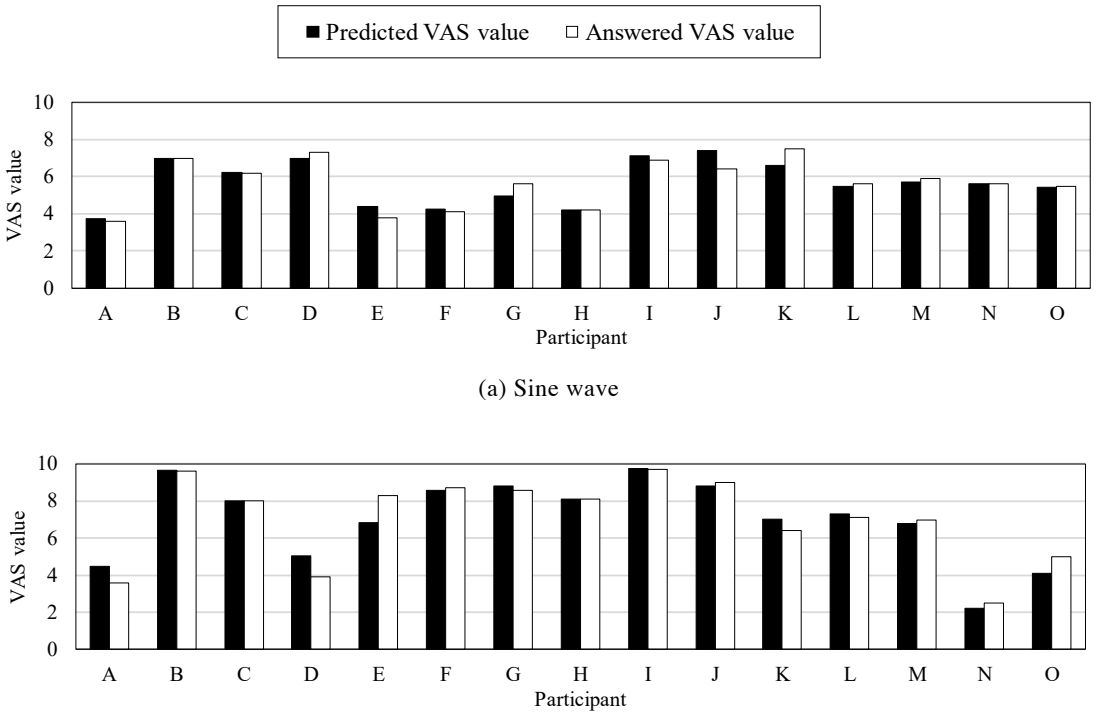

(a) Sine wave

(b) Square wave

Fig. 6 Relationship between prediction and actual answer.

values by estimating" and "answered VAS values in experiments". "Predicted VAS values by estimating" were the values calculated using the model of multiple regression analysis. Besides, "answered VAS values in experiments" were the values in which the subjects answered after exposing time.

Figure 6 shows the relationship between the predicted VAS value and the answered VAS value for each vibration condition. Figure 6 (a) shows the results of the sine wave, and (b) shows the results of the square wave. The correlation r between the predicted value and the measured value was 0.935 for the sine wave and 0.960 for the square wave, confirming a strong correlation. If the correlation r was closer to 1, it means that the established equation according to their biological information could estimate the feelings of the subjects correctly. Therefore, it is possible to estimate the ride comfort using the model that calculated multiple regression analyses in each jerk condition.

7. Conclusion

In this study, the ride comfort was evaluated quantitatively using the measured biological information and the answered VAS value in exposing vibration experiments. Moreover, we researched the relationship between the biological information and the objective evaluation of the VAS value by using the multiple regression analysis. In addition, it was confirmed that the subjective evaluation of the VAS value was able to be estimated by using the plural biological information, even though we researched in limited condition focused on the jerk in vertical vibration.

We will research objective and quantitative evaluation for the ride comfort in other vibration conditions, and establish an estimating method for the feeling of the driver to improve the ride comfort of vehicles.

References

1) Y. Oshinoya, H. Arai and K. Ishibashi, Experimental study on active seat suspension for a small vehicle, Int. J. App. Electromagn. Mech., Vol.19, p.437 (2004).
2) H. Kato, S. Hasegawa and Y. Oshinoya, Active Control of Ultra-Compact Vehicle Seat with Voice Coil Motor (Examination of the Control Performances during Driving on a Bad Road), J. Magn. Soc. Jpn., Vol.37, p.95 (2013).
3) K. Takei and M. Ishiguro: Evaluation of Ride Comfort on the Basis of Subjective Judgement, Tech. J. R&D review Toyota CRDL, Vol.30, p.47 (1995).
4) M. Okamura, T. Koizumi, N. Tsujiuchi and A. Kohama: A Study on the Evaluation of Ride Comfort Due to Human Dynamic Characteristics on Biaxail Vibration

(Vertical and Horizontal), Trans. Jpn. Soc. Mech. Eng. Ser. C, Vol.68, p.2865 (2002).

5) C. Nakagawa, N. Akiu, S. Yoshie, T. Nojima, T. Watanabe and A. Suzuki, Basic Study on Assessment of State of the Drivers Based on Physiological Indices, RTRI REPORT, Vol.33, No.1, p.5 (2019).
6) T. Shimizu and T. Nanbu, Measurement of Brain Activity in Driving Conditions using Functional Near-infrared Spectroscopy, Trans. Soc. Auto. Eng. Jpn., Vol.41, p.1263 (2010).
7) K. Ikeda, A. Endo, R. Minowa, T. Narita and H. Kato, Ride Comfort Control System Considering Physiological and Psychological Characteristics: Effect of Masking on Vertical Vibration on Passengers, actuators, Vol.7, p.42 (2018).
8) K. Ikeda, R. Minowa, A. Endo, H. Kato and T. Narita, Ride Comfort Control System Considering Physiological, Psychological, and Psychological Characteristics: Experimental Study of LIR, Proc. 2019 12th ASCC, p.1228 (2019).
9) A. Endo, K. Ikeda, R. Minowa, H. Kato and T. Narita, Evaluation of Ride Comfort and Vertical Vibration of Ultra-Compact mobility Vehicles Using Brain Blood Flow, Proc. Schl. Eng. Tokai Univ., Ser. E, Vol.43, p.17 (2018).
10) F. Wang, K. Sagawa, and H. Inooka, A study of the relationship between the longitudinal acceleration/deceleration of automobiles and ride comfort, Jpn. J. Ergonomics, **36** (2000) 191.
11) M. Tanida, M. Katsuyama, and K. Sakatani, Effects of fragrance administration on stress-induced prefrontal cortex activity and sebum secretion in the facial skin, Neurosci. Lett., Vol.432, p,157 (2008).
12) W. Ishikawa, M. Sato, Y. Fukuda, T. Matsumoto, N. Takemura and K. Sakatani, Correlation between asymmetry of spontaneous oscillation of hemodynamic changes in the prefrontal cortex and anxiety levels: A near-infrared spectroscopy study, J. Biomed. Opt, Vol.19, No.2, p.027005 (2014).
13) H. Kato, M. Ishida, M. Mashino and T. Narita, Proposal of ride comfort control system by psychological state estimation of the driver, Trans. JSME, Vol.81, No.832, p,15-00356 (2015).
14) V. SL. Williams, R. J. Morlock and D. Feltner, Psychometric evaluation of a visual analog scale for the assessment of anxiety, Hlth. Qlty. Life Outcomes, Vlol.8, p,57 (2010).
15) Y. Matsumoto and M. J. Griffin, A study of the dynamic response of the human body to vertical whole-body vibration, Doboku Gakkai Ronbunshuu, Vol.703, p.185 (2002).
16) K. Yokoyama and I. Takahashi, Feasibility study on estimating subjective fatigue from heart rate time series, IEICE Trans. Jpn., Vol. J96, p.756 (2013).

The School of Engineering of Tokai University publishes two kinds of Reports: the report written in English (once a year) and the one written in Japanese (twice a year). The report written in English includes original papers, as well as the abstracts of the papers which appeared in the reports written in Japanese.

*　　*　　*

Any requests for this proceedings should be addressed to the Editorial Committee of Procceedings of the School of Engineering Tokai University, 4-1-1, Kitakaname, Hiratsuka-shi, Kanagawa-ken. Japan

September 30, 2020

Attention:
The name of this PROCEEDINGS has been changed from 2002 edition as follows.
「PROCEEDINGS OF *THE SCHOOL OF ENGINEERINGS* /
THE SCHOOL OF INFORMATION SCIENCE
AND TECHNOLOGY OF TOKAI UNIVERSITY」